

Justus-Liebig-Universität Gießen
Fachbereich 07 - Mathematik und Informatik, Physik,
Geographie
Institut für Theoretische Physik I

Master's Thesis

Hyperon-Nucleon Interactions in Nuclear Matter

**Hyperon-Nukleon Wechselwirkungen
in Kernmaterie**

vorgelegt von

Anika Obermann

Betreuer: Prof. Dr. Horst Lenske

Gießen, September 2011

Contents

1. Introduction	1
2. Scattering Theory	3
2.1. Kinematics	3
2.2. Bethe-Salpeter Equation	4
2.2.1. Three-Dimensional Reduction	5
2.2.2. Blankenbecler-Sugar Propagator	5
2.2.3. Reduced BS Equation	7
2.3. Lippmann-Schwinger Equation	8
2.4. R -Matrix Equation	9
2.4.1. Uncoupled Channels	10
2.5. Decomposition in Partial Waves	10
2.5.1. Helicity Basis	11
2.5.2. LSJ Basis	12
2.6. Phase Shifts	14
2.7. Cross Sections	15
2.8. Low-Energy Parameters	15
3. Nucleon-Nucleon Interaction	16
3.1. Isospin	16
3.2. General Ansatz for the NN Potential	17
3.3. Bonn Potential	19
3.4. Non-Relativistic Momentum-Space Potential	20
3.5. Spin Dependence	21
3.6. Partial Wave Decomposition	22
3.6.1. Helicity Basis	22
3.6.2. LSJ-Basis	25
3.7. Singlet Potential	25
3.8. Cutoffs	26
3.8.1. Reformulation of the Vertex	27
3.8.2. Executing the Angular Integration	28
3.9. Singlet-Even- NN Potential	30
3.10. Results	31
3.10.1. Phase Shifts	31

3.10.2. Cross Sections	32
3.10.3. Low-Energy Parameters	32
3.10.4. Quality of Potential and Numerical Calculation	32
4. Hyperon-Nucleon Interaction	34
4.1. Hyperons	34
4.2. Ansatz	34
4.3. Masses	35
4.4. Conservation of s and Kinematics of Coupled Channels	36
4.5. Isospin Basis	36
4.5.1. $T = \frac{3}{2}$ Channel	37
4.5.2. $T = \frac{1}{2}$ Channels	38
4.5.3. Fitting Procedure	39
4.6. Results	40
4.6.1. Potential	40
4.6.2. Cross Sections	42
4.6.3. LE Parameters	43
4.7. Particle Basis	44
4.7.1. Uncoupled Channels	45
4.7.2. $Q = 1$ Channels	47
4.7.3. $Q = 0$ Channels	54
4.7.4. Quality of the Potential	58
5. In-Medium Interaction	59
5.1. Pauli Exclusion Principle in the R -matrix Equation	59
5.2. Pauli Projection Operator	60
5.2.1. Transformation to c.m. Frame	60
5.3. Results	64
5.3.1. Uncoupled Channels	64
5.3.2. $Q = 1$ Channels	66
5.3.3. $Q = 0$ Channels	70
5.3.4. Summary	73
6. Summary and Outlook	75
7. Bibliography	76
A. Solving the R-Matrix Equation	78
B. Approximation of the Legendre Functions	80
C. Properties of the Legendre Polynomials	81

D. Partial-Wave Decomposition	82
E. Danksagung	83
Versicherung an Eides statt (Affirmation)	84

1. Introduction

The interaction between nucleons, the nuclear force, is one of the main problems in nuclear physics. Yukawa made the first attempt to explain the nature of this force. His idea was that the interaction between two nucleons (NN interaction) is mediated via a third particle, called exchange boson [29]. This was the origin of a huge family of NN potential models, which are constructed out of potentials of the Yukawa type and called one-boson-exchange (OBE) models.

Nucleons are baryons and consist of three quarks, two up (u) and one down (d) quark form a proton while one u and two d quarks form a neutron. The interaction between the quarks is described by quantum chromodynamics (QCD), which is highly non-perturbative for the energy scale of nuclear physics. However, for this scale of low energies, QCD predicts the confinement of quarks into hadrons. OBE potentials are very successful in describing the experimental data, even though the coupling between nucleons (and all other hadrons) is not fundamental [18]. In recent years, chiral perturbation theory has been developed as an interesting QCD-inspired alternative approach, providing in principle a systematic ordering scheme for the various classes of diagrams contributing to baryon-baryon (BB) interactions [14].

Another type of baryons are the hyperons. They belong to the same flavor octet as the nucleons but have a different quark content: one of the u or d quarks is substituted by a strange (s) quark. An extension of the interaction model to hyperons is eligible, because strangeness-rich systems are important in understanding relativistic heavy-ion collisions, hypernuclei and astrophysical problems [28]. The scattering data for NN interaction are rich and accurate, as well as the NN potential models. Since there is less data for hyperon-nucleon (YN) scattering, the empirically best-known strong interaction is the NN interaction [18], but OBE models can be used for describing the YN interaction as well as the NN interaction [28]. Hence, a OBE model will be used for constructing a YN potential in this work. A clear advantage of OBE models, e.g. over the present day chiral approaches, is their very transparent operator structure dictated by basic requirements of Lorentz-invariance and the symmetries of strong interaction physics.

The second main research question of this work is the in-medium interaction of hyperons and nucleons, which is of interest e.g. for the study of hypernuclei. An simple way to include in-medium effects can be performed by assuming the interaction to occur

in infinite nuclear matter. The effect of infinite nuclear matter can be included in the scattering integral equation in terms of a Pauli projection operator [15].

This work is organized as follows: In the first chapter, the idea of two particle scattering will be introduced and a scattering integral equation, namely the R -matrix equation will be derived. Then, in the second chapter, a non relativistic NN potential for singlet scattering in momentum space will be derived from the Bonn potential. The derived potential and the R -matrix equation will be tested and compared to experimental data and theoretical predictions of other OBE models. In the third chapter, this potential is used as basis in order to obtain a YN potential. The YN potential will be constructed via fitting the modified NN potential on phase shift predictions of the Jülich group [16]. In the last chapter, the in-medium interaction is treated via including a two particle Pauli projection operator in the scattering equation. Finally, the results for in-medium YN interaction are given.

2. Scattering Theory

In this section, a short introduction to scattering processes will be given. First, the scattering in laboratory frame and the Mandelstam variable are introduced briefly.

In the main part, an integral equation for two-particle scattering is derived. Starting from a four-dimensional Bethe-Salpeter equation for the complex invariant scattering amplitude, we will achieve a one-dimensional Lippmann-Schwinger equation for a real scattering matrix in partial wave decomposition taking into account couplings between states of different particles and different quantum numbers. Emphasis is put on the structure of the propagator, while the other components of the scattering equations (i.e. potential and scattering matrix) will be discussed in detail in subsequent chapters. We follow the explanations in [18] and [15] closely, where a detailed derivation of integral equations for two particle-scattering can be found.

Finally, the main properties (e.g. cross sections and low energy parameters) for comparing theoretical calculations to the experiment as well to each other will be introduced.

2.1. Kinematics

Observing the scattering process in laboratory frame as shown in fig. 2.1, we find one particle moving with momentum \vec{p}_{Lab} (particle 1, called projectile), while the other particle is at rest (particle 2, called target). After the scattering, both particles are moving with momenta $\vec{p}'_{1,2}$ in an angle $\vartheta_{1,2}$ relative to the direction of \vec{p}_{Lab} .

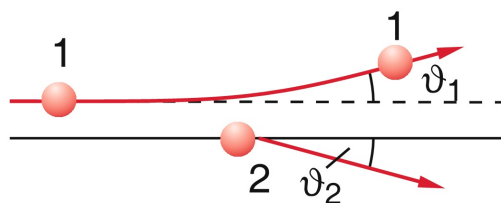


Figure 2.1.: Scattering of two particles in laboratory frame [10].

The four-momenta of particle 1 and 2 are:

$$p_1 = \begin{pmatrix} E_1(\vec{p}_{Lab}) \\ \vec{p}_{Lab} \end{pmatrix}, \quad p_2 = \begin{pmatrix} E_2(\vec{0}) \\ \vec{0} \end{pmatrix} \quad (2.1)$$

E_i denotes the relativistic energy of particle i :

$$E_i^2(\vec{p}) = \vec{p}^2 + M_i^2 \quad (2.2)$$

A conserved quantity of the scattering process is the squared total energy, i.e. the Mandelstam variable s . For scattering of particle 1 and 2 in the initial state into particle 3 and 4 in the final state it is defined as

$$s = (p_1 + p_2)^2 = (p_3 + p_4)^2. \quad (2.3)$$

The total energy then is defined as \sqrt{s} .

For convenience, especially in transformations between different reference frames, we define the laboratory frame properties in terms of s and find for the absolute value of the momentum of the projectile

$$p_{Lab} = \sqrt{\left(\frac{s - M_1^2 - M_2^2}{2M_2}\right)^2 - M_1^2} \quad (2.4)$$

and its kinetic energy

$$T_{Lab} = E_1(\vec{p}_{Lab}) - M_1 = \frac{s - (M_1 + M_2)^2}{2M_2}. \quad (2.5)$$

2.2. Bethe-Salpeter Equation

The Bethe-Salpeter (BS) equation is utilized to describe two particle scattering covariantly. It is a four-dimensional integral equation and can be written in operator notation as

$$\mathcal{T} = \mathcal{V} + \mathcal{V}\mathcal{G}\mathcal{T} \quad (2.6)$$

Here, \mathcal{T} is the invariant amplitude, \mathcal{G} is the relativistic propagator of the scattering process and \mathcal{V} is the sum of all connected two particle irreducible diagrams [18]. In an arbitrary frame the BS equation can be written as

$$\mathcal{T}(q', q|P) = \mathcal{V}(q', q|P) + \int \frac{d^4k}{(2\pi)^4} \mathcal{V}(q', q|P) \mathcal{G}(k|P) \mathcal{T}(k, q|P) \quad (2.7)$$

with initial, intermediate, and final relative four-momenta q , k and q' in center-of-mass (c.m.) frame, which is defined as the frame, where the sum over the momenta of all particles equals zero.

The total four-momentum P is directly related to the Mandelstam variable by

$$s = P^2. \quad (2.8)$$

The BS equation is a four-dimensional integral equation. As such it is difficult to solve.

2.2.1. Three-Dimensional Reduction

We want to solve the BS equation numerically, thus three-dimensional reductions are sufficient. They should be covariant and satisfy relativistic elastic unitarity as the original BS equation does. These reductions are not unique, but they usually are derived by decomposing 2.6 into the two coupled equations

$$\mathcal{T} = \mathcal{W} + \mathcal{W}g\mathcal{T} \quad (2.9)$$

$$\mathcal{W} = \mathcal{V} + \mathcal{V}(\mathcal{G} - g)\mathcal{W}. \quad (2.10)$$

Here, g is the covariant three-dimensional propagator with same elastic unitarity as \mathcal{G} in the physical region [18]. By dropping the second term in the right hand side of 2.10, we achieve a simplification of the problem and can write

$$\mathcal{T} = \mathcal{V} + \mathcal{V}g\mathcal{T}. \quad (2.11)$$

2.2.2. Blankenbecler-Sugar Propagator

The Blankenbecler-Sugar (BbS) propagator [4] is a possible choice for g :

$$g_{BbS}(k, s) = - \int_{(M_1+M_2)^2}^{\infty} \frac{ds'}{s' - s - i\epsilon} \cdot \delta(k_1^2 - M_1^2) \delta(k_2^2 - M_2^2) \Lambda^+(k_1, M_1) \Lambda^+(k_2, M_2) \quad (2.12)$$

Here, the integration variable s' is the total energy of the intermediate state and s is the total energy of the initial state. The δ -functions project the intermediate off-shell four-momenta k_i on the mass-shells M_i , and $\Lambda^+(k_i, M_i)$ is the positive-energy projection operator for particle i with mass M_i .

The intermediate off-shell four-momenta k_i are defined as

$$k_1 = x_1 P + k \quad (2.13)$$

$$k_2 = x_2 P - k. \quad (2.14)$$

with the invariant weights given in the c.m.-frame as

$$x_i = x_i(\vec{k}) = \frac{E_i(\vec{k})}{E_1(\vec{k}) + E_2(\vec{k})}. \quad (2.15)$$

The weights fulfill $x_1 + x_2 = 1$ and are composed of the relativistic energies (eq. 2.2).

Additionally, the weights are related to arbitrary $s' \neq s$ through

$$P^2 = (k_1 + k_2)^2 = s', \quad P = \begin{pmatrix} P_0 \\ \vec{0} \end{pmatrix}, \quad P_0 = \sqrt{s'}. \quad (2.16)$$

This choice gives for the k_i and the relative intermediate off-shell four-momentum k

$$k_1 = \begin{pmatrix} x_1 P_0 \\ \vec{k} \end{pmatrix}, \quad k_2 = \begin{pmatrix} x_2 P_0 \\ -\vec{k} \end{pmatrix} \quad (2.17)$$

$$k = x_2 k_1 - x_1 k_2 = \begin{pmatrix} P_0 (x_2 x_1 - x_1 x_2) \\ \vec{k} \end{pmatrix} = \begin{pmatrix} 0 \\ \vec{k} \end{pmatrix}. \quad (2.18)$$

Thus, k is a space-like four-vector and P is a time-like four-vector, which is consistent with our desired description in c.m. frame. Evaluation of the delta functions gives the requirements

$$k_1^2 = (x_1 P + k)^2 = x_1^2 s'_1 - \vec{k}^2 \stackrel{!}{=} M_1^2 \quad (2.19)$$

$$k_2^2 = (x_2 P + k)^2 = x_2^2 s'_2 - \vec{k}^2 \stackrel{!}{=} M_2^2. \quad (2.20)$$

Solving these equations for s' we find using eq. 2.15

$$s'_i = \frac{E_i^2(\vec{k})}{x_i^2(\vec{k})} = [E_1(\vec{k}) + E_2(\vec{k})]^2 = s'. \quad (2.21)$$

But at this point we stay at the notation of the s'_i rather than substituting all of them by s' . Using this result leads to the following form of the propagator:

$$\begin{aligned} g_{BbS}(k, s) = & - \frac{\delta(k_1^2(s'_2) - M_1^2)}{s'_2 - s - i\epsilon} \Lambda^+(k_1(s'_2), M_1) \Lambda^+(k_2(s'_2), M_2) \\ & - \frac{\delta(k_2^2(s'_1) - M_2^2)}{s'_1 - s - i\epsilon} \Lambda^+(k_1(s'_1), M_1) \Lambda^+(k_2(s'_1), M_2) \end{aligned} \quad (2.22)$$

In the next step we have to evaluate the remaining δ -functions. The evaluation is carried out using a relative four-momentum with non-zero time-like component: $k = (k_0, \vec{k})$. Consequently, we reformulate the k_i , again:

$$\begin{aligned} k_1^2(s'_2) &= (x_1 P + k)^2 = x_1^2 P_0^2 + 2x_1 k_0 P_0 + k_0^2 - \vec{k}^2 \\ &= k_0 [k_0 + 2E_1(\vec{k})] + M_1 \end{aligned} \quad (2.23)$$

$$\begin{aligned} k_2^2(s'_1) &= (x_2 P + k)^2 = x_2^2 P_0^2 - 2x_2 k_0 P_0 + k_0^2 - \vec{k}^2 \\ &= k_0 [k_0 - 2E_2(\vec{k})] + M_2 \end{aligned} \quad (2.24)$$

Where eqs. 2.15, 2.2 and 2.16 have been used. Now we can evaluate the δ -functions and we find (using the familiar properties of the δ -function):

$$\delta(k_1^2(s'_2) - M_1^2) = \delta(k_0 [k_0 + 2E_1(\vec{k})]) = \frac{1}{2E_1(\vec{k})} \delta(k_0) \quad (2.25)$$

$$\delta(k_2^2(s'_1) - M_2^2) = \delta(k_0 [k_0 - 2E_2(\vec{k})]) = \frac{1}{2E_2(\vec{k})} \delta(k_0) \quad (2.26)$$

Which is in agreement with our previous assumption of a space like k . Inserting this results and now substituting $s'_i = s'$ (eq. 2.21), we find the propagator

$$\begin{aligned} g_{BbS}(k, s) &= -\frac{\delta(k_0)}{2} \frac{1}{s' - s - i\epsilon} \left[\frac{1}{E_1(\vec{k})} + \frac{1}{E_2(\vec{k})} \right] \Lambda^+(k_1, M_1) \Lambda^+(k_2, M_2) \\ &= \frac{\delta(k_0)}{2\varepsilon_{12}(\vec{k})} \frac{1}{s - [E_1(\vec{k}) + E_2(\vec{k})]^2 - i\epsilon} \Lambda^+(k_1, M_1) \Lambda^+(k_2, M_2) \\ &= \delta(k_0) \overline{g_{BbS}}(\vec{k}, s) \end{aligned} \quad (2.27)$$

with the reduced energy

$$\varepsilon_{ij}(\vec{k}) = \frac{E_i(\vec{k}) E_j(\vec{k})}{E_i(\vec{k}) + E_j(\vec{k})} \xrightarrow{k \rightarrow 0} \frac{M_i M_j}{M_i + M_j} = \mu_{ij}. \quad (2.28)$$

2.2.3. Reduced BS Equation

We now can write the BS equation in the three dimensional reduction as

$$\mathcal{T}(\vec{q}', \vec{q} | \sqrt{s}) = \mathcal{V}(\vec{q}', \vec{q}) + \int \frac{d^3k}{(2\pi)^3} \mathcal{V}(\vec{q}', \vec{q}) \overline{g_{BbS}}(\vec{k}, s) \mathcal{T}(\vec{k}, \vec{q} | \sqrt{s}). \quad (2.29)$$

After taking the matrix elements between positive-energy spinors and executing the $\Lambda^+(k_i, M_i)$ we find

$$\hat{T}(\vec{q}', \vec{q}) = \hat{V}(\vec{q}', \vec{q}) + \int \frac{d^3k}{(2\pi)^3} \hat{V}(\vec{q}', \vec{q}) \frac{1}{2\varepsilon_{12}(\vec{k})} \frac{1}{s - (E_1(\vec{k}) + E_2(\vec{k}))^2 + i\epsilon} \hat{T}(\vec{k}, \vec{q}). \quad (2.30)$$

With the total energy $s = (E_1(\vec{q}) + E_2(\vec{q}))^2$ of the initial state. The spin, helicity, and isospin indices are suppressed at this point.

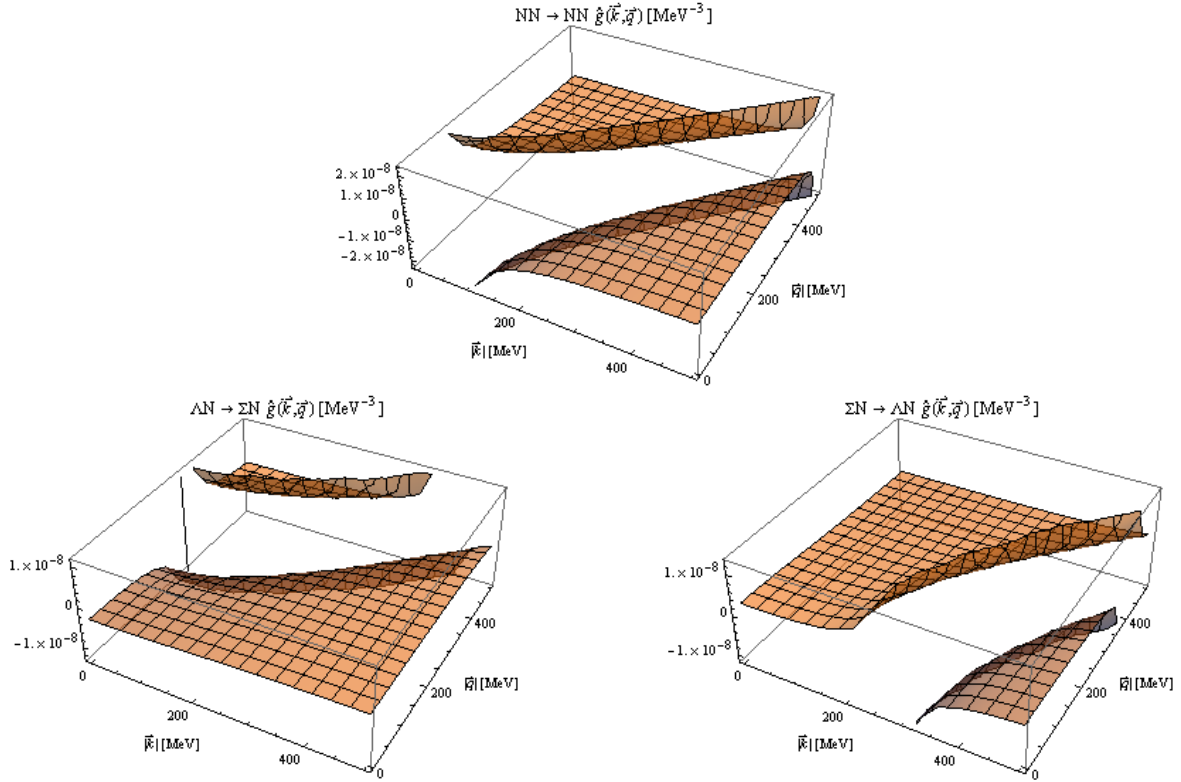


Figure 2.2.: $\hat{g}(\vec{k}, \vec{q})$ for $NN \rightarrow NN$, $\Lambda N \rightarrow \Sigma N$, and $\Sigma N \rightarrow \Lambda N$ scattering.

Thus, the propagator reads

$$\hat{g}(\vec{k}, \vec{q}) = \frac{1}{2\varepsilon_{12}(\vec{k})} \frac{1}{(E_1(\vec{q}) + E_2(\vec{q}))^2 - (E_1(\vec{k}) + E_2(\vec{k}))^2 + i\epsilon} \quad (2.31)$$

In fig. 2.2 the propagator $\hat{g}(\vec{k}, \vec{q})$ is plotted for $NN \rightarrow NN$, $\Lambda N \rightarrow \Sigma N$, and $\Sigma N \rightarrow \Lambda N$ scattering as function of the initial as well as the final momenta.

2.3. Lippmann-Schwinger Equation

The poles of the propagator $\hat{g}(\vec{k}, \vec{q})$ are on different positions, depending on the mass difference between initial and final channel. Only if the masses of initial and final channel are identical (e.g. for $NN \rightarrow NN$) the pole is placed on $|\vec{q}| = |\vec{k}|$ and thus can be treated easily in numerical calculations. Henceforth, we want to solve the scattering equation in shape of a Lippmann-Schwinger (LS) equation. That means we want to have the

propagator in a shape that satisfies a dispersion relation in the momentum rather than in s . In order to achieve this, we follow the description in [20] and define T and V as

$$\langle f | V | i \rangle = \frac{1}{\sqrt{4\mu_{34}(E_3(q') + E_4(q'))}} \langle f | \hat{V} | i \rangle \frac{1}{\sqrt{4\mu_{12}(E_1(q) + E_2(q))}} \quad (2.32)$$

$$\langle f | T | i \rangle = \frac{1}{\sqrt{4\mu_{34}(E_3(q') + E_4(q'))}} \langle f | \hat{T} | i \rangle \frac{1}{\sqrt{4\mu_{12}(E_1(q) + E_2(q))}}. \quad (2.33)$$

Here, i (f) denotes the initial (final) state with particles 1 and 2 (3 and 4) and relative momentum q (q'). The reduced mass is defined as

$$\mu_{ij} = \frac{M_i M_j}{M_i + M_j}. \quad (2.34)$$

Now choosing the propagator to be

$$g(\vec{k}_n, \vec{q}_n) = \frac{1}{2} \frac{1}{E_{n_1}(\vec{k}_n) + E_{n_2}(\vec{k}_n)} \frac{1}{\vec{q}_n^2 - \vec{k}_n^2 + i\epsilon} \quad (2.35)$$

we find the LS equation

$$\begin{aligned} \langle 3, 4, q' | T | 1, 2, q \rangle &= \langle 3, 4, q' | V | 1, 2, q \rangle + \sum_n \int \frac{d^3 \vec{k}}{(2\pi)^3} \langle 3, 4, q' | V | n_1, n_2, k_n \rangle \\ &\quad \cdot \frac{2\mu_{n_1 n_2}}{\vec{q}_n^2 - \vec{k}_n^2 + i\epsilon} \langle n_1, n_2, k_n | T | 1, 2, q \rangle. \end{aligned} \quad (2.36)$$

The poles of the propagator $g(\vec{k}_n, \vec{q}_n)$ have moved to $|\vec{q}_n| = |\vec{k}_n|$. Subsequently, the treatment of the poles is more easy.

2.4. *R-Matrix Equation*

We want to solve the LS equation numerically. Hence, it is desirable to use only real numbers, because it allows for calculating a lot faster [18]. In order to achieve a description through real numbers, we express the T -matrix in terms of the R -matrix:

$$T = \frac{R}{1 - iR} \quad (2.37)$$

The LS equation for the R -matrix for a given s is [18]:

$$R(\vec{q}', \vec{q}) = V(\vec{q}', \vec{q}) + \mathbf{P} \sum_n \int \frac{d^3 \vec{k}}{(2\pi)^3} V(\vec{q}', \vec{k}_n) G(\vec{k}_n, \vec{q}_n) R(\vec{k}_n, \vec{q}) \quad (2.38)$$

Here, q' , q , and k denote the relative four-momenta of the particles in the initial, intermediate, and final state, again. \mathbf{P} denotes the principal value. Its treatment is described in detail in appendix A. In operator notation this equation reads

$$R = V + VGR. \quad (2.39)$$

$G(\vec{k}_n, \vec{q}_n)$ is the Green's function. It has the shape

$$G(\vec{k}_n, \vec{q}_n) = \frac{2\mu_{n_1 n_2}}{\vec{q}_n^2 - \vec{k}_n^2} \quad (2.40)$$

Here, $\mu_{n_1 n_2}$ is the reduced mass of the intermediate system (eq. 2.34). q_n denotes the on-shell momentum and k_n the intermediate momentum in intermediate state n .

2.4.1. Uncoupled Channels

If initial, intermediate, and final state have the same particle content, i.e. $f = i = (n_1, n_2) = (1, 2)$, we find

$$T(\vec{q}', \vec{q}) = V(\vec{q}', \vec{q}) + \mathbf{P} \int \frac{d^3\vec{k}}{(2\pi)^3} V(\vec{q}', \vec{k}) G(\vec{k}, \vec{q}) T(\vec{k}, \vec{q}) \quad (2.41)$$

with the Green's function

$$G(\vec{k}, \vec{q}) = \frac{2\mu_{12}}{\vec{q}^2 - \vec{k}^2}. \quad (2.42)$$

2.5. Decomposition in Partial Waves

Strong interaction conserves total angular momentum J and parity $\pi = (-1)^L$. Therefore, transitions between different J^π are prohibited and these channels can be treated separately. For short range interactions only the lower partial waves are important. The decomposition of a potential is exemplified in appendix D.

The YN interaction is spin dependent, therefrom non central and spin-dependent forces occur. Furthermore, orbital angular momentum and spin are not conserved individually. However, the sum $\vec{J} = \vec{L} + \vec{S}$ is conserved.

In order to keep the notation simple, we perform the following derivations for an uncoupled channel, i.e. eq. 2.41. The calculations for coupled channels can be done in an analogous way.

The next step is aiming at solving the R -matrix equation for certain values of L , S and J . First we consider the spin of the particles. Since only baryons are involved, only a particle spin of $\frac{1}{2}$ occurs. We start with writing the LS-equation in helicity basis.

2.5.1. Helicity Basis

The helicity H of a particle is defined by the component of its spin \vec{S} in direction of its motion with momentum \vec{p} [10]:

$$H = \frac{\vec{S} \cdot \vec{p}}{|\vec{S}| \cdot |\vec{p}|} \quad (2.43)$$

This means a particle with spin parallel to the direction of its momentum has positive helicity (denoted by $+$) and is called “right-handed”. If the spin is antiparallel to the direction of motion, the helicity is negative ($-$) and the particle is called “left-handed”.

We now can write the R -matrix equation in partial wave decomposition with respect to all possible combination of helicities before, during and after the scattering process:

$$\begin{aligned} \langle \lambda'_1 \lambda'_2 | R^J(q', q) | \lambda_1 \lambda_2 \rangle &= \langle \lambda'_1 \lambda'_2 | V^J(q', q) | \lambda_1 \lambda_2 \rangle \\ &+ \sum_{h_1 h_2} \mathbf{P} \int \frac{dk}{2\pi^2} \langle \lambda'_1 \lambda'_2 | V^J(q', k) | h_1 h_2 \rangle G(k, q) \langle h'_1 h'_2 | R^J(k, q) | \lambda_1 \lambda_2 \rangle \end{aligned} \quad (2.44)$$

The angle integration has been executed, leading to a factor $4\pi k^2$. The integration now is one dimensional, and the remaining dependence on k has been moved into the Green's function:

$$G(k, q) = \frac{2\mu k^2}{q^2 - k^2} \quad (2.45)$$

Here R^J is the R -matrix with the total angular momentum J , h_1 and h_2 are the intermediate helicities of particle 1 and 2, λ_1 and λ_2 the initial and λ'_1 and λ'_2 the final helicities. Throughout the rest of the chapter only absolute three-momenta are needed. They are denoted by $|\vec{k}| = k$, $|\vec{q}| = q$, $|\vec{q}'| = q'$, for simplicity.

Ignoring antiparticles, $\langle \lambda'_1 \lambda'_2 | R^J(q', q|P) | \lambda_1 \lambda_2 \rangle$ includes $2^4 = 16$ different helicity amplitudes. Due to parity conservation, total spin conservation, and the time reversal invariance, they can be reduced to 6 independent amplitudes (which are partly decoupled):

$${}^0 R^J = \langle ++ | R^J | ++ \rangle - \langle ++ | R^J | -- \rangle \quad (2.46)$$

$${}^1 R^J = \langle +- | R^J | +- \rangle - \langle +- | R^J | -+ \rangle \quad (2.47)$$

$${}^{12} R^J = \langle ++ | R^J | ++ \rangle + \langle ++ | R^J | -- \rangle \quad (2.48)$$

$${}^{34} R^J = \langle +- | R^J | +- \rangle + \langle +- | R^J | -+ \rangle \quad (2.49)$$

$${}^5 R^J = \langle ++ | R^J | +- \rangle \quad (2.50)$$

$${}^6 R^J = \langle +- | R^J | ++ \rangle \quad (2.51)$$

For $\langle \lambda'_1 \lambda'_2 | V^J(q', q|P) | \lambda_1 \lambda_2 \rangle$ we introduce corresponding definitions. We could solve the R -matrix equation in helicity basis at this point, but usually this is done in another basis, the LSJ basis.

2.5.2. LSJ Basis

The representation of two baryon systems in terms of $|LSJM\rangle$ states is more common in nuclear physics than the representation in helicity space. Here, L denotes the relative orbital angular momentum, J the total angular momentum with projection M , and S the total spin. The channels are named $^{2S+1}L_J$. Hence the uncoupled state with the lowest numbers is called 1S_0 , this means $S = 0$, $J = 0$, and $L = 0$. The only other state with $J = 0$ is named 3P_0 in this convention; here the quantum numbers are $S = 1$, $J = 0$, and $L = J + 1 = 1$.

Transformation from helicity basis to LSJ basis yields coupling between channels of same total angular momentum J and parity π , written as J^π . However, the orbital angular momentum of the coupled channels is not identical, but has a difference of 2 ($L = J \pm 1$). The R -matrix elements are denoted by ${}^{L'L}R^J = \langle L'SJM | R^J | LSJM \rangle$, here $+$ refers to $L, L' = J + 1$, $-$ refers to $L, L' = J - 1$. The unitary transformation can be described by [18]:

$${}^0R^J = {}^0R^J \tag{2.52}$$

$${}^1R^J = {}^1R^J \tag{2.53}$$

$${}^{++}R^J = \frac{1}{2J+1} \left[(J+1) {}^{12}R^J + J {}^{34}R^J - 2\sqrt{J(J+1)} ({}^5R^J + {}^6R^J) \right] \tag{2.54}$$

$${}^{--}R^J = \frac{1}{2J+1} \left[J {}^{12}R^J + (J+1) {}^{34}R^J + 2\sqrt{J(J+1)} ({}^5R^J + {}^6R^J) \right] \tag{2.55}$$

$${}^{+-}R^J = -\frac{1}{2J+1} \left[\sqrt{J(J+1)} ({}^{12}R^J - {}^{34}R^J) + 2(J+1) {}^5R^J - 2J {}^6R^J \right] \tag{2.56}$$

$${}^{-+}R^J = -\frac{1}{2J+1} \left[\sqrt{J(J+1)} ({}^{12}R^J - {}^{34}R^J) - 2J {}^5R^J + 2(J+1) {}^6R^J \right] \tag{2.57}$$

Thus, the uncoupled channels ${}^0R^J$ and ${}^1R^J$ remain unchanged and the R -matrix equation in LSJ basis of these channels can be written in the familiar form as

$${}^0R^J(q', q) = {}^0V^J(q', q) + \mathbf{P} \int \frac{dk}{2\pi^2} {}^0V^J(q', k) G(k, q) {}^0R^J(k, q) \tag{2.58}$$

for the singlet and

$${}^1R^J(q', q) = {}^1V^J(q', q) + \mathbf{P} \int \frac{dk}{2\pi^2} {}^1V^J(q', k) G(k, q) {}^1R^J(k, q) \tag{2.59}$$

for the uncoupled triplet, while for the coupled triplet we find the coupled equations

$$\begin{aligned}
 {}^{++}R^J(q', q) = {}^{++}V^J(q', q) + \mathbf{P} \int \frac{dk}{2\pi^2} & \left[{}^{++}V^J(q', k)G(k, q){}^{++}R^J(k, q) \right. \\
 & \left. + {}^{+-}V^J(q', k)G(k, q){}^{-+}R^J(k, q) \right] \quad (2.60)
 \end{aligned}$$

$$\begin{aligned}
 {}^{--}R^J(q', q) = {}^{--}V^J(q', q) + \mathbf{P} \int \frac{dk}{2\pi^2} & \left[{}^{-+}V^J(q', k)G(k, q){}^{+-}R^J(k, q) \right. \\
 & \left. + {}^{--}V^J(q', k)G(k, q){}^{--}R^J(k, q) \right] \quad (2.61)
 \end{aligned}$$

$$\begin{aligned}
 {}^{-+}R^J(q', q) = {}^{-+}V^J(q', q) + \mathbf{P} \int \frac{dk}{2\pi^2} & \left[{}^{-+}V^J(q', k)G(k, q){}^{-+}R^J(k, q) \right. \\
 & \left. + {}^{--}V^J(q', k)G(k, q){}^{-+}R^J(k, q) \right] \quad (2.62)
 \end{aligned}$$

$$\begin{aligned}
 {}^{+-}R^J(q', q) = {}^{+-}V^J(q', q) + \mathbf{P} \int \frac{dk}{2\pi^2} & \left[{}^{++}V^J(q', k)G(k, q){}^{+-}R^J(k, q) \right. \\
 & \left. + {}^{+-}V^J(q', k)G(k, q){}^{+-}R^J(k, q) \right]. \quad (2.63)
 \end{aligned}$$

For coupled channels, the R -matrix equation can be written in operator notation as

$$\begin{pmatrix} {}^{++}R^J & {}^{+-}R^J \\ {}^{-+}R^J & {}^{--}R^J \end{pmatrix} = \begin{pmatrix} {}^{++}V^J & {}^{+-}V^J \\ {}^{-+}V^J & {}^{--}V^J \end{pmatrix} + \begin{pmatrix} {}^{++}V^J & {}^{+-}V^J \\ {}^{-+}V^J & {}^{--}V^J \end{pmatrix} \begin{pmatrix} G & 0 \\ 0 & G \end{pmatrix} \begin{pmatrix} {}^{++}R^J & {}^{+-}R^J \\ {}^{-+}R^J & {}^{--}R^J \end{pmatrix}. \quad (2.64)$$

Now we can write the LS equation for scattering in singlet and triplet partial waves including the coupling between different orbital angular momenta as well as coupling between different particle channels. All of these can be solved using the Fredholm method, which is described in appendix A.

2.6. Phase Shifts

Phase shifts describe the modification of the wave function through the scattering process. They can be expressed in terms of the on-shell R -matrix elements. For an uncoupled channel the relation is [18]:

$$\delta^J = \arctan\left(-q \frac{\mu}{2\pi} R^J\right) \quad (2.65)$$

Here q is the on-shell momentum and μ the reduced mass of the channel.

For coupled channels the Blatt-Biedenharn eigenphase shifts [5] can be related to the on-shell R -matrix elements through the relations [18]

$$\delta_+^J = \arctan\left(-q_+ \frac{\mu_+}{4\pi} \left(-R^J + R^J - \frac{-R^J - R^J}{\cos(\epsilon^J)}\right)\right) \quad (2.66)$$

$$\delta_-^J = \arctan\left(-q_- \frac{\mu_-}{4\pi} \left(-R^J + R^J + \frac{-R^J - R^J}{\cos(\epsilon^J)}\right)\right) \quad (2.67)$$

$$\epsilon^J = \frac{1}{2} \arctan\left(-2 \frac{R^J}{-R^J - R^J}\right). \quad (2.68)$$

Another convention for the phase shifts of coupled channels are the bar-phase shifts or Stapp phase shifts [26]. They are related to the Blatt-Biedenharn eigenphase shifts as

$$\bar{\epsilon} = \frac{1}{2} \arcsin[\sin(\delta_+ - \delta_-) \sin(2\epsilon)] \quad (2.69)$$

$$\bar{\delta}_1 = \frac{1}{2} \left[\delta_+ + \delta_- + \arcsin\left(\frac{\tan(2\bar{\epsilon})}{\tan(2\epsilon)}\right) \right] \quad (2.70)$$

$$\bar{\delta}_2 = \delta_+ + \delta_- - \bar{\delta}_1. \quad (2.71)$$

If the coupling ϵ is small, the bar and eigenphase shifts show only a small difference. For uncoupled channels, bar and eigenphase shifts become identical:

$$\bar{\epsilon} \xrightarrow{\epsilon \rightarrow 0} 0, \quad \bar{\delta}_1 \xrightarrow{\epsilon \rightarrow 0} \delta_+, \quad \bar{\delta}_2 \xrightarrow{\epsilon \rightarrow 0} \delta_- \quad (2.72)$$

The scattering matrix (or S -matrix) can be parameterized in terms of both phase shift conventions [21]:

$$S = \begin{pmatrix} \cos \epsilon & -\sin \epsilon \\ \sin \epsilon & \cos \epsilon \end{pmatrix} \begin{pmatrix} e^{2i\delta_+} & 0 \\ 0 & e^{2i\delta_-} \end{pmatrix} \begin{pmatrix} \cos \epsilon & \sin \epsilon \\ -\sin \epsilon & \cos \epsilon \end{pmatrix} \quad (2.73)$$

$$= \begin{pmatrix} e^{2i\bar{\delta}_1} \cos(2\bar{\epsilon}) & ie^{i(\bar{\delta}_1 + \bar{\delta}_2)} \sin(2\bar{\epsilon}) \\ ie^{i(\bar{\delta}_1 + \bar{\delta}_2)} \sin(2\bar{\epsilon}) & e^{2i\bar{\delta}_2} \cos(2\bar{\epsilon}) \end{pmatrix}. \quad (2.74)$$

For the uncoupled case we find

$$S = e^{2i\delta}. \quad (2.75)$$

2.7. Cross Sections

We will concentrate on scattering in the singlet-even (SE) channel (1S_0 in LSJ notation). The cross section for this channel can be calculated as [10]

$$\sigma_{ij} = \frac{4\pi}{q_i^2} |C_{ij}|^2. \quad (2.76)$$

The C_{ij} are the elements of the scattering amplitude T and related to the S -matrix through

$$C_{ij} = T_{ij} = \frac{1}{2i} (S_{ij} - \delta_{ij}). \quad (2.77)$$

For the uncoupled case we find

$$\sigma = \frac{4\pi}{q_i^2} \sin^2(\delta). \quad (2.78)$$

2.8. Low-Energy Parameters

An important and convenient measure of the interaction is obtained from the effective-range (ER) expansion. For $q \rightarrow 0$ the S -wave R -matrix elements behave as $\frac{\tan^0 \delta^0}{q}$, and can be expanded as

$$\frac{q}{\tan^0 \delta^0} = q \cot^0 \delta^0 \approx -\frac{1}{a_s} + \frac{1}{2} r_s q^2 \quad (2.79)$$

with the low-energy (LE) parameters a_s and r_s , the scattering length and the effective range. a_s is positive, if a bound state exists and negative, if that is not the case. The relation of the low energy parameters to the cross section is [25]

$$\lim_{q \rightarrow 0^+} \sigma = 4\pi a^2 + \mathcal{O}(k^2). \quad (2.80)$$

The cross section for low momenta thus is dominated by the scattering length.

The LE parameters are determined from the phase shifts by applying the method of least squares (described in more detail e.g. in [6]) in an interval of about $q = 0.1 - 1.0$ MeV with the polynomial

$$f(x) = \sum_n z_n x^n, \quad x = q^2, \quad n = 0, \dots, N. \quad (2.81)$$

N has to be chosen depending on the desired precision, but should be 1 or greater to include r_s .

3. Nucleon-Nucleon Interaction

This chapter focuses on nucleon-nucleon (NN) interaction. We will use the results of this chapter to describe hyperon-nucleon (YN) interaction in the next chapter.

In the first part of this chapter, an introduction to the characteristics of the NN interaction will be given and the model of interaction via exchange mesons will be introduced. Afterwards, a non relativistic NN potential for scattering in momentum space will be derived, using the Bonn potential [19] as the starting point. Emphasis will be put on the potential for scattering in singlet states. In the last part the derived NN potential for singlet-even (SE) scattering will be compared with experimental values and theoretical predictions from other models.

3.1. Isospin

Since nucleons have isospin $I = \frac{1}{2}$, the total isospin $|I_1 - I_2| \leq T \leq I_1 + I_2$ of a two nucleon system is either 0 or 1. The third isospin component is $I_z = \pm\frac{1}{2}$ for protons p and neutrons n , respectively. Thus, we find the total isospin three component of a two nucleon system $T_z = I_{z1} \pm I_{z2}$ to be $-1, 0, 1$ for nn, pn and pp systems. As T_z can have the values $-T, -T + 1, \dots, T - 1, T$ we find the nn and pp systems to consist of $T = 1$ alone, while the pn system can be composed of both total isospin values.

In case of treating the NN interaction in isospin space, both particles are identified as nucleons N rather than as proton and / or neutron and thus have to be treated as identical particles with $I_z = \frac{1}{2}$ and $s = \frac{1}{2}$. This leads to the requirement of a quantum number which guarantees the wave function of this system to be antisymmetric. Thus, the total isospin T is no longer an independent quantum number, but has to fulfill the following condition [18]

$$(-1)^{L+S+T} = -1. \tag{3.1}$$

That means, $L + S + T$ has to be an odd number.

We will solve the R -matrix equation for certain partial waves. However, we need to know which partial wave belongs to which isospin. By using eq. 3.1 we can determine the isospin for each partial wave. The results for low partial waves are shown in tab. 3.1.

T	partial waves
0	${}^3S_1, {}^1P_1, {}^3D_1, {}^3D_2, \dots$
1	${}^1S_0, {}^3P_0, {}^1D_2, {}^3P_2, \dots$

Table 3.1.: Isospin values T for NN -partial waves in LSJ notation.

The potential, R -matrix equation, and all other quantities mentioned before can be calculated either in isospin or in particle base. In isospin space n and p are not distinguished, but treated as identical nucleons. Therefore, there are only two cases; $T = 0, 1$. That makes the calculation in isospin base simple and comfortable. On the other hand, the calculation in particle base has the advantage, that physical particle masses are included. Furthermore, it is possible to include coulomb interaction because of distinction of channels after total charge. Additionally, one can compare the results with the experimental values and add the in-medium interaction.

We will use the isospin basis in this chapter because it allows for comparison of the results of our model with other theoretical models which are using the isospin basis.

3.2. General Ansatz for the NN Potential

In 1935, Hideki Yukawa found a potential which describes the NN interaction via exchange mesons [29]. He postulated the existence of an exchange meson, which later was identified as the pion. In fig. 3.1 the Feynman diagrams for NN interaction via virtual pions are shown.

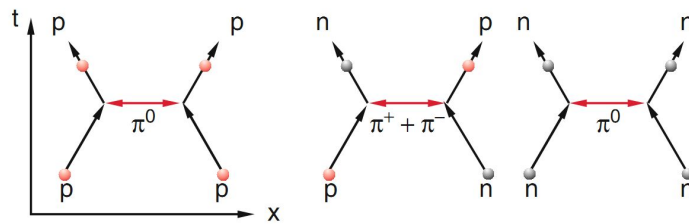
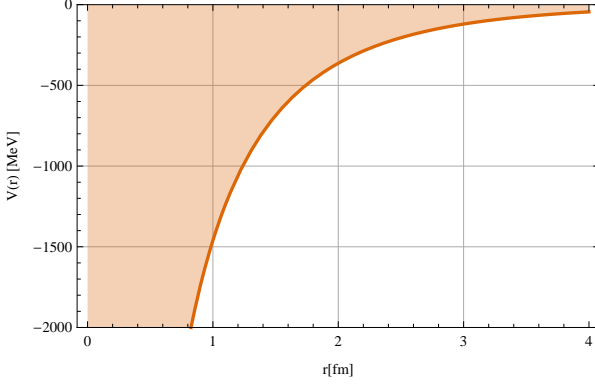


Figure 3.1.: Strong interaction via exchange of virtual pions [10].

In coordinate space the Yukawa potential has the shape

$$V(r) = V_0 \frac{e^{-r/R}}{r/R}; \quad R = \frac{\hbar c}{m}; \quad V_0 = -\frac{mg^2}{4\pi}. \quad (3.2)$$

The potential describes the interaction between two particles in a distance r mediated through the exchange of a meson with the mass m .



A Yukawa potential for exchange of a pion is shown in fig. 3.2. The coupling strength g determines the strength of the interaction, and thus the amplitude of the potential. R denotes the effective range of the potential. It decreases with increasing m . As a result, heavy mesons have a shorter range than light mesons.

Figure 3.2.: $V(r)$ for $m = m_\pi$, $g = g_\pi$ values taken from tab. 3.2.

The scattering equation is formulated in momentum space. We have to perform a Fourier transform to obtain the potential in momentum space. For a spheric symmetric potential this can be done via

$$f(\vec{k}) = \frac{1}{|\vec{k}| 2\pi^2} \int_0^\infty \sin(|\vec{k}| r) f(r) r dr. \quad (3.3)$$

For a detailed explanation of this procedure, see e.g. [22]. We find for the Yukawa potential in momentum space:

$$V(\vec{k}) = \frac{4\pi}{(2\pi)^3} V_0 R^3 \frac{m^2}{k^2 + m^2} = -\frac{g^2}{k^2 + m^2} \left(\frac{\hbar c}{2\pi}\right)^3 \quad (3.4)$$

Here, \vec{k} denotes the interchanged momentum.

Assuming the NN interaction is mediated through mesons, the NN potential can be determined by fitting the coupling constants of several Yukawa potentials with different coupling strengths g_i and masses m_i to experimental data.

In fig. 3.3 the shape of the SE- NN potential in coordinate space is shown. The potential can be divided in three parts with different properties: In the short range part (dark shaded area), the potential is highly repulsive. This part is called the hard core. In the intermediate range (light shaded area), the potential is attractive and approaches zero with increasing radius r in the long range part.

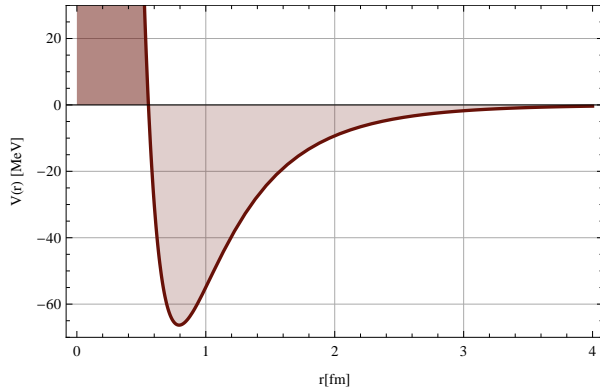


Figure 3.3.: Schematic plot of the SE- NN potential constructed of three exchange mesons (see text).

As can be seen easily, a single Yukawa potential does not fit the NN potential shown in fig. 3.3 on the full range, but the part where the potential becomes less attractive. Thus we will use a One-Boson-Exchange (OBE) potential. This type of potentials is made up of a sum of one-particle exchange amplitudes of several bosons, the interchanged mesons. The meson exchange picture for NN -interactions has been applied successfully by various groups, e.g. the Nijmegen models [27].

3.3. Bonn Potential

A well established and highly optimized OBE-model potential for NN -scattering is the Bonn potential [18, 19]. It assumes the exchange of six non strange mesons with masses below $1 \text{ GeV}/c^2$ to be relevant for the NN interaction. Consequently, the potential is constituted by summing up the potentials of the participating mesons:

$$V = \sum_{\beta} V_{\beta}, \quad \beta = \pi, \rho, \eta, \omega, \delta, \sigma \quad (3.5)$$

These mesons can be categorized within three groups with properties as shown in tab. 3.2:

Pseudoscalar Mesons $J^{\pi} = 0^{-}$ (i.e. zero spin $J = 0$ and negative parity $\pi = -$):

π The pion is the lightest meson included in the model and thus provides the long range part of the potential.

η The η -meson is the second lightest meson. It has a small coupling and provides a less important part of the potential.

Scalar Mesons $J^{\pi} = 0^{+}$:

σ is a fictitious meson, which is a parameterization of the 2π exchange and provides the attractive potential at intermediate range.

δ is the heaviest meson in the model. It has a weak coupling.

Vector Mesons $J^\pi = 1^-$:

ω is a 3π resonance and responsible for the strong repulsive force of short range.

ρ is a 2π resonance.

The π , δ and ρ mesons are isovector mesons ($I = 1$). They have three charge states (+, 0 and $-$) and their potentials gain an additional factor $\tau_1 \cdot \tau_2$, which leads to a factor -3 for $T = 0$ states [19].

Meson	J^π	I^G	m [MeV]	$\frac{g_{NN}^2}{4\pi}$	$\frac{f_{NN}}{g_{NN}}$	Λ [MeV]
η	0^-	0^+	548.8	3	—	1500
π	0^-	1^-	138.03	14.9	—	1300
σ	0^+	0^+	550 (715)	7.7823 (16.2061)	—	2000
δ	0^+	1^-	983	2.6713	—	2000
ω	1^-	0^-	782.6	20	0	1500
ρ	1^-	1^+	769	0.95	6.1	1300

Table 3.2.: Properties of the mesons and parameters of the Bonn potential [19]. Values in brackets apply to $T = 0$ states.

3.4. Non-Relativistic Momentum-Space Potential

Since the R -matrix equation is solved in momentum space, the potential has to be displayed in momentum space too. Following [19], we therefore introduce two new variables: the interchanged momentum \vec{k} and the average momentum \vec{p} . They are related to the incoming and outgoing relative momenta \vec{q} and \vec{q}' (which are defined in the same way as in the previous chapter) by

$$\vec{k} = \vec{q}' - \vec{q} \tag{3.6}$$

$$\vec{p} = \frac{1}{2} (\vec{q}' + \vec{q}) \tag{3.7}$$

For the squared quantities two relations follow directly (k , p , q , and q' marking absolute values of three-momenta in the further description):

$$k^2 = q'^2 + q^2 - 2q'q \cos \vartheta \tag{3.8}$$

$$p^2 = \frac{k^2}{4} + q'q \cos \vartheta \tag{3.9}$$

A non-relativistic reduction of the Bonn NN potential can be achieved by expanding the relativistic energies of the Bonn full model [19] in powers of k^2 and q^2 and keeping only the lowest order. From [19] we take the expressions for the interaction via pseudoscalar (ps), scalar (s), and vector (v) mesons:

$$V_{ps}(\vec{k}, \vec{p}) = -\frac{g_{ps}^2}{4M^2} \frac{(\sigma_1 \cdot \vec{k})(\sigma_2 \cdot \vec{k})}{k^2 + m_{ps}^2} \quad (3.10)$$

$$V_s(\vec{k}, \vec{p}) = -\frac{g_s^2}{2M^2} \frac{1}{k^2 + m_s^2} \left[2M^2 - p^2 + \frac{k^2}{4} - iS \cdot (\vec{k} \times \vec{p}) \right] \quad (3.11)$$

$$\begin{aligned} V_v(\vec{k}, \vec{p}) = & \frac{1}{k^2 + m_v^2} \\ & \left(\frac{g_v^2}{2M^2} \left[2M^2 + 3p^2 - \frac{k^2}{4} + 3iS \cdot (\vec{k} \times \vec{p}) - \sigma_1 \cdot \sigma_2 \frac{k^2}{2} + \frac{1}{2} (\sigma_1 \cdot \vec{k})(\sigma_2 \cdot \vec{k}) \right] \right. \\ & + \frac{g_v f_v}{2M^2} \left[-k^2 + 4iS \cdot (\vec{k} \times \vec{p}) - \sigma_1 \cdot \sigma_2 k^2 + (\sigma_1 \cdot \vec{k})(\sigma_2 \cdot \vec{k}) \right] \\ & \left. + \frac{f_v^2}{4M^2} \left[-\sigma_1 \cdot \sigma_2 k^2 + (\sigma_1 \cdot \vec{k})(\sigma_2 \cdot \vec{k}) \right] \right) \quad (3.12) \end{aligned}$$

Here, g_i and f_i are the coupling constants, M is the mass of the nucleon, and m_i is the mass of meson i .

3.5. Spin Dependence

The potentials in eqs. 3.10-3.12 include the spin dependence within four operators (shown in tab. 3.3) and can be written as a sum of these. According to [15], the potential reads

$$V(\vec{k}, \vec{p}) = \sum_{\alpha} \Omega_{\alpha} V_{\alpha}, \quad \alpha = c, \sigma, SL, \sigma k. \quad (3.13)$$

Here, σ_i is the spin operator for baryon i and $\vec{S} = \frac{1}{2}(\vec{\sigma}_1 + \vec{\sigma}_2)$ is the total spin operator.

central force	$\Omega_c = 1$
spin-spin force	$\Omega_{\sigma} = \vec{\sigma}_1 \cdot \vec{\sigma}_2$
spin-orbit force	$\Omega_{SL} = -i S \cdot (\vec{k} \times \vec{p})$
tensor force	$\Omega_{\sigma k} = (\vec{\sigma}_1 \cdot \vec{k})(\vec{\sigma}_2 \cdot \vec{k})$

Table 3.3.: Operators of the NN potential.

$\Omega_{\sigma k}$ can be decomposed into operators of good tensorial rank [19]

$$\Omega_{\sigma k} = k^2 \left(S_{12} + \frac{1}{3} \vec{\sigma}_1 \cdot \vec{\sigma}_2 \right) \quad (3.14)$$

with the rank-2 tensor $S_{12} = \frac{1}{3} \left(3 \frac{(\vec{\sigma}_1 \cdot \vec{k})(\vec{\sigma}_2 \cdot \vec{k})}{k^2} - \vec{\sigma}_1 \cdot \vec{\sigma}_2 \right)$ and the scalar (rank-0 tensor) $\sigma_1 \sigma_2$.

From comparison of eqs. 3.10-3.12 to eq. 3.13 and tab. 3.3 we find for the potential factors V_α :

$$\begin{aligned} V_{\sigma k}^{ps} &= -\frac{g_{ps}^2}{4M^2} \frac{1}{k^2 + m_{ps}^2}, \\ V_c^s &= -\frac{g_s^2}{8M^2} \frac{8M^2 - 4p^2 + k^2}{k^2 + m_s^2}, \quad V_{SL}^s = -\frac{g_s^2}{2M^2} \frac{1}{k^2 + m_s^2}, \\ V_c^v &= \frac{g_v^2}{M^2} \left(M^2 + \frac{3p^2}{2} - \frac{k^2}{8} - \frac{k^2 f_v}{2g_v} \right) \frac{1}{k^2 + m_v^2}, \quad V_\sigma^v = -\frac{(g_v + f_v)^2}{4M^2} k^2 \frac{1}{k^2 + m_v^2}, \\ V_{SL}^v &= -\frac{3g_v^2 + 4g_v f_v}{2M^2} \frac{1}{k^2 + m_v^2}, \quad V_{\sigma k}^v = \frac{(g_v + f_v)^2}{4M^2} \frac{1}{k^2 + m_v^2} \\ V_c^{ps} &= V_\sigma^{ps} = V_{SL}^{ps} = V_\sigma^s = V_{\sigma k}^s = 0 \end{aligned} \quad (3.15)$$

The V_α are dependent on k^2 and p^2 and thus on the absolute values of q' , q and $\cos \vartheta$, where ϑ is the angle between \vec{q}' and \vec{q} .

3.6. Partial Wave Decomposition

In order to achieve a description of the NN potential in LSJ basis, we have to follow the same procedure as we did for the R -matrix equation in section 2.5.

3.6.1. Helicity Basis

Following [15] and determining the helicities of baryon i before (λ_i) and after (λ'_i) the scattering, the six coupled potentials in helicity basis can be decoupled in a similar way as we found for the the R matrix (eqs. 2.46-2.51):

$${}^0V^J = \langle ++ | V^J | ++ \rangle - \langle ++ | V^J | -- \rangle \quad (3.16)$$

$${}^1V^J = \langle +- | V^J | +- \rangle - \langle +- | V^J | -+ \rangle \quad (3.17)$$

$${}^{12}V^J = \langle ++ | V^J | ++ \rangle + \langle ++ | V^J | -- \rangle \quad (3.18)$$

$${}^{34}V^J = \langle +- | V^J | +- \rangle + \langle +- | V^J | -+ \rangle \quad (3.19)$$

$${}^5V^J = \langle ++ | V^J | +- \rangle \quad (3.20)$$

$${}^6V^J = \langle +- | V^J | ++ \rangle \quad (3.21)$$

In helicity space the potential can be written as

$$\langle \lambda'_1 \lambda'_2 | V^J | \lambda_1 \lambda_2 \rangle = \sum_{\alpha} \langle \lambda'_1 \lambda'_2 | W_{\alpha}^J | \lambda_1 \lambda_2 \rangle, \quad \alpha = c, \sigma, SL, \sigma k \quad (3.22)$$

The helicities λ_i and λ'_i can be either positive or negative, which is denoted by $+$ and $-$. Thus there are sixteen helicity state amplitudes of $\langle \lambda'_1 \lambda'_2 | V^J | \lambda_1 \lambda_2 \rangle$. Because of time-reversal invariance, parity and spin conservation we need only six independent matrix elements [15]:

$$\langle ++ | W_{\alpha}^J | ++ \rangle = \frac{1}{2} \int_{-1}^1 d \cos \vartheta d_{00}^J(\vartheta) \langle ++ | \Omega_{\alpha} | ++ \rangle V_{\alpha} \quad (3.23)$$

$$\langle ++ | W_{\alpha}^J | -- \rangle = \frac{1}{2} \int_{-1}^1 d \cos \vartheta d_{00}^J(\vartheta) \langle ++ | \Omega_{\alpha} | -- \rangle V_{\alpha} \quad (3.24)$$

$$\langle +- | W_{\alpha}^J | +- \rangle = \frac{1}{2} \int_{-1}^1 d \cos \vartheta d_{11}^J(\vartheta) \langle +- | \Omega_{\alpha} | +- \rangle V_{\alpha} \quad (3.25)$$

$$\langle +- | W_{\alpha}^J | -+ \rangle = \frac{1}{2} \int_{-1}^1 d \cos \vartheta d_{-11}^J(\vartheta) \langle +- | \Omega_{\alpha} | -+ \rangle V_{\alpha} \quad (3.26)$$

$$\langle ++ | W_{\alpha}^J | +- \rangle = \frac{1}{2} \int_{-1}^1 d \cos \vartheta d_{10}^J(\vartheta) \langle ++ | \Omega_{\alpha} | +- \rangle V_{\alpha} \quad (3.27)$$

$$\langle +- | W_{\alpha}^J | ++ \rangle = \frac{1}{2} \int_{-1}^1 d \cos \vartheta d_{01}^J(\vartheta) \langle +- | \Omega_{\alpha} | ++ \rangle V_{\alpha} \quad (3.28)$$

The Jacobi functions $d_{ij}^J(\vartheta)$ can be expressed by the familiar Legendre polynomials $P_J(x)$. (For a short description of their properties see appendix C.)

$$d_{00}^J(\vartheta) = P_J(\cos \vartheta) \quad (3.29)$$

$$d_{11}^J(\vartheta) = \frac{P_J(\cos \vartheta) + \frac{J+1}{2J+1} P_{J-1}(\cos \vartheta) + \frac{J}{2J+1} P_{J+1}(\cos \vartheta)}{1 + \cos \vartheta} \quad (3.30)$$

$$d_{-11}^J(\vartheta) = \frac{-P_J(\cos \vartheta) + \frac{J+1}{2J+1} P_{J-1}(\cos \vartheta) + \frac{J}{2J+1} P_{J+1}(\cos \vartheta)}{1 - \cos \vartheta} \quad (3.31)$$

$$d_{10}^J(\vartheta) = \frac{\sqrt{J(J+1)}}{2J+1} \frac{P_{J+1}(\cos \vartheta) - P_{J-1}(\cos \vartheta)}{\sin \vartheta} \quad (3.32)$$

$$d_{01}^J(\vartheta) = -d_{10}^J(\vartheta) \quad (3.33)$$

In the next step we have to evaluate the mean values of Ω_α in helicity basis. Following [15] we can write the mean values of these operators in helicity basis:

$$\langle \lambda'_1 \lambda'_2 | \Omega_c | \lambda_1 \lambda_2 \rangle = \left(|\lambda'_1 + \lambda_1| \cos \frac{\vartheta}{2} + (\lambda'_1 - \lambda_1) \sin \frac{\vartheta}{2} \right) \left(|\lambda'_2 + \lambda_2| \cos \frac{\vartheta}{2} - (\lambda'_2 - \lambda_2) \sin \frac{\vartheta}{2} \right) \quad (3.34)$$

$$\begin{aligned} \langle \lambda'_1 \lambda'_2 | \Omega_\sigma | \lambda_1 \lambda_2 \rangle = & - \left((\lambda'_1 + \lambda_1) \sin \frac{\vartheta}{2} + |\lambda'_1 - \lambda_1| \cos \frac{\vartheta}{2} \right) \left((\lambda'_2 + \lambda_2) \sin \frac{\vartheta}{2} - |\lambda'_2 - \lambda_2| \cos \frac{\vartheta}{2} \right) \\ & - \left(|\lambda'_1 + \lambda_1| \sin \frac{\vartheta}{2} - (\lambda'_1 - \lambda_1) \cos \frac{\vartheta}{2} \right) \left(|\lambda'_2 + \lambda_2| \sin \frac{\vartheta}{2} + (\lambda'_2 - \lambda_2) \cos \frac{\vartheta}{2} \right) \\ & - \left((\lambda'_1 + \lambda_1) \cos \frac{\vartheta}{2} - |\lambda'_1 - \lambda_1| \sin \frac{\vartheta}{2} \right) \left((\lambda'_2 + \lambda_2) \sin \frac{\vartheta}{2} + |\lambda'_2 - \lambda_2| \sin \frac{\vartheta}{2} \right) \end{aligned} \quad (3.35)$$

$$\begin{aligned} \langle \lambda'_1 \lambda'_2 | \Omega_{SL} | \lambda_1 \lambda_2 \rangle = & - \frac{1}{2} q' q \sin \vartheta \\ & \left[\left(|\lambda'_1 + \lambda_1| \sin \frac{\vartheta}{2} - (\lambda'_1 - \lambda_1) \cos \frac{\vartheta}{2} \right) \left(|\lambda'_2 + \lambda_2| \cos \frac{\vartheta}{2} - (\lambda'_2 - \lambda_2) \sin \frac{\vartheta}{2} \right) \right. \\ & \left. + \left(|\lambda'_1 + \lambda_1| \cos \frac{\vartheta}{2} + (\lambda'_1 - \lambda_1) \sin \frac{\vartheta}{2} \right) \left(|\lambda'_2 + \lambda_2| \sin \frac{\vartheta}{2} + (\lambda'_2 - \lambda_2) \cos \frac{\vartheta}{2} \right) \right] \end{aligned} \quad (3.36)$$

$$\begin{aligned} \langle \lambda'_1 \lambda'_2 | \Omega_{\sigma k} | \lambda_1 \lambda_2 \rangle = & - 4 (\lambda'_1 q' - \lambda_1 q) (\lambda'_2 q' - \lambda_2 q) \\ & \left(|\lambda'_1 + \lambda_1| \cos \frac{\vartheta}{2} + (\lambda'_1 - \lambda_1) \sin \frac{\vartheta}{2} \right) \left(|\lambda'_2 + \lambda_2| \cos \frac{\vartheta}{2} + (\lambda'_2 - \lambda_2) \sin \frac{\vartheta}{2} \right) \end{aligned} \quad (3.37)$$

The mean values of $\langle \lambda'_1 \lambda'_2 | \Omega_\alpha | \lambda_1 \lambda_2 \rangle$ for the relevant helicity combinations in eqs. 3.23 - 3.28 are given in tab. 3.4.

	Ω_c	Ω_σ	Ω_{SL}	$\Omega_{\sigma k}$
$\langle ++ \Omega_\alpha ++ \rangle$	$\frac{\cos \vartheta + 1}{2}$	$\frac{-3 + \cos \vartheta}{2}$	$-\frac{q'q}{2} \sin^2 \vartheta$	$-\frac{(q'-q)^2}{2} (\cos \vartheta + 1)$
$\langle ++ \Omega_\alpha -- \rangle$	$\frac{\cos \vartheta - 1}{2}$	$\frac{3 + \cos \vartheta}{2}$	$-\frac{q'q}{2} \sin^2 \vartheta$	$-\frac{(q'+q)^2}{2} (\cos \vartheta - 1)$
$\langle +- \Omega_\alpha +- \rangle$	$\frac{\cos \vartheta + 1}{2}$	$\frac{1 + \cos \vartheta}{2}$	$-\frac{q'q}{2} \sin^2 \vartheta$	$\frac{(q'-q)^2}{2} (\cos \vartheta + 1)$
$\langle +- \Omega_\alpha -+ \rangle$	$\frac{\cos \vartheta - 1}{2}$	$\frac{1 - \cos \vartheta}{2}$	$\frac{q'q}{2} \sin^2 \vartheta$	$-\frac{(q'+q)^2}{2} (\cos \vartheta - 1)$
$\langle ++ \Omega_\alpha +- \rangle$	$-\frac{\sin \vartheta}{2}$	$-\frac{\sin \vartheta}{2}$	$-\frac{q'q}{2} \cos \vartheta \sin \vartheta$	$\frac{q'^2 - q^2}{2} \sin \vartheta$
$\langle +- \Omega_\alpha ++ \rangle$	$\frac{\sin \vartheta}{2}$	$\frac{\sin \vartheta}{2}$	$\frac{q'q}{2} \cos \vartheta \sin \vartheta$	$\frac{q'^2 - q^2}{2} \sin \vartheta$

Table 3.4.: Mean values of the spin dependence operators (eqs. 3.34-3.37) for relevant helicity combinations in eqs. 3.23 - 3.28.

3.6.2. LSJ-Basis

The transformation from helicity basis in LSJ-basis can be performed analogous to eqs. 2.58-2.63:

$${}^0V^J = {}^0V^J \quad (3.38)$$

$${}^1V^J = {}^1V^J \quad (3.39)$$

$${}^{++}V^J = \frac{1}{2J+1} \left((J+1) {}^{12}V^J + J {}^{34}V^J - 2\sqrt{J(J+1)} ({}^5V^J + {}^6V^J) \right) \quad (3.40)$$

$${}^{--}V^J = \frac{1}{2J+1} \left(J {}^{12}V^J + (J+1) {}^{34}V^J + 2\sqrt{J(J+1)} ({}^5V^J + {}^6V^J) \right) \quad (3.41)$$

$${}^{+-}V^J = -\frac{1}{2J+1} \left(\sqrt{J(J+1)} ({}^{12}V^J - {}^{34}V^J) + 2(J+1) {}^5V^J - 2J {}^6V^J \right) \quad (3.42)$$

$${}^{-+}V^J = -\frac{1}{2J+1} \left(\sqrt{J(J+1)} ({}^{12}V^J - {}^{34}V^J) - 2J {}^5V^J + 2(J+1) {}^6V^J \right) \quad (3.43)$$

The six potentials are diverted in singlet ($S = 0$) and triplet ($S = 1$) channels. The triplet channels can be divided in the uncoupled triplet channel ${}^1V^J$ and the coupled channels ${}^{\pm\pm}V^J$. In the further calculations we will concentrate on the singlet channel. the calculation for the triplet potential can be done analogously.

3.7. Singlet Potential

Using eqs. 3.22-3.24, 3.16 and tab. 3.4 we find for the singlet potential

$${}^0V^J = \frac{1}{2} \int_{-1}^1 d \cos \vartheta (V_c - 3V_\sigma - k^2 V_{\sigma k}) P_J(\cos \vartheta). \quad (3.44)$$

The spin-orbit force gives no contribution to the singlet potential; only central, spin-spin and the scalar component of tensor interactions remain in the formula. Inserting the relations for the potential factors (eq. 3.15) gives the singlet potential for each kind of mesons, respectively:

$${}^0V_{ps}^J(p, k) = \frac{1}{2} \int_{-1}^1 d \cos \vartheta \left(\frac{g_{ps}^2}{4M^2} \frac{k^2}{k^2 + m_{ps}^2} \right) P_J(\cos \vartheta) \quad (3.45)$$

$${}^0V_s^J(p, k) = \frac{1}{2} \int_{-1}^1 d \cos \vartheta \left(-\frac{g_s^2}{8M^2} \frac{k^2 - 4p^2 + 8M^2}{k^2 + m_s^2} \right) P_J(\cos \vartheta) \quad (3.46)$$

$${}^0V_v^J(p, k) = \frac{1}{2} \int_{-1}^1 d \cos \vartheta \left(\frac{g_v^2}{8M^2} \frac{\left[4 \left(\frac{f_v^2}{g_v^2} + \frac{f_v}{g_v} \right) + 3 \right] k^2 + 8M^2 + 12p^2}{k^2 + m_v^2} \right) P_J(\cos \vartheta) \quad (3.47)$$

The pseudoscalar mesons contribute only through the tensor force and the scalar mesons contribute only through the central force, while the vector mesons give a contribution to all three remaining forces.

We want to write the potential as function of q and q' only, therefore we insert the relations for k^2 and p^2 (eqs. 3.8 and 3.9) into eqs. 3.45-3.47, but keep the vertices as they are for simplicity. We find:

$${}^0V_{ps}^J(q', q, k) = \frac{1}{2} \frac{g_{ps}^2}{4M^2} \int_{-1}^1 d \cos \vartheta \frac{q'^2 + q^2 - 2q'q \cos \vartheta}{k^2 + m_{ps}^2} P_J(\cos \vartheta) \quad (3.48)$$

$${}^0V_s^J(q', q, k) = \frac{1}{2} \frac{g_s^2}{4M^2} \int_{-1}^1 d \cos \vartheta \frac{2q'q \cos \vartheta - 4M^2}{k^2 + m_s^2} P_J(\cos \vartheta) \quad (3.49)$$

$${}^0V_v^J(q', q, k) = \frac{1}{2} \frac{g_v^2}{4M^2} \int_{-1}^1 d \cos \vartheta \frac{\left[2 \left(\frac{f_v^2}{g_v^2} + \frac{f_v}{g_v} \right) + 3 \right] (q'^2 + q^2) + 4M^2 - 4 \left(\frac{f_v^2}{g_v^2} + \frac{f_v}{g_v} \right) q'q \cos \vartheta}{k^2 + m_v^2} P_J(\cos \vartheta) \quad (3.50)$$

We now have to carry out two different integrals for every kind of meson: One integral is proportional to $\frac{1}{k^2+m^2}$ and the other is proportional to $\frac{\cos \vartheta}{k^2+m^2}$. In the further calculation we write:

$${}^0V^J(q', q, k) = \frac{1}{2} \frac{g^2}{4M^2} \int_{-1}^1 d \cos \vartheta \left({}^0V_0 \frac{1}{k^2 + m^2} + {}^0V_1 \frac{\cos \vartheta}{k^2 + m^2} \right) P_J(\cos \vartheta) \quad (3.51)$$

with the factors

$${}^0V_0^{ps} = q'^2 + q^2, \quad {}^0V_1^{ps} = -2q'q, \quad {}^0V_0^s = -4M^2, \quad {}^0V_1^s = 2q'q, \\ {}^0V_0^v = \left[2 \left(\frac{f_v^2}{g_v^2} + \frac{f_v}{g_v} \right) + 3 \right] (q'^2 + q^2) + 4M^2, \quad {}^0V_1^v = -4q'q \left(\frac{f_v^2}{g_v^2} + \frac{f_v}{g_v} \right) \quad (3.52)$$

3.8. Cutoffs

The NN potential composed of Yukawa potentials becomes infinite for $r \rightarrow 0$. To prevent this, a so called cutoff is used. This suppresses the contribution of high momenta (corresponding to small distances) and is done by multiplying a form factor \mathcal{F}^2 at each meson-nucleon vertex:

$$\mathcal{F}^2(\vec{k}) = \left(\frac{\Lambda^2 - m^2}{\Lambda^2 + k^2} \right)^{2n} \quad (3.53)$$

The cutoff mass Λ determines the range of suppression and is adjusted to fit the empirical data. The exponent $n = 1, 2$ depends on the coupling, but is set to 1 for simplification

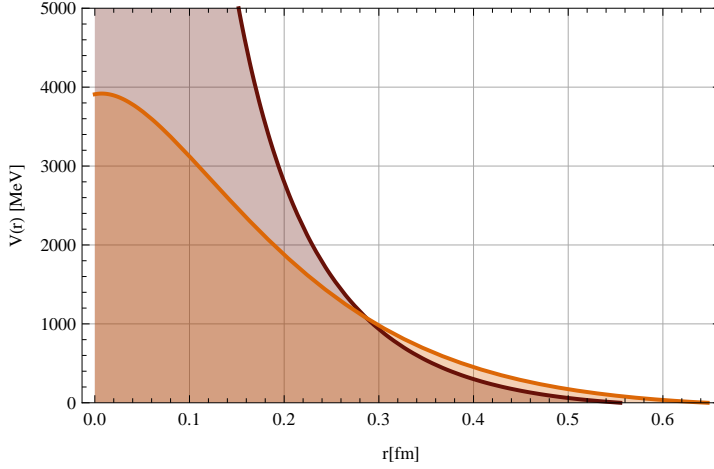


Figure 3.4: Repulsive part of an NN potential made up of Yukawa potentials (brown) and the potential modified with cutoffs (orange).

in the further calculations [19]. In fig. 3.4 the effect of applying the form factors to a coordinate space potential is shown schematically.

3.8.1. Reformulation of the Vertex

The cutoffs can be included in the potential by replacing the vertex with

$$\frac{1}{k^2 + m^2} \longrightarrow \frac{1}{k^2 + m^2} \left(\frac{\Lambda^2 - m^2}{\Lambda^2 + k^2} \right)^2 = \frac{1}{k^2 + m^2} - \frac{1}{k^2 + \Lambda^2} - \frac{\Lambda^2 - m^2}{(\Lambda^2 + k^2)^2} \quad (3.54)$$

We now have two terms which are of the familiar Yukawa type. One of them has the same meson mass as before and the other one has the cutoff mass instead. The rightmost term has a different structure. Using the relation for k^2 (eq. 3.8) it can be reformulated as a derivation

$$\frac{1}{(\Lambda^2 + k^2)^2} = - \left(\frac{1}{2q'q} \right)^2 \frac{\partial}{\partial Z_\Lambda} \frac{1}{Z_\Lambda - \cos \vartheta} \quad (3.55)$$

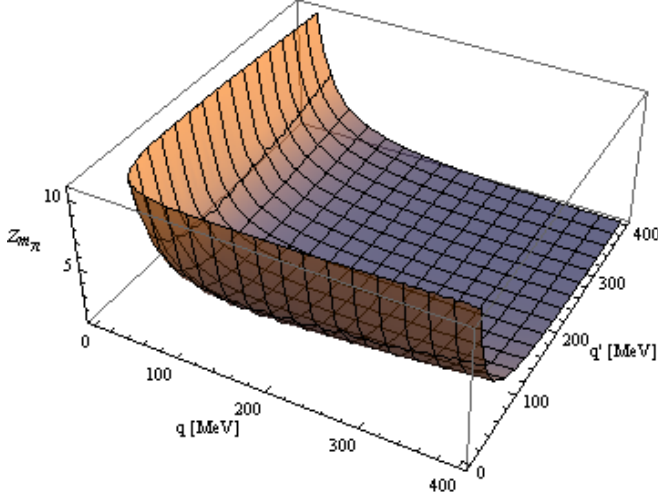
with the abbreviation

$$Z_M = \frac{q'^2 + q^2 + M^2}{2q'q} \quad (3.56)$$

Equation 3.56 is plotted in fig. 3.5 for interaction via pion exchange.

Reformulating the other terms of eq. 3.54 in a similar way, we find

$$\frac{1}{k^2 + m^2} \longrightarrow \frac{1}{2q'q} \frac{1}{Z_m - \cos \vartheta} - \frac{1}{2q'q} \frac{1}{Z_\Lambda - \cos \vartheta} + \left(\frac{1}{2q'q} \right)^2 \frac{\partial}{\partial Z_\Lambda} \frac{\Lambda^2 - m^2}{Z_\Lambda - \cos \vartheta}. \quad (3.57)$$


 Figure 3.5.: Z_{m_π}

Z_M has its minimal value for a given q at the onshell point

$$Z_M \xrightarrow{q' \rightarrow q} 1 + \frac{M^2}{2q^2}$$

and the absolute minimum is found to be

$$Z_M \xrightarrow{q' = q \rightarrow \infty} 1.$$

It follows that the integration $\int_{-1}^1 d \cos \vartheta$ will not cause any problems.

3.8.2. Executing the Angular Integration

We now insert the correction for the cutoff masses (eq. 3.57) in the integral and rewrite the formula substituting $f(\vartheta) = 1, \cos \vartheta$:

$$\begin{aligned} & \int_{-1}^1 d \cos \vartheta \frac{f(\vartheta)}{k^2 + m^2} P_J(\cos \vartheta) \\ \rightarrow & \frac{1}{2q'q} \int_{-1}^1 d \cos \vartheta \frac{f(\vartheta) P_J(\cos \vartheta)}{Z_m - \cos \vartheta} - \frac{1}{2q'q} \int_{-1}^1 d \cos \vartheta \frac{f(\vartheta) P_J(\cos \vartheta)}{Z_\Lambda - \cos \vartheta} \\ & + \left(\frac{1}{2q'q} \right)^2 (\Lambda^2 - m^2) \frac{\partial}{\partial Z_\Lambda} \int_{-1}^1 d \cos \vartheta \frac{f(\vartheta) P_J(\cos \vartheta)}{Z_\Lambda - \cos \vartheta} \end{aligned} \quad (3.58)$$

Integration and derivation can be executed in arbitrary order, because Z_Λ is not dependent on ϑ . We have to carry out the integration over two different types of integrands and find:

$$\int_{-1}^1 d \cos \vartheta \frac{P_J(\cos \vartheta)}{Z_M - \cos \vartheta} = 2Q_J(Z_M) \quad (3.59)$$

$$\int_{-1}^1 d \cos \vartheta \frac{\cos \vartheta P_J(\cos \vartheta)}{Z_M - \cos \vartheta} = 2Z_M Q_J(Z_M) - 2\delta_{J0} \quad (3.60)$$

With the Legendre functions of the second kind $Q_J(x)$. Following [2] they are defined recursively by

$$Q_J(x) = \frac{2J-1}{J} x Q_{J-1}(x) - \frac{J-1}{J} Q_{J-2}(x) \quad (3.61)$$

with the first two Legendre functions

$$Q_0(x) = \frac{1}{2} \ln \frac{x+1}{x-1} \quad (3.62)$$

$$Q_1(x) = x Q_0(x) - 1. \quad (3.63)$$

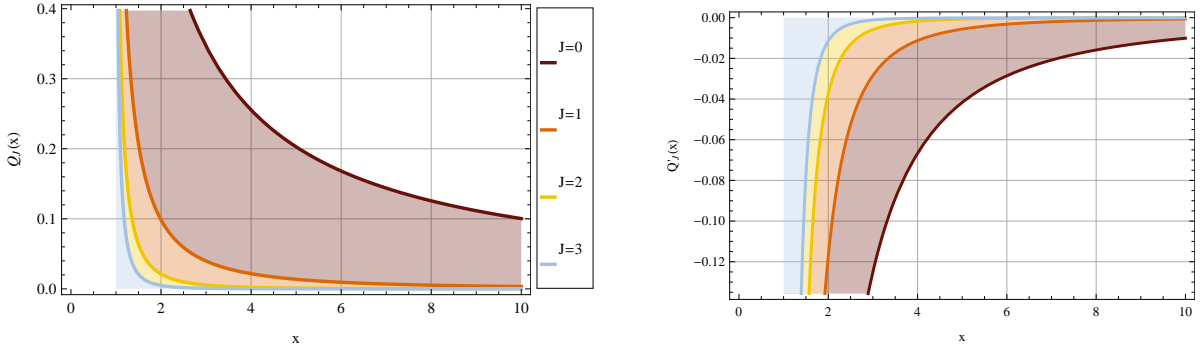


Figure 3.6.: Legendre functions $Q_J(x)$ and their derivatives $Q'_J(x)$ for total angular momenta $0 \leq J \leq 3$.

We need the derivation of the integrals also, and therefrom the derivatives $Q'_J(x)$. They are defined by

$$Q'_J(x) = \frac{J}{x^2 - 1} [x Q_J(x) - Q_{J-1}(x)] \quad (3.64)$$

$$Q'_0(x) = \frac{1}{2} \left(\frac{1}{x+1} - \frac{1}{x-1} \right) \quad (3.65)$$

$$Q'_1(x) = Q_0(x) + x Q'_0(x). \quad (3.66)$$

The Legendre functions of the second kind and their derivatives are plotted in fig. 3.6. For $x \rightarrow 1^+$ they are approaching $\pm\infty$, while for $x \rightarrow \infty$ they are approaching 0. The treatment of these functions in the numerical calculations is described in appendix B.

Using our results for the integrals together with eq. 3.58 in eq. 3.51 we find for the singlet partial wave ($L = J$)

$${}^0V^J(q', q) = \frac{g^2}{4M^2} ({}^0V_0 R_J(q', q) + {}^0V_1 T_J(q', q)) \quad (3.67)$$

with

$$R_J(q', q) = \frac{1}{2q'q} \left(Q_J(Z_m) - Q_J(Z_\Lambda) + \frac{\Lambda^2 - m^2}{2q'q} Q'_J(Z_\Lambda) \right) \quad (3.68)$$

$$T_J(q', q) = \frac{1}{2q'q} \left(Z_m Q_J(Z_m) - Z_\Lambda Q_J(Z_\Lambda) + \frac{\Lambda^2 - m^2}{2q'q} Z_\Lambda Q'_J(Z_\Lambda) \right). \quad (3.69)$$

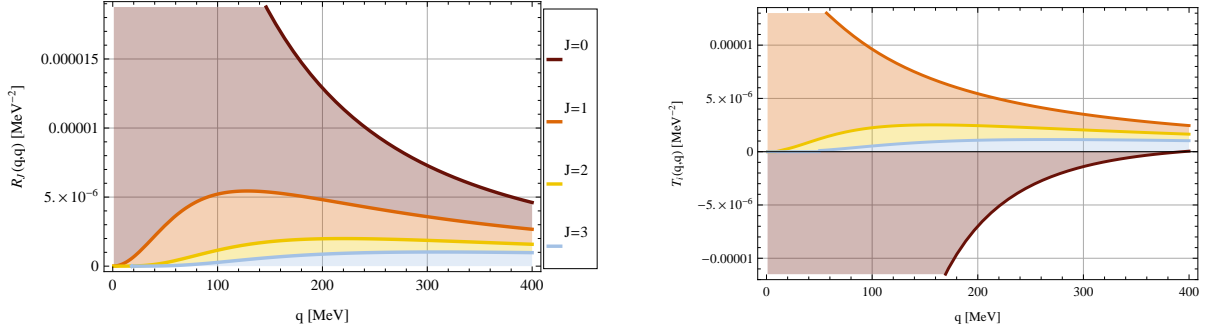


Figure 3.7.: $R_J(q, q)$ and $T_J(q, q)$ for interaction via exchange of a pion ($m_\pi = 138.03$ MeV, $\Lambda_\pi = 1300$ MeV) for total angular momenta $0 \leq J \leq 3$.

In fig. 3.7 these expressions for interaction via exchange of one pion are plotted for $J \leq 3$. We find the main contribution being due to the S -wave ($J = 0$), while the higher partial waves contributions are decreasing with increasing J . Another interesting point is that Z_M is not sensitive to exchange of q and q' . Thus $R_J(q', q)$ and $T_J(q', q)$ behave in the same way and are symmetric to the on-shell line ($q' = q$).

3.9. Singlet-Even- NN Potential

We now can calculate the singlet potential for all mesons using eqs. 3.67-3.69, 3.52 and the values of tab. 3.2. The resulting SE- NN potential is plotted in fig. 3.8. The main contribution to the potential in the plotted energy range is provided by the σ meson and the vector mesons. The pseudoscalar mesons and the δ meson provide smaller contributions.

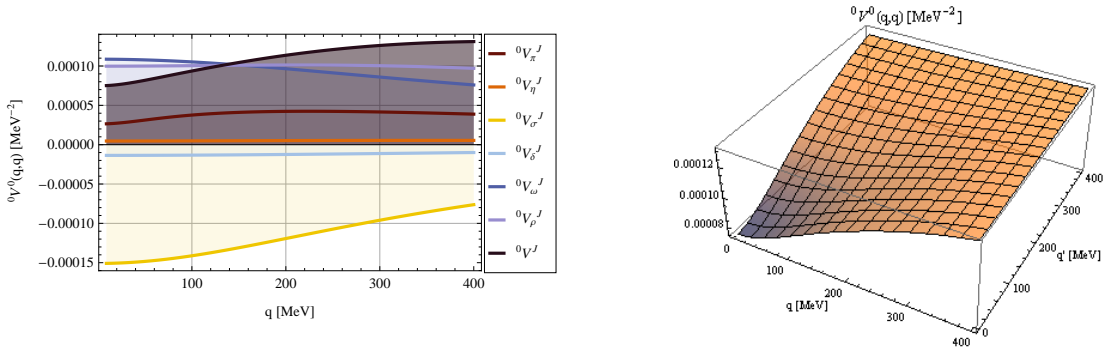


Figure 3.8.: SE- NN potential ${}^0V^0(q', q)$.

3.10. Results

In this section, we want use to the SE- NN potential as test for our numerics and code. The results of our calculations will be compared to theoretical predictions of other models and some experimental values.

3.10.1. Phase Shifts

The phase shifts for the SE- NN potential are calculated using the on-shell R -matrix of the uncoupled channel (eq. 2.58). Inserting the nucleon mass $M_N = 938.919$ MeV leads to the NN propagator

$$G(k, q) = M_N \frac{k^2}{q^2 - k^2} \quad (3.70)$$

In fig. 3.9 the result of this calculation is plotted in comparison to a relativistic Bonn potential (BonnB) [19] and a Nijmegen potential (Nijm93) [27]. The numbers are taken from [1]. Our results are close to the other phase shifts for small momenta, but for higher momenta the deviation from the relativistic BonnB model increases. The consistency with the Nijm93 model is higher, and has the highest deviation for momenta in intermediate range.

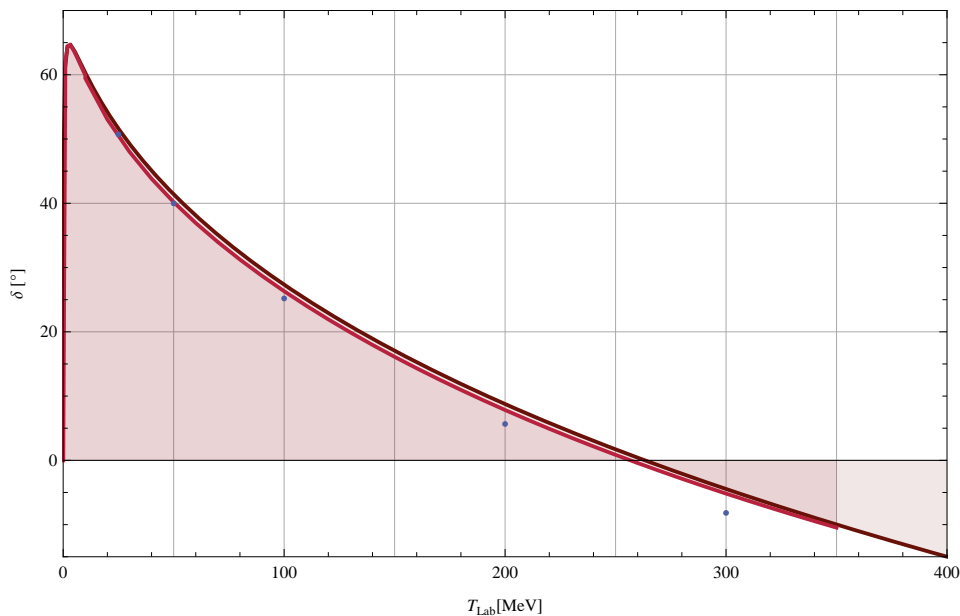


Figure 3.9.: SE-phase shift of NN potentials. Red: Nijm93 [27], dots: BonnB [19], brown: our model.

3.10.2. Cross Sections

The cross section for the SE channel can be calculated using eq. 2.78. The result is plotted in fig. 3.10. Experimental data gives a much higher value: The experimental cross section is 30–70 MeV for $T_{Lab} \geq 100$ MeV [1]. But this is caused by contributions of higher partial waves, which we did not include in our calculation.

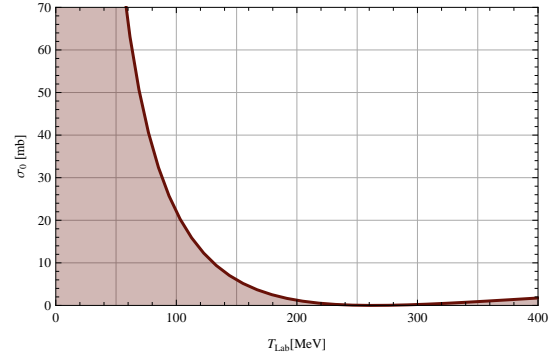


Figure 3.10.: SE-cross section of the NN interaction.

3.10.3. Low-Energy Parameters

The singlet LE parameters were determined by performing a least square fit (as described in section 2.8) over an interval $0.1 \leq q \leq 1.0$ MeV. The numbers are smaller than the experimental values and the theoretical predictions of the relativistic BonnB model. The deviation from the experimental values is 0.84 % for a and 2.8 % for r .

	a [fm]	r [fm]
Experiment [19]	$-23.748(10)$	$2.75(5)$
BonnB [19]	-23.75	2.71
non relativistic	-23.5481	2.6731

Table 3.5.: The table shows low-energy parameters. Parentheses indicate one-standard-deviation uncertainties in the last digits of experimental values.

3.10.4. Quality of Potential and Numerical Calculation

The results of our model are close to the results of other models for the phase shift as well as the experimentally measured low energy parameters. The results could be optimized by using more integration points in the integration procedure for solving the R -matrix equation and optimizing the least square fit interval as well as the degree of the polynomial, but this will not be part of this work. A comparison of cross sections is

not eligible, because the total cross section includes a sum over all partial waves, but only the SE channel is considered in this work.

By now, we find the non-relativistic SE- NN potential of adequate quality and will use it as basis of an YN potential in the next chapter.

4. Hyperon-Nucleon Interaction

This chapter includes the derivation, fitting and test of a YN potential from the NN potential we derived in the previous section. First, the main changes in comparison to the NN potential are pointed out and the characteristics of the treatment of coupled channels are discussed. In the next step, the R -matrix equation is solved in isospin basis and the potential is fitted to the results of the Jülich group [16]. Afterwards, the results in isospin basis are discussed. In the last section, the potential in particle basis is calculated from the isospin basis results and the calculated cross sections as well as the low energy parameters are both discussed and compared to experimental data. The investigations in this section are highly exploratory. In the first place, they are intended as feasibility studies, serving as a foundation for more detailed investigations in the future.

4.1. Hyperons

We want to describe the interaction of nucleons (N) and hyperons (Y) with strangeness $S = -1$, i.e. the Λ and Σ baryons. Nucleons and hyperons both are baryons. Their properties are given in tab. 4.1. In our model we include the same six mesons as in the Bonn model for NN interaction: π , η , ω , ρ , σ , δ . As discussed in the previous chapter, the nucleons are an isodoublet ($I = \frac{1}{2}, I_z = \pm\frac{1}{2}$). The Λ is an isosinglet ($I = 0, I_z = 0$), and the Σ baryons build up an isotriplet ($I = 1, I_z = -1, 0, 1$).

As in NN interaction, the isospin factors of the isovector mesons have to be taken into account. We use the values given in [28] and [24] (tab. 4.2).

4.2. Ansatz

For describing the interaction $YN \rightarrow XN$ in isospin basis, we use potentials with the same structure as the NN potential known from the previous section, but with different coupling strengths. The general formula is:

$$\frac{g_{NN}^2}{4\pi} \rightarrow \frac{g_{NN}g_{XY}}{4\pi}, \quad \frac{f_{NN}}{g_{NN}} \rightarrow \frac{f_{XY}}{\sqrt{g_{NN}g_{XY}}} \quad (4.1)$$

Baryon	Particle	I	Mass [MeV]
Nucleon	N	$\frac{1}{2}$	938.919
	n	$\frac{1}{2}$	938.27231
	p	$\frac{1}{2}$	939.56563
Hyperon	Λ	0	1115.684
	Σ	1	1193.12
	Σ^+	1	1189.37
	Σ^0	1	1192.55
	Σ^-	1	1197.436
	Cascade	Ξ	$\frac{1}{2}$
Ξ^0		$\frac{1}{2}$	1314.90
Ξ^-		$\frac{1}{2}$	1321.32

Table 4.1.: Properties of some baryons [28].

The average masses of multiplets are denoted by N , Σ and Ξ .

	T	η, σ, ω	π, δ, ρ
$NN \rightarrow NN$	0	1	-3
	1	1	1
$\Lambda N \rightarrow \Lambda N$	$\frac{1}{2}$	1	0
$\Lambda N \rightarrow \Sigma N$	$\frac{1}{2}$	0	$\sqrt{3}$
$\Sigma N \rightarrow \Sigma N$	$\frac{1}{2}$	1	-2
	$\frac{3}{2}$	1	1

Table 4.2.: Factors, indicating whether isoscalar mesons are included in the potential, and isospinfactors $\tau_1 \cdot \tau_2$ for isovector mesons [24, 28].

Additionally, the cutoffs of the potential could be varied. Since the variation of couplings and cutoffs would be too extensive for this work, we use a more simple way for obtaining a YN potential. Indeed, as a first ansatz we multiply the NN potential by overall factors:

$${}^0V_{XN \rightarrow YN}^J(q', q) \rightarrow b_{XY} {}^0V_{NN}^J(q', q) \quad (4.2)$$

It should be highlighted in this place, that ${}^0V_{NN}^J(q', q)$ includes the correct isospin factors of the YN interaction given in tab. 4.2. In this work, the latter ansatz is used. We will determine the b_{XY} by fitting theoretical predictions for the phase shifts of the Jülich group [16].

4.3. Masses

In the potential derived in the previous chapter, the masses of the particles are included as $M = M_N$ because only NN scattering is considered. Since our goal is to describe YN interaction, we have to take into account the possibility of different masses. Thus we substitute the original simple expression by another one which includes the masses of the baryons before (M_1 and M_2) and after (M'_1 and M'_2) the scattering as

$$M^2 = \sqrt{M_1 M'_1 M_2 M'_2} \quad (4.3)$$

For uncoupled channels, i.e. $M_i = M'_i$, we find $M^2 = M_1 M_2$. For the scattering of identical particles the relation $M^2 = M_1^2$ is valid and we find a result consistent with the Bonn potential as it is described in [19].

4.4. Conservation of s and Kinematics of Coupled Channels

The coupling between channels of different particle content and different masses is performed over the conserved quantity s (eq. 2.3), which in c.m. frame can be calculated as

$$s = (E_1 + E_2)^2, \quad E_i = \sqrt{q^2 + M_i^2} \quad (4.4)$$

Since s is conserved, it has the same value in both channels. The on-shell momenta are depending on the masses in the channels:

$$q_s^2 = q_{1s}^2 = q_{2s}^2 = \frac{1}{4s} \left(s - (M_1^2 - M_2^2)^2 \right) \left(s - (M_1 + M_2)^2 \right) \quad (4.5)$$

The threshold for each channel is determined by the minimal value of $q_s = 0$. The minimal s is then given by

$$s_{ij} = (M_i + M_j)^2 \Leftrightarrow \sqrt{s_{ij}} = M_i + M_j \quad (4.6)$$

During the calculation we have to take care, which channel we are actually calculating. s is always defined by the elastic entrance channel, containing asymptotically an incoming plane wave. The appropriate on-shell momentum has to be used, e.g. V_{XY}^I means that the initial momentum has to be in XN channel, while the final momentum is in YN channel.

Additionally, in the parts of the system of equations, which is describing the interaction in the channel with heavier particle content, the integration has to be executed over sampling points in the heavier system, while in the parts with interaction in the channel with lighter particle content the corresponding on-shell momenta of the lighter channel must be used. The transformation can be performed using eq. 4.5.

4.5. Isospin Basis

Sorting the possible NN and YN combinations after total isospin T and strangeness S gives the four possible isospin values $T = 0, \frac{1}{2}, 1, \frac{3}{2}, 2$ with $-4 \leq S \leq 0$ as shown in tab. 4.3. We will concentrate on the channels with one strange quark (i.e. $S = -1$), where two values of isospin are possible (i.e. $T = \frac{1}{2}, \frac{3}{2}$). Since the Λ hyperon is an isosinglet, a ΛN system can couple only to a total isospin of $\frac{1}{2}$, while ΣN scattering is possible in both isospin channels. In fig. 4.1 the on shell momenta for isospin channels with $S \geq -1$ are plotted in dependency of s , their thresholds are given in tab. 4.4.

	$T = 0$	$T = \frac{1}{2}$	$T = 1$	$T = \frac{3}{2}$	$T = 2$
$S = 0$	NN		NN		
$S = -1$		$\Lambda N, \Sigma N$		ΣN	
$S = -2$	$\Lambda\Lambda, \Xi N, \Sigma\Sigma$		$\Xi N, \Sigma\Lambda, \Sigma\Sigma$		$\Sigma\Sigma$
$S = -3$		$\Xi\Lambda, \Xi\Sigma$		$\Xi\Sigma$	
$S = -4$	$\Xi\Xi$		$\Xi\Xi$		

Table 4.3.: Channels in isospin basis [28], blue: this section

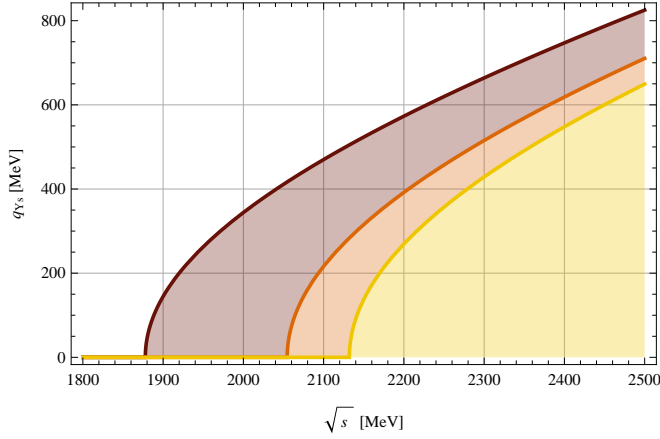


Figure 4.1.: Relation between total energy \sqrt{s} and on-shell momentum q_{Ys} . Brown: NN , orange: ΛN , yellow: ΣN .

Channel	$s [10^6 \text{ MeV}^2]$	$\sqrt{s} [\text{MeV}]$
NN	3.52528	1877.84
ΛN	4.22139	2054.60
ΣN	4.54558	2132.04

Table 4.4.: Thresholds for isospin channels with $S \geq -1$.

4.5.1. $T = \frac{3}{2}$ Channel

In the $T = \frac{3}{2}$ channel only ΣN scattering is possible, thus we can solve the R -matrix equation in the same way as before and write in operator notation according to 2.39:

$$R_{\Sigma\Sigma}^{\frac{3}{2}} = V_{\Sigma\Sigma}^{\frac{3}{2}} + V_{\Sigma\Sigma}^{\frac{3}{2}} G_{\Sigma} R_{\Sigma\Sigma}^{\frac{3}{2}} \quad (4.7)$$

Here, we only wrote the isospin and the hyperons before and after the scattering as subscripts, neglecting the nucleons: V_{XY}^T means the potential for reaction $XN_X \rightarrow YN_Y$ with isospin T and $X, Y = \Lambda, \Sigma$ (accordingly for R_{XY}^T).

The parameters for this channel now can be determined by comparing our calculations to the results of other groups, especially the Jülich group (Haidenbauer et al., [16]), who did similar calculations in isospin basis.

The parameters of the NN potential were used as starting values, i.e. $b_{\Sigma\Sigma} = 1$. The only difference to the original NN potential are the isospin factors (tab. 4.2). For the $\Sigma N^{\frac{3}{2}}$ channel these factors have the same values as for the NN channel with $T = 1$. We find the overall scaling factor to be $b_{\Sigma\Sigma} = 0.79$. The result is plotted in fig. 4.2.

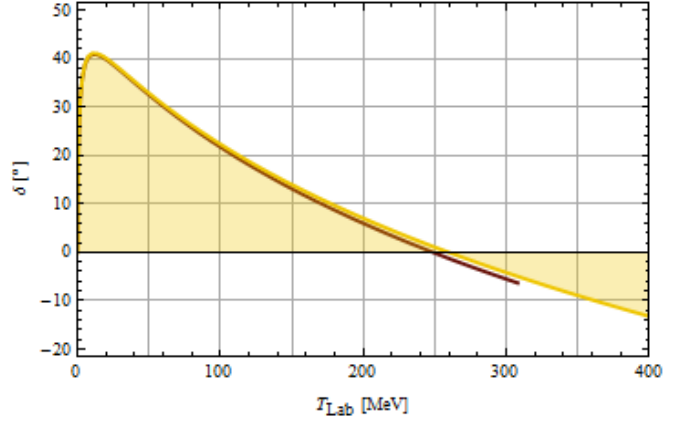


Figure 4.2.: SE-phase shifts in $\Sigma N^{\frac{3}{2}}$ channel. Brown line: Jülich group [16], yellow shaded area: fit.

4.5.2. $T = \frac{1}{2}$ Channels

In the $T = \frac{1}{2}$ channel the so called $\Lambda\Sigma$ coupling occurs. This means the transition $\Lambda N \leftrightarrow \Sigma N$ is available and a separate treatment of the channels in the form

$$R_{\Sigma\Sigma}^{\frac{1}{2}} = V_{\Sigma\Sigma}^{\frac{1}{2}} + V_{\Sigma\Sigma}^{\frac{1}{2}} G_{\Sigma} R_{\Sigma\Sigma}^{\frac{1}{2}} \quad (4.8)$$

$$R_{\Lambda\Lambda}^{\frac{1}{2}} = V_{\Lambda\Lambda}^{\frac{1}{2}} + V_{\Lambda\Lambda}^{\frac{1}{2}} G_{\Lambda} R_{\Lambda\Lambda}^{\frac{1}{2}} \quad (4.9)$$

is no longer sufficient. In order to account for including the $\Lambda\Sigma$ -coupling, we must change to matrix formulation and write for R , V and G in 2.39

$$R \rightarrow \begin{pmatrix} R_{\Lambda\Lambda}^{\frac{1}{2}} & R_{\Lambda\Sigma}^{\frac{1}{2}} \\ R_{\Sigma\Lambda}^{\frac{1}{2}} & R_{\Sigma\Sigma}^{\frac{1}{2}} \end{pmatrix}, \quad V \rightarrow \begin{pmatrix} V_{\Lambda\Lambda}^{\frac{1}{2}} & V_{\Lambda\Sigma}^{\frac{1}{2}} \\ V_{\Sigma\Lambda}^{\frac{1}{2}} & V_{\Sigma\Sigma}^{\frac{1}{2}} \end{pmatrix}, \quad G \rightarrow \begin{pmatrix} G_{\Lambda} & 0 \\ 0 & G_{\Sigma} \end{pmatrix}. \quad (4.10)$$

Where $V_{\Lambda\Sigma}^T$ and $V_{\Sigma\Lambda}^T$ are the transition potentials between the channels, causing corresponding non-diagonal terms in the R-matrix.

By executing the matrix multiplications we arrive at

$$\begin{aligned} \begin{pmatrix} R_{\Lambda\Lambda}^{\frac{1}{2}} & R_{\Lambda\Sigma}^{\frac{1}{2}} \\ R_{\Sigma\Lambda}^{\frac{1}{2}} & R_{\Sigma\Sigma}^{\frac{1}{2}} \end{pmatrix} &= \begin{pmatrix} V_{\Lambda\Lambda}^{\frac{1}{2}} & V_{\Lambda\Sigma}^{\frac{1}{2}} \\ V_{\Sigma\Lambda}^{\frac{1}{2}} & V_{\Sigma\Sigma}^{\frac{1}{2}} \end{pmatrix} + \begin{pmatrix} V_{\Lambda\Lambda}^{\frac{1}{2}} & V_{\Lambda\Sigma}^{\frac{1}{2}} \\ V_{\Sigma\Lambda}^{\frac{1}{2}} & V_{\Sigma\Sigma}^{\frac{1}{2}} \end{pmatrix} \begin{pmatrix} G_{\Lambda} & 0 \\ 0 & G_{\Sigma} \end{pmatrix} \begin{pmatrix} R_{\Lambda\Lambda}^{\frac{1}{2}} & R_{\Lambda\Sigma}^{\frac{1}{2}} \\ R_{\Sigma\Lambda}^{\frac{1}{2}} & R_{\Sigma\Sigma}^{\frac{1}{2}} \end{pmatrix} \\ &= \begin{pmatrix} V_{\Lambda\Lambda}^{\frac{1}{2}} & V_{\Lambda\Sigma}^{\frac{1}{2}} \\ V_{\Sigma\Lambda}^{\frac{1}{2}} & V_{\Sigma\Sigma}^{\frac{1}{2}} \end{pmatrix} + \begin{pmatrix} V_{\Lambda\Lambda}^{\frac{1}{2}} G_{\Lambda} & V_{\Lambda\Sigma}^{\frac{1}{2}} G_{\Sigma\Sigma} \\ V_{\Sigma\Lambda}^{\frac{1}{2}} G_{\Lambda} & V_{\Sigma\Sigma}^{\frac{1}{2}} G_{\Sigma\Sigma} \end{pmatrix} \begin{pmatrix} R_{\Lambda\Lambda}^{\frac{1}{2}} & R_{\Lambda\Sigma}^{\frac{1}{2}} \\ R_{\Sigma\Lambda}^{\frac{1}{2}} & R_{\Sigma\Sigma}^{\frac{1}{2}} \end{pmatrix} \\ &= \begin{pmatrix} V_{\Lambda\Lambda}^{\frac{1}{2}} & V_{\Lambda\Sigma}^{\frac{1}{2}} \\ V_{\Sigma\Lambda}^{\frac{1}{2}} & V_{\Sigma\Sigma}^{\frac{1}{2}} \end{pmatrix} + \begin{pmatrix} V_{\Lambda\Lambda}^{\frac{1}{2}} G_{\Lambda} R_{\Lambda\Lambda}^{\frac{1}{2}} + V_{\Lambda\Sigma}^{\frac{1}{2}} G_{\Sigma} R_{\Sigma\Lambda}^{\frac{1}{2}} & V_{\Lambda\Lambda}^{\frac{1}{2}} G_{\Lambda} R_{\Lambda\Sigma}^{\frac{1}{2}} + V_{\Lambda\Sigma}^{\frac{1}{2}} G_{\Sigma} R_{\Sigma\Sigma}^{\frac{1}{2}} \\ V_{\Sigma\Lambda}^{\frac{1}{2}} G_{\Lambda} R_{\Lambda\Lambda}^{\frac{1}{2}} + V_{\Sigma\Sigma}^{\frac{1}{2}} G_{\Sigma} R_{\Sigma\Lambda}^{\frac{1}{2}} & V_{\Sigma\Lambda}^{\frac{1}{2}} G_{\Lambda} R_{\Lambda\Sigma}^{\frac{1}{2}} + V_{\Sigma\Sigma}^{\frac{1}{2}} G_{\Sigma} R_{\Sigma\Sigma}^{\frac{1}{2}} \end{pmatrix}. \end{aligned} \quad (4.11)$$

This expression can be written as two systems of coupled R -matrix equations, which are

$$R_{\Lambda\Lambda}^{\frac{1}{2}} = V_{\Lambda\Lambda}^{\frac{1}{2}} + V_{\Lambda\Lambda}^{\frac{1}{2}} G_{\Lambda} R_{\Lambda\Lambda}^{\frac{1}{2}} + V_{\Lambda\Sigma}^{\frac{1}{2}} G_{\Sigma} R_{\Sigma\Lambda}^{\frac{1}{2}} \quad (4.12)$$

$$R_{\Sigma\Lambda}^{\frac{1}{2}} = V_{\Sigma\Lambda}^{\frac{1}{2}} + V_{\Sigma\Lambda}^{\frac{1}{2}} G_{\Lambda} R_{\Lambda\Lambda}^{\frac{1}{2}} + V_{\Sigma\Sigma}^{\frac{1}{2}} G_{\Sigma} R_{\Sigma\Lambda}^{\frac{1}{2}} \quad (4.13)$$

and

$$R_{\Lambda\Sigma}^{\frac{1}{2}} = V_{\Lambda\Sigma}^{\frac{1}{2}} + V_{\Lambda\Lambda}^{\frac{1}{2}} G_{\Lambda} R_{\Lambda\Sigma}^{\frac{1}{2}} + V_{\Lambda\Sigma}^{\frac{1}{2}} G_{\Sigma}^{\frac{1}{2}} R_{\Sigma\Sigma}^{\frac{1}{2}} \quad (4.14)$$

$$R_{\Sigma\Sigma}^{\frac{1}{2}} = V_{\Sigma\Sigma}^{\frac{1}{2}} + V_{\Sigma\Lambda}^{\frac{1}{2}} G_{\Lambda} R_{\Lambda\Sigma}^{\frac{1}{2}} + V_{\Sigma\Sigma}^{\frac{1}{2}} G_{\Sigma} R_{\Sigma\Sigma}^{\frac{1}{2}}. \quad (4.15)$$

The numerical values of the thresholds in isospin bases are given in table 4.4. According to this results we have to perform the transitions of eq. 4.10 at $s = s_{\Sigma N}$. Below that value, it is sufficient to calculate the uncoupled ΛN channel alone, i.e. using eq. 4.9.

4.5.3. Fitting Procedure

The fit of the coupled $T = \frac{1}{2}$ channels is performed as follows. In the first step the ΛN interaction is fitted for lower energies, where $\Lambda\Sigma$ -coupling does not occur. The NN coupling values are chosen as starting point, i.e. $b_{\Lambda\Lambda} = 1$. A good description of the Jülich data below the threshold is achieved for $b_{\Lambda\Lambda} = 0.86$ (fig. 4.3).

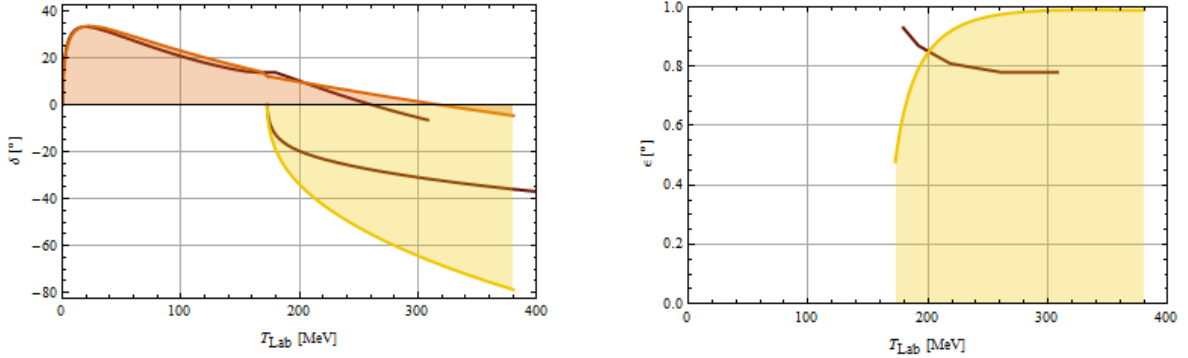


Figure 4.3.: Fitting the SE-eigenphase shifts and mixing parameter in $T = \frac{1}{2}$ channel. Brown line: Jülich group [16], orange: fit for δ_+ , yellow: fit for δ_- and ϵ .

In the second step the ΣN coupling constants already known from the $\Sigma N^{\frac{3}{2}}$ fit are used and the $\Lambda\Sigma$ transition parameters are varied, starting at $b_{\Lambda\Sigma} = 1$ and leading to an overall scaling of $b_{\Lambda\Sigma} = 0.02$. Here the fit was done to the ΣN phase shift as well as the mixing parameter ϵ . The fit shows a larger deviation from the data, especially the ΣN

phase shift shows a much larger value than the predictions from [16]. The absolute value of δ_- could be lowered by increasing $b_{\Lambda\Sigma}$, but this would result in a larger deviation in ϵ at the same time.

4.6. Results

Using the results for the scaling factors given in tab. 4.5, we can plot the YN potential in isospin base and calculate cross sections and low energy parameters. The outcome of this calculations is discussed in this section.

Channel $YN \rightarrow YN$	Scaling factor b_{XY}
$\Lambda N \rightarrow \Lambda N$	0.86
$\Sigma N \rightarrow \Sigma N$	0.79
$\Lambda N \rightarrow \Sigma N$	0.02

Table 4.5.: Scalings of the YN potential.

4.6.1. Potential

The SE- ΛN potential is plotted in fig. 4.4. The contributions come from the isoscalar mesons only. The shape of the potential is similar to the SE- NN potential, but for low momenta the SE- ΛN potential is negative.

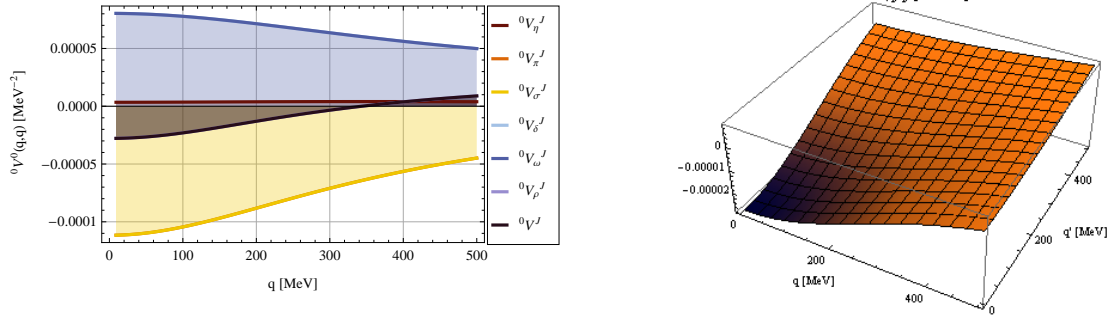


Figure 4.4.: SE- ΛN potential ${}^0V^0(q', q)$.

The SE- $\Sigma N^{\frac{1}{2}}$ potential is shown in fig. 4.5. It is negative for small momenta and has an amplitude in the order of 10^{-3} MeV^{-2} . Hence, it is three times larger than the SE- ΛN potential. In turn, the SE- $\Sigma N^{\frac{3}{2}}$ potential (plotted in fig. 4.6) is positive and has a smaller amplitude, which is in the order of the SE- ΛN potential. The difference between the ΣN potentials of different isospin is caused by the isospin factors. In $T = \frac{1}{2}$ channels they are two times larger than in the $\Sigma N^{\frac{3}{2}}$ channel and have a negative sign.

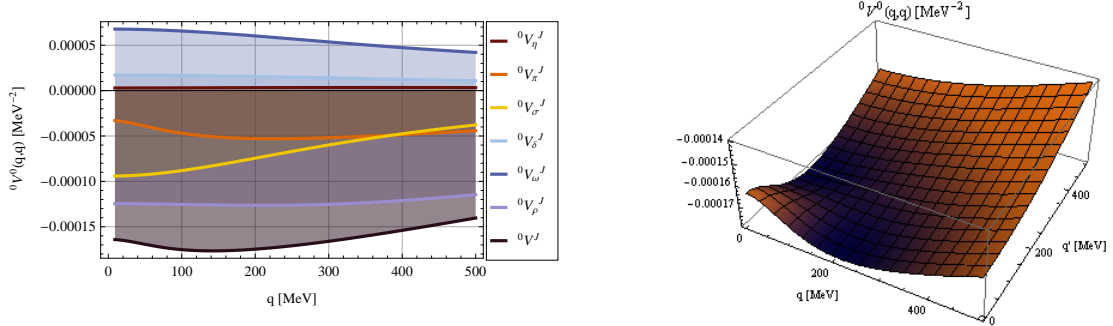


Figure 4.5.: SE- $\Sigma N^{\frac{1}{2}}$ potential ${}^0V^0(q', q)$.

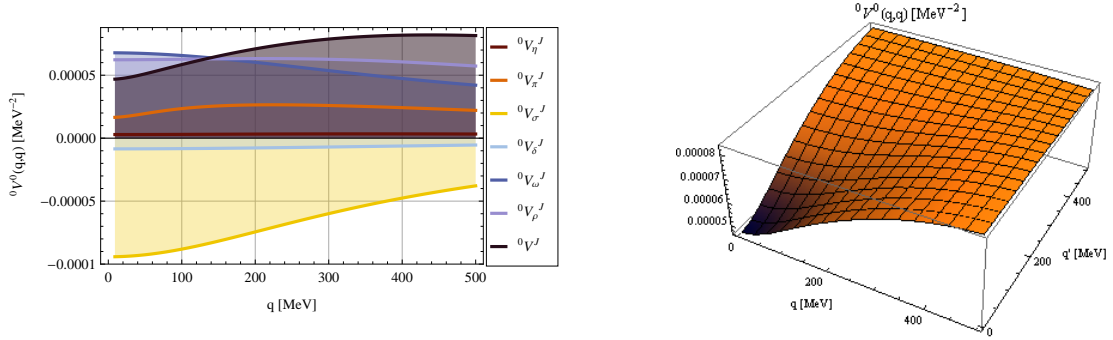


Figure 4.6.: SE- $\Sigma N^{\frac{3}{2}}$ potential ${}^0V^0(q', q)$.

The $\Lambda\Sigma$ transition potential is plotted in fig. 4.7. The on-shell potential here is not given by same values for q and q' , but by the on-shell momenta belonging to the same total energy \sqrt{s} in the two systems before and after the scattering. Therefore, the on-shell potential decreases as q_s increases, although the potential has its minimum for $q = q' = 0$ MeV.

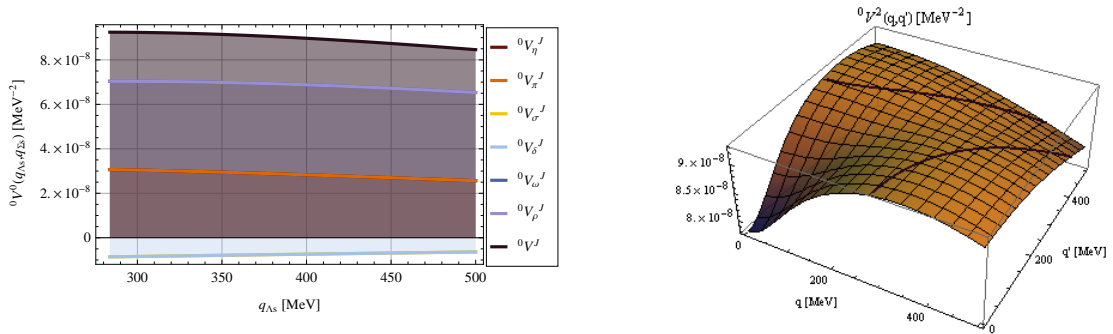


Figure 4.7.: SE- $\Lambda\Sigma$ transition potential ${}^0V^0(q', q)$. Black lines are marking the on-shell potential.

4.6.2. Cross Sections

The cross sections can be determined from the eigenphase shifts and the mixing parameter as described in section 2.7. The results for the $T = \frac{1}{2}$ channels are shown in fig. 4.8.

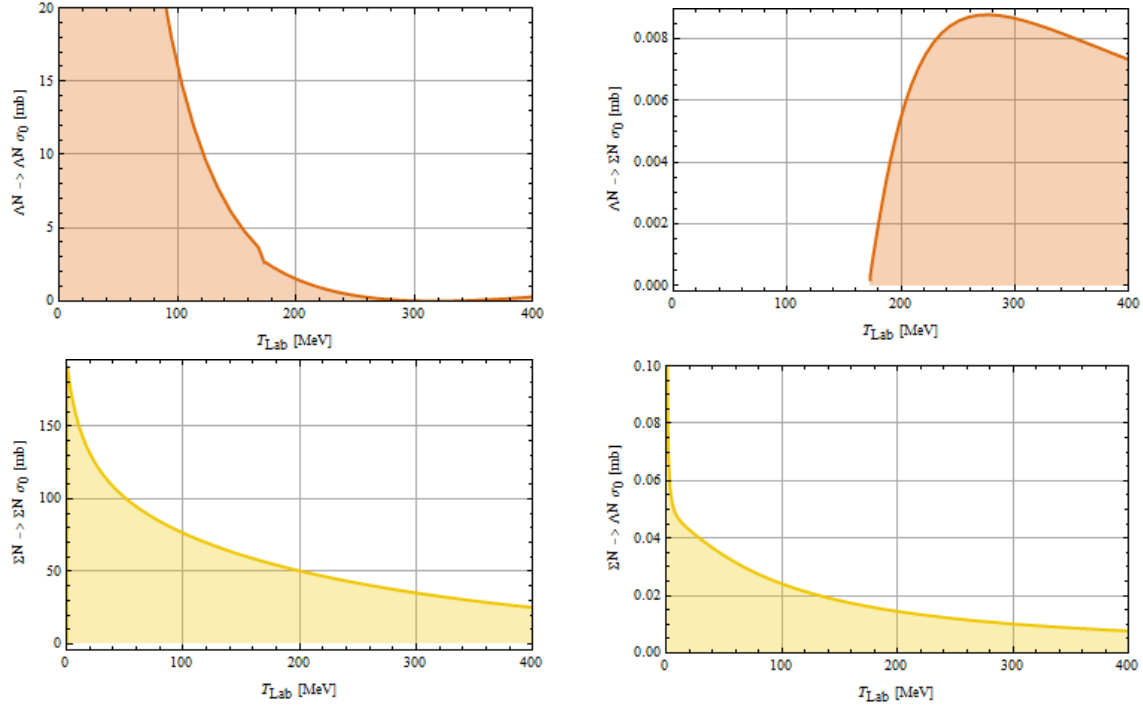


Figure 4.8.: SE-cross sections of the $\Lambda N \leftrightarrow \Sigma N^{\frac{1}{2}}$ system.

As long as no $\Lambda\Sigma$ coupling occurs, the $\Lambda N \rightarrow \Lambda N$ cross section is decreasing continuous. At the coupling threshold of $\sqrt{s} = 2132.04$ MeV, which is corresponding to a laboratory energy of the incoming Λ of $T_{Lab} = 172.644$ MeV, there is a kink where the cross section decreases instantaneous. At the same moment the threshold is achieved, the $\Lambda N \rightarrow \Sigma N$ cross section increases and reaches its maximum at an laboratory energy of about 280 MeV, but keeps less than 10^{-2} mb. The minimal value of the $\Lambda N \rightarrow \Lambda N$ cross section is found to be at an T_{Lab} of about 320 MeV, where the cross section is almost zero.

The cross sections of the $\Sigma N^{\frac{1}{2}}$ system show less structure. The $\Sigma N^{\frac{1}{2}} \rightarrow \Sigma N^{\frac{1}{2}}$ cross section as well as the $\Sigma N \rightarrow \Lambda N$ cross section have the highest values for $T_{Lab} = 0$ MeV and are decreasing continuous from there. Moreover, the $\Sigma N \rightarrow \Lambda N$ cross section is more than three orders of magnitude smaller than the $\Sigma N^{\frac{1}{2}} \rightarrow \Sigma N^{\frac{1}{2}}$ cross section. In short, the coupling between ΛN and ΣN channels is small.

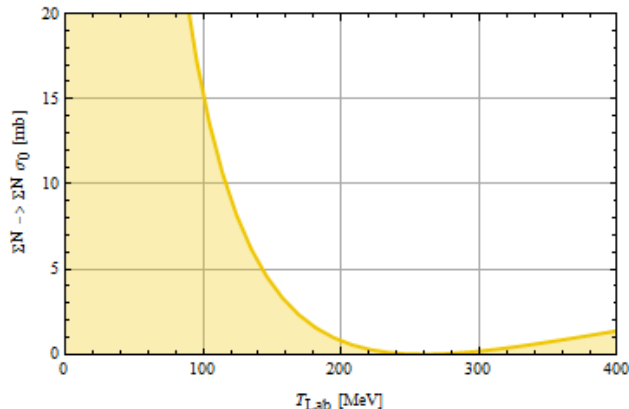


Figure 4.9.: $\Sigma N^{\frac{3}{2}}$ SE cross section.

The $\Sigma N^{\frac{3}{2}}$ cross section as shown in fig. 4.9 has a similar shape as the $\Lambda N \rightarrow \Lambda N$ cross section, but does not have a kink.

4.6.3. LE Parameters

For uncoupled channels, we can calculate the LE parameters as introduced in section 2.8. For the $\Sigma N^{\frac{1}{2}}$ channel the calculation is more complicated, because the LE parameters have to be calculated from physical phase shifts instead of eigenphase shifts. The calculation is not as simple as for the uncoupled channels and the LE parameters become complex above the threshold. In this work, we restrict ourselves to calculating the so called eigen-LE parameters. In order to do this, we use the eigenphase shift δ_- instead of the physical phase shift $\delta_{\Sigma\Sigma}$ in eq. 2.79.

Our notation is as follows: The eigen-LE parameters calculated from δ_- are named by the channel opening at the threshold when δ_- occurs, and marked with the prefix eigen. Results are given in tab. 4.6.

The scattering length (a_s) of the YN isospin channels is found to have lower absolute values than in NN scattering. The ΛN channel and the $\Sigma N^{\frac{3}{2}}$ channel have negative scattering length. The eigen scattering length of the $\Sigma N^{\frac{1}{2}}$ channel is positive.

	a [fm]	r [fm]
ΛN	-2.4037	2.5745
$\Sigma N^{\frac{1}{2}}$ eigen	1.2480	-1.052
$\Sigma N^{\frac{3}{2}}$	-4.7493	3.3596

Table 4.6.: (Eigen-) LE parameters for Isospin channels

The effective ranges (r_s) of the ΛN channel and the $T = \frac{3}{2}$ channel are positive and in the same order of magnitude than the NN effective range. The eigen-effective range of the $\Sigma N^{\frac{1}{2}}$ channel is a negative, in contrast. Since we are comparing eigen and physical LE parameters, the deviant behavior of the eigen-LE parameters is not unreckoned.

The interval and degree of the fitting polynomial in the least square fit are optimized for NN interaction. Thus, the results for YN interaction may not be as accurate as they are for NN interaction and further studies on this topic are needed.

4.7. Particle Basis

In the particle basis the physical particles are combined and sorted after total strangeness S and total charge Q , as shown in tab. 4.8. This results in 4 channels with $S = -1$. Two of them are uncoupled, two are coupled. The on-shell momenta in dependency of s and the thresholds of the $S = -1$ channels are given in fig. 4.10 and tab. 4.7. An advantage of the particle basis is the possibility to include the Coulomb interaction, which is neglected in our calculations. An additional advantage is the possibility to compare the results to experimental cross sections immediately.

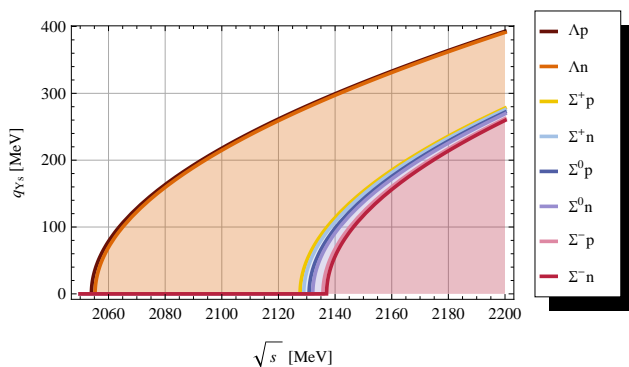


Figure 4.10.: Relation between mandelstam s and on shell momentum q_{Ys} in particle basis.

Channel	s [10^6 MeV 2]	\sqrt{s} [MeV]
pp	3.52142	1876.54
np	3.52628	1877.84
nn	3.53113	1879.13
Λp	4.21874	2053.96
Λn	4.22405	2055.25
$\Sigma^+ p$	4.52686	2127.64
$\Sigma^+ n$	4.53237	2128.94
$\Sigma^0 p$	4.5404	2130.82
$\Sigma^0 n$	4.54592	2132.12
$\Sigma^- p$	4.56125	2135.71
$\Sigma^- n$	4.56678	2137.00

Table 4.7.: Thresholds of channels in particle basis.

We find an drawback, because we now have up to three channels, which can couple and thus the system of equations to be solved becomes more complicated. We will avoid this by approximating three channel coupling by two channel coupling.

Since the YN potential is defined in isospin basis, it has to be transformed into the particle basis by performing an isospin rotation. We will use the transformations as given in [24].

	$Q = -2$	$Q = -1$	$Q = 0$	$Q = 1$	$Q = 2$
$S = 0$			nn	np	pp
$S = -1$		$\Sigma^- n$	$\Lambda n, \Sigma^0 n, \Sigma^- p$	$\Lambda p, \Sigma^+ n, \Sigma^0 p$	$\Sigma^+ p$
$S = -2$	$\Sigma^- \Sigma^-$	$\Xi^- n, \Sigma^- \Lambda, \Sigma^- \Sigma^0$	$\Lambda \Lambda, \Xi^0 n, \Xi^- p, \Sigma^0 \Lambda, \Sigma^0 \Sigma^0, \Sigma^- \Sigma^+$		$\Sigma^+ \Sigma^+$
$S = -3$	$\Xi^- \Sigma^-$	$\Xi^- \Lambda, \Xi^0 \Sigma^-, \Xi^- \Sigma^0$	$\Xi^0 \Lambda, \Xi^0 \Sigma^0, \Xi^- \Sigma^+$	$\Xi^0 \Sigma^+$	
$S = -4$	$\Xi^- \Xi^-$	$\Xi^- \Xi^0$	$\Xi^0 \Xi^0$		

Table 4.8.: Channels in particle basis [28], blue: part of this section.

4.7.1. Uncoupled Channels

The $Q = -1$ and the $Q = +2$ channels do not couple with any other channel and thus only consist of the $T = \frac{3}{2}$ part of the ΣN potential [24]. The only difference to the $T = \frac{3}{2}$ calculations in the previous chapter is the substitution of the physical particle masses. For the $Q = -1$ channel we find the formulas:

$$V_{\Sigma^- \Sigma^-} = V_{\Sigma \Sigma}^{\frac{3}{2}}, \quad M_{\Sigma} \rightarrow M_{\Sigma^-}, \quad M_N \rightarrow M_n \quad (4.16)$$

$$R_{\Sigma^- \Sigma^-} = V_{\Sigma^- \Sigma^-} + V_{\Sigma^- \Sigma^-} G_{\Sigma^-} R_{\Sigma^- \Sigma^-} \quad (4.17)$$

totally analogous, we find for the $Q = +2$ channel:

$$V_{\Sigma^+ \Sigma^+} = V_{\Sigma \Sigma}^{\frac{3}{2}}, \quad M_{\Sigma} \rightarrow M_{\Sigma^+}, \quad M_N \rightarrow M_p \quad (4.18)$$

$$R_{\Sigma^+ \Sigma^+} = V_{\Sigma^+ \Sigma^+} + V_{\Sigma^+ \Sigma^+} G_{\Sigma^+} R_{\Sigma^+ \Sigma^+} \quad (4.19)$$

The potentials are very similar to the $\Sigma N^{\frac{3}{2}}$ potential. This can be understood by comparing the masses of the channels in isospin and particle basis:

$$\frac{M_{\Sigma} M_N}{M_{\Sigma^-} M_n} = 0.995709, \quad \frac{M_{\Sigma} M_N}{M_{\Sigma^+} M_p} = 1.00384 \quad (4.20)$$

From this calculation we find a difference of about four percent to the isospin basis potential. The main difference between the isospin and particle basis potentials is caused by different on shell momenta belonging to the same s .

From there, the phase shifts and cross sections of the uncoupled particle basis channels are found to be almost identical to the results for the $T = \frac{3}{2}$ channel in isospin basis, as shown in figs. 4.11 and 4.12.

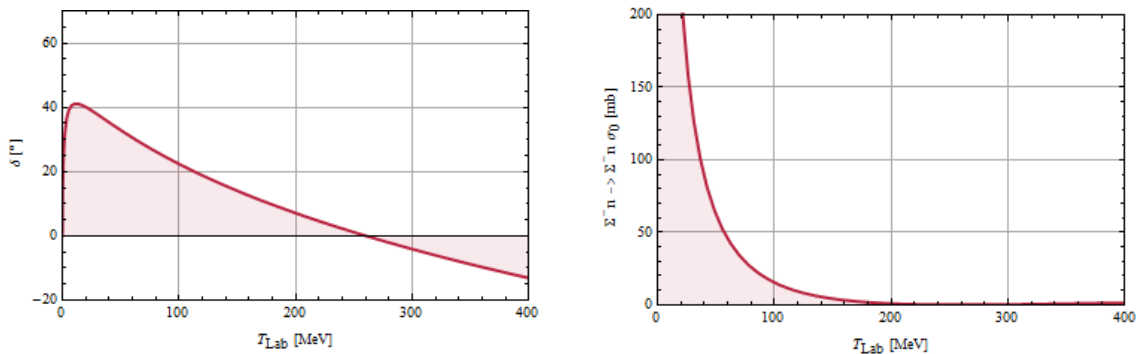


Figure 4.11.: $Q = -1$ SE-phase shifts and cross section (Σ^-n interaction).

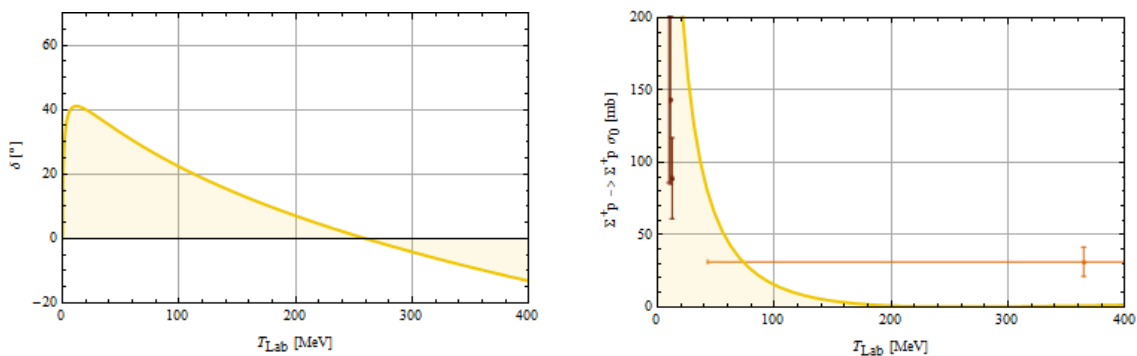


Figure 4.12.: $Q = 2$ SE-phase shifts and cross section (Σ^+p interaction). Data taken from [1], brown: DO66 [11], orange: CH70 [7].

For Σ^+p scattering experimental data is available. The experimental values are taken from [1] and named in the same way as there. The cross section in fig. 4.12 is much larger than the experimental data for low laboratory energies and too low for higher energies. On the one hand, this is caused by the fact that only the SE channel has been taken into account. The inclusion of higher partial waves would lead to an increase of the cross section for higher energies. On the other hand, we determined our YN potential by fitting to theoretical predictions of phase shifts. A fit to the cross section probably would lead to a better description of these data.

The results for the low-energy parameters are given in tab. 4.9. They are found to be close to the $\Sigma N^{\frac{3}{2}}$ results in the isospin basis (tab. 4.6). The Nijmegen models NSC97a-f [24] predict $a_s \approx -4.3$ fm for Σ^+p and $a_s \approx -6$ fm for Σ^-n .

Channel	a [fm]	r [fm]
Σ^-n	-4.7551	3.3096
Σ^+p	-4.7441	3.3235

Table 4.9.: Low-energy parameters of uncoupled channels

4.7.2. $Q = 1$ Channels

For the $Q = 1$ state, three different particle combinations are possible:

$$\Lambda p, \Sigma^+ n, \text{ and } \Sigma^0 p.$$

The thresholds are given in 4.7 while the on-shell momenta for $Q = 1$ are shown in fig. 4.13. Since the Λ is about 77 MeV lighter than the Σ s, but Σ^+ and Σ^0 show a mass difference of about 3 MeV, only, the Λp channel opens at a by far lower total energy while the ΣN channels open short after another.

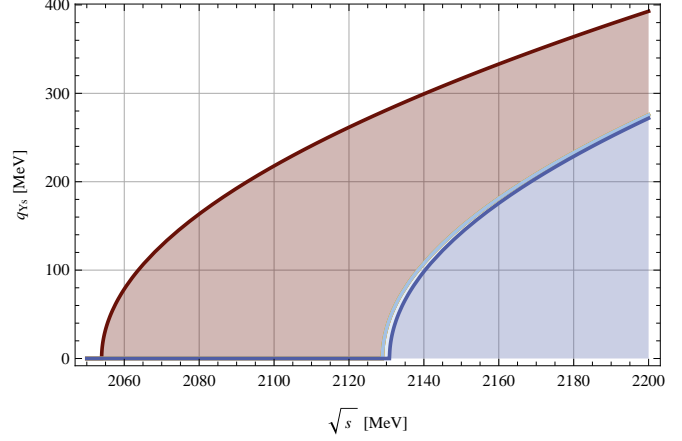


Figure 4.13.: Relation between total energy s and on-shell momentum q_{Ys} for $Q = 1$ channels. Legend as in 4.1.

As for the uncoupled channels, the potential again has to be determined in terms of an isospin rotation. According to [24] this yields:

$$\begin{pmatrix} V_{\Lambda\Lambda} & V_{\Lambda\Sigma^+} & V_{\Lambda\Sigma^0} \\ V_{\Sigma^+\Lambda} & V_{\Sigma^+\Sigma^+} & V_{\Sigma^+\Sigma^0} \\ V_{\Sigma^0\Lambda} & V_{\Sigma^0\Sigma^+} & V_{\Sigma^0\Sigma^0} \end{pmatrix} = \begin{pmatrix} V_{\Lambda\Lambda} & \sqrt{\frac{2}{3}}V_{\Lambda\Sigma} & -\sqrt{\frac{1}{3}}V_{\Lambda\Sigma} \\ \sqrt{\frac{2}{3}}V_{\Sigma\Lambda} & \frac{2}{3}V_{\Sigma\Sigma}^{\frac{1}{2}} + \frac{1}{3}V_{\Sigma\Sigma}^{\frac{3}{2}} & \frac{\sqrt{2}}{3} \left[V_{\Sigma\Sigma}^{\frac{3}{2}} - V_{\Sigma\Sigma}^{\frac{1}{2}} \right] \\ -\sqrt{\frac{1}{3}}V_{\Sigma\Lambda} & \frac{\sqrt{2}}{3} \left[V_{\Sigma\Sigma}^{\frac{3}{2}} - V_{\Sigma\Sigma}^{\frac{1}{2}} \right] & \frac{1}{3}V_{\Sigma\Sigma}^{\frac{1}{2}} + \frac{2}{3}V_{\Sigma\Sigma}^{\frac{3}{2}} \end{pmatrix} \quad (4.21)$$

Since the channels are opening successive one after another, we find a matrix structure in the R -matrix equation:

$$V_{\Lambda\Lambda} \xrightarrow{s \geq s_{\Sigma^+ n}} \begin{pmatrix} V_{\Lambda\Lambda} & V_{\Lambda\Sigma^+} \\ V_{\Sigma^+\Lambda} & V_{\Sigma^+\Sigma^+} \end{pmatrix} \xrightarrow{s \geq s_{\Sigma^0 p}} \begin{pmatrix} V_{\Lambda\Lambda} & V_{\Lambda\Sigma^+} & V_{\Lambda\Sigma^0} \\ V_{\Sigma^+\Lambda} & V_{\Sigma^+\Sigma^+} & V_{\Sigma^+\Sigma^0} \\ V_{\Sigma^0\Lambda} & V_{\Sigma^0\Sigma^+} & V_{\Sigma^0\Sigma^0} \end{pmatrix} \quad (4.22)$$

$$R_{\Lambda\Lambda} \xrightarrow{s \geq s_{\Sigma^+ n}} \begin{pmatrix} R_{\Lambda\Lambda} & R_{\Lambda\Sigma^+} \\ R_{\Sigma^+\Lambda} & R_{\Sigma^+\Sigma^+} \end{pmatrix} \xrightarrow{s \geq s_{\Sigma^0 p}} \begin{pmatrix} R_{\Lambda\Lambda} & R_{\Lambda\Sigma^+} & R_{\Lambda\Sigma^0} \\ R_{\Sigma^+\Lambda} & R_{\Sigma^+\Sigma^+} & R_{\Sigma^+\Sigma^0} \\ R_{\Sigma^0\Lambda} & R_{\Sigma^0\Sigma^+} & R_{\Sigma^0\Sigma^0} \end{pmatrix} \quad (4.23)$$

$$G_{\Lambda} \xrightarrow{s \geq s_{\Sigma^+ n}} \begin{pmatrix} G_{\Lambda} & 0 \\ 0 & G_{\Sigma^+} \end{pmatrix} \xrightarrow{s \geq s_{\Sigma^0 p}} \begin{pmatrix} G_{\Lambda\Lambda} & 0 & 0 \\ 0 & G_{\Sigma^+} & 0 \\ 0 & 0 & G_{\Sigma^0} \end{pmatrix} \quad (4.24)$$

As long as only two channels are involved, we can solve the R -matrix equation and calculate the phase shifts, cross sections, and low energy parameters as before. For the part, where three channels are allowed, we approximate their coupling by two channel coupling. Thus, we introduce three subsystems:

$\Lambda p \leftrightarrow \Sigma^+ n$ Coupling

The first subsystem includes the $\Lambda p \leftrightarrow \Sigma^+ n$ coupling and gives a correct treatment of the $Q = 1$ channel for total energies below 2130.82 MeV. The R -matrix equation in operator notation reads:

$$\begin{pmatrix} R_{\Lambda\Lambda} & R_{\Lambda\Sigma^+} \\ R_{\Sigma^+\Lambda} & R_{\Sigma^+\Sigma^+} \end{pmatrix} = \begin{pmatrix} V_{\Lambda\Lambda} & V_{\Lambda\Sigma^+} \\ V_{\Sigma^+\Lambda} & V_{\Sigma^+\Sigma^+} \end{pmatrix} + \begin{pmatrix} V_{\Lambda\Lambda} & V_{\Lambda\Sigma^+} \\ V_{\Sigma^+\Lambda} & V_{\Sigma^+\Sigma^+} \end{pmatrix} \begin{pmatrix} G_{\Lambda} & 0 \\ 0 & G_{\Sigma^+} \end{pmatrix} \begin{pmatrix} R_{\Lambda\Lambda} & R_{\Lambda\Sigma^+} \\ R_{\Sigma^+\Lambda} & R_{\Sigma^+\Sigma^+} \end{pmatrix} \quad (4.25)$$

The cross sections of the $\Lambda p \leftrightarrow \Sigma^+ n$ channels are shown in fig. 4.14. The $\Lambda p \rightarrow \Lambda p$ cross section is greater than the experimental values for small momenta and lower for large momenta. Overall, the structure and thus the reason of the error seems to be the same as for the $\Sigma^+ p$ interaction. In the data base of [1] one data point for $\Lambda p \rightarrow \Sigma^+ n$ scattering can be found: the cross section is measured to be 30 ± 20 mb in an energy range of 240 ± 17 MeV [9]. Hence, the $\Lambda p \rightarrow \Sigma^+ n$ cross section seems to be too small by a factor 10^3 at least.

The LE parameter for $\Lambda p \leftrightarrow \Sigma^+ n$ scattering are given in tab. 4.10. The absolute value of the Λp scattering length is slightly smaller than the number found for the ΛN scattering and consistent with the Nijmegen models NSC97a-f [24]. These predict $-2.51 \text{ fm} \leq a_s \leq -0.71 \text{ fm}$ for Λp scattering. The effective range is of the same size as for ΛN scattering, as well.

Channel	a [fm]	r [fm]
Λp	-2.4021	2.5287
$\Sigma^+ n$ eigen	-8.7759	0.5615

Table 4.10.: (Eigen) low energy parameters for $\Lambda p \leftrightarrow \Sigma^+ n$.

The absolute value of the $\Sigma^+ n$ eigen-scattering length is higher than the $\Sigma N^{\frac{3}{2}}$ scattering lengths by a factor of almost 2. But one has to keep in mind that the eigen-LE parameter are not completely comparable to the LE parameters obtained from physical phase shifts.

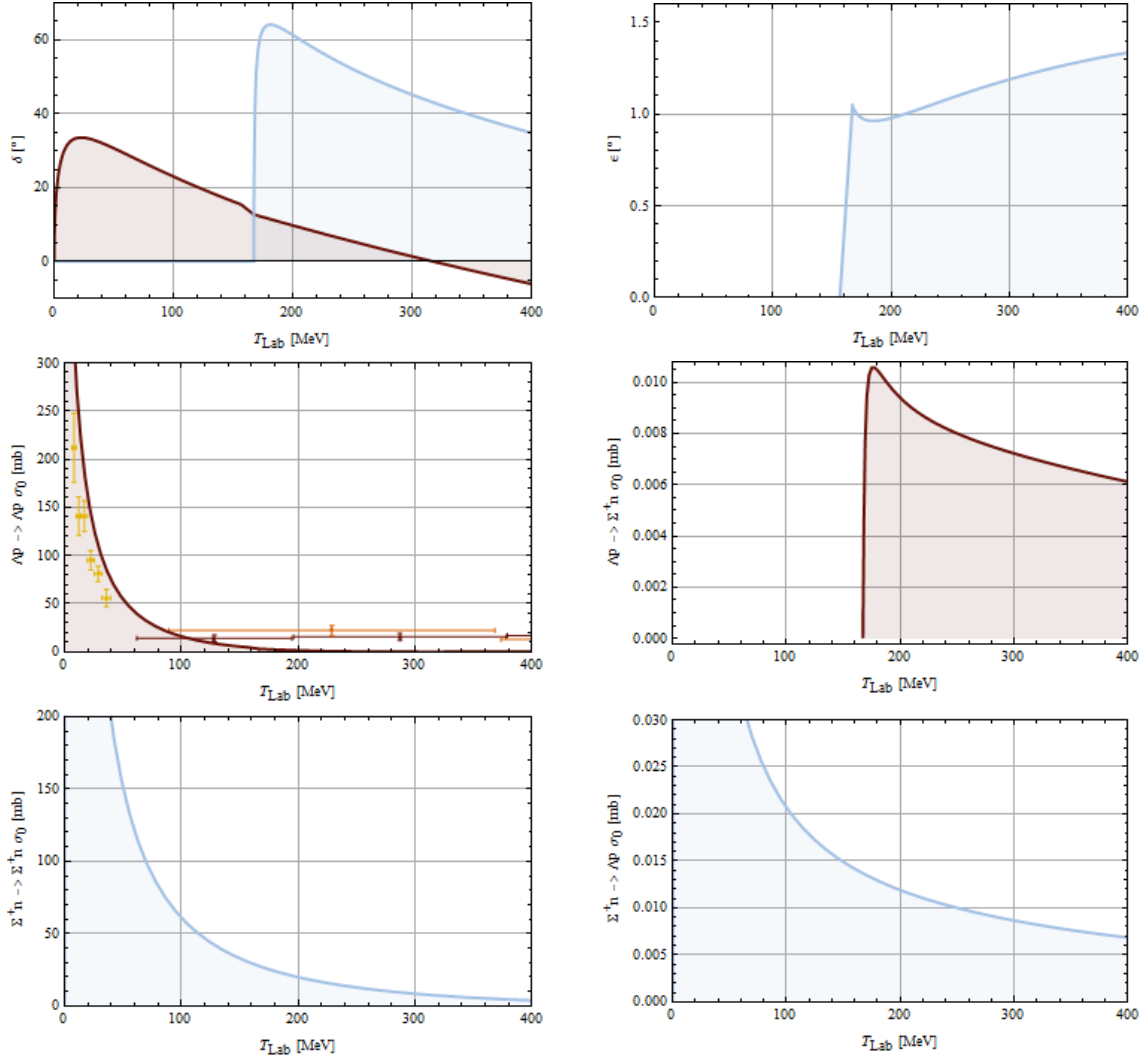


Figure 4.14.: $\Lambda p \leftrightarrow \Sigma^+ n$ SE-eigenphase shifts, mixing parameter, and cross sections. Data taken from [1], brown: CL67 [8], orange: CH70 [7], yellow: AL68 [3].

$\Lambda p \leftrightarrow \Sigma^0 p$ Coupling

The second subsystem includes the $\Lambda p \leftrightarrow \Sigma^0 p$ coupling. The R -matrix equation in operator notation for this subsystem reads:

$$\begin{pmatrix} R_{\Lambda\Lambda} & R_{\Lambda\Sigma^0} \\ R_{\Sigma^0\Lambda} & R_{\Sigma^0\Sigma^0} \end{pmatrix} = \begin{pmatrix} V_{\Lambda\Lambda} & V_{\Lambda\Sigma^0} \\ V_{\Sigma^0\Lambda} & V_{\Sigma^0\Sigma^0} \end{pmatrix} + \begin{pmatrix} V_{\Lambda\Lambda} & V_{\Lambda\Sigma^0} \\ V_{\Sigma^0\Lambda} & V_{\Sigma^0\Sigma^0} \end{pmatrix} \begin{pmatrix} G_{\Lambda} & 0 \\ 0 & G_{\Sigma^0} \end{pmatrix} \begin{pmatrix} R_{\Lambda\Lambda} & R_{\Lambda\Sigma^0} \\ R_{\Sigma^0\Lambda} & R_{\Sigma^0\Sigma^0} \end{pmatrix} \quad (4.26)$$

The phase shifts shown in fig. 4.15 have a similar structure as in the $\Lambda p \leftrightarrow \Sigma^+ n$ case, but the mixing parameter is negative, here. Additionally, the mixing is starting less strongly. For the $\Lambda p \rightarrow \Lambda p$ cross section we find a similar picture as before. Again, the experimental values found in [1] are much larger than our results for the transition cross section $\Lambda p \rightarrow \Sigma^0 p$. All these points can be explained by the obviously very small coupling between ΣN and ΛN channels. The structure of the $\Sigma^0 p \rightarrow \Sigma^0 p$ cross section is similar to the other cross sections discussed before, but the $\Sigma^0 p \rightarrow \Lambda p$ cross section is increasing slowly, in contrast.

The LE parameters are given in tab. 4.11. For the Λp the results are identical to the $\Lambda p \leftrightarrow \Sigma^+ n$ LE parameters, of course. The $\Sigma^0 p$ eigen-LE parameters have similar values.

Channel	a [fm]	r [fm]
Λp	-2.4021	2.5287
$\Sigma^0 p$ eigen	-2.0214	2.4805

Table 4.11.: (Eigen-) LE parameters for $\Lambda p \leftrightarrow \Sigma^0 p$.

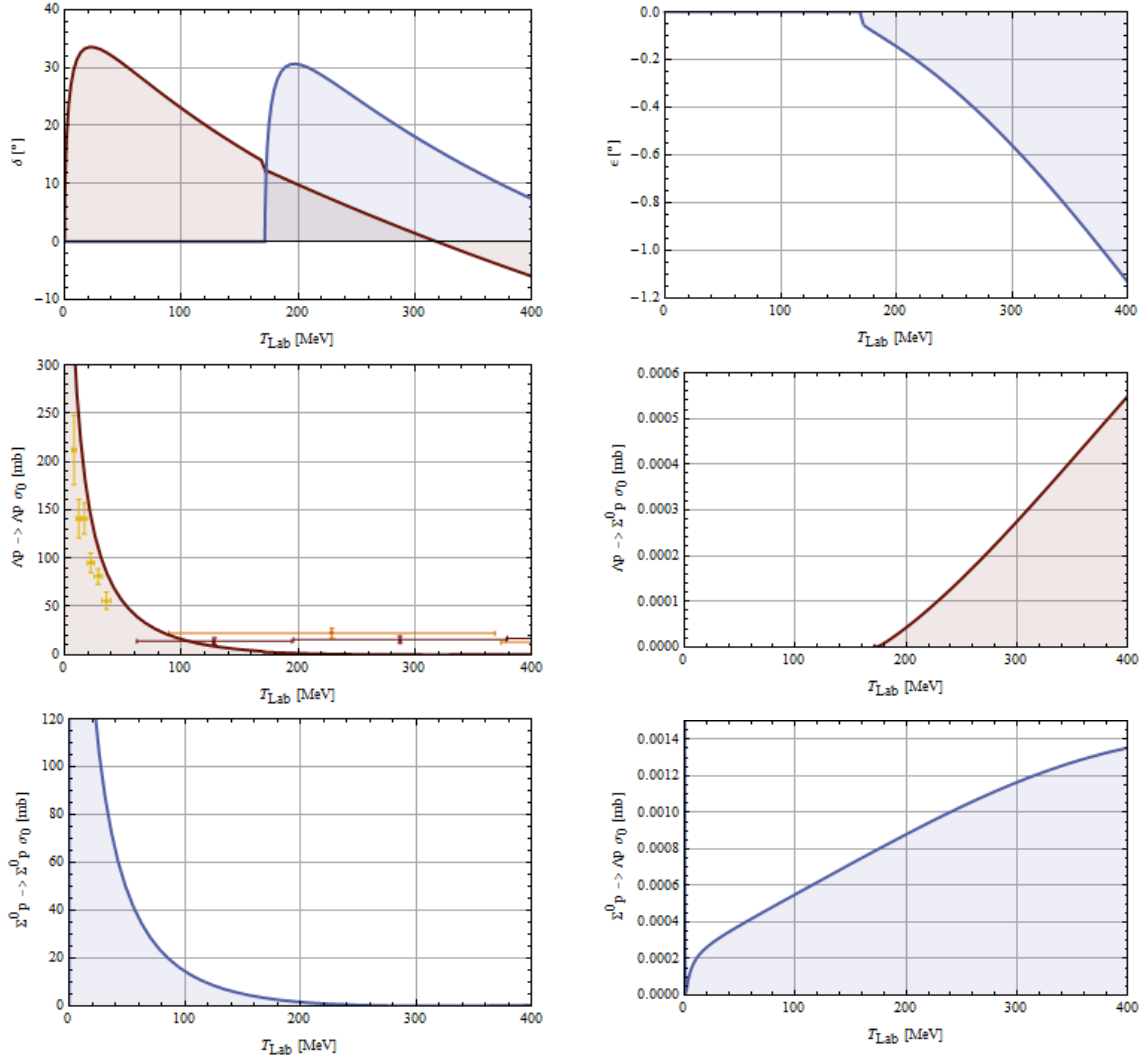


Figure 4.15.: $\Lambda p \leftrightarrow \Sigma^0 p$ SE-eigenphase shifts, mixing parameter, and cross sections. Data taken from [1], brown: CL67 [8], orange: CH70 [7], yellow: AL68 [3].

$\Sigma^+n \leftrightarrow \Sigma^0p$ Coupling

The third, and last, subsystem of the $Q = 1$ channel includes the $\Sigma^+n \leftrightarrow \Sigma^0p$ coupling. The R -matrix equation in operator notation for this subsystem reads:

$$\begin{pmatrix} R_{\Sigma^+\Sigma^+} & R_{\Sigma^+\Sigma^0} \\ R_{\Sigma^0\Sigma^+} & R_{\Sigma^0\Sigma^0} \end{pmatrix} = \begin{pmatrix} V_{\Sigma^+\Sigma^+} & V_{\Sigma^+\Sigma^0} \\ V_{\Sigma^0\Sigma^+} & V_{\Sigma^0\Sigma^0} \end{pmatrix} + \begin{pmatrix} V_{\Sigma^+\Sigma^+} & V_{\Sigma^+\Sigma^0} \\ V_{\Sigma^0\Sigma^+} & V_{\Sigma^0\Sigma^0} \end{pmatrix} \begin{pmatrix} G_{\Sigma^+} & 0 \\ 0 & G_{\Sigma^0} \end{pmatrix} \begin{pmatrix} R_{\Sigma^+\Sigma^+} & R_{\Sigma^+\Sigma^0} \\ R_{\Sigma^0\Sigma^+} & R_{\Sigma^0\Sigma^0} \end{pmatrix} \quad (4.27)$$

The phase shifts of the $\Sigma^+n \leftrightarrow \Sigma^0p$ coupling are shown in fig. 4.16. Since the mixing parameter ϵ is large, both channels influence each other more than they do influence the Λp channel in the other subsystems. Accordingly, the $\Sigma^+n \rightarrow \Sigma^+n$ cross section shows a kink when the Σ^0p channel becomes available. Another effect of the large mixing is the fact that the transition cross sections between both channels are of the same order of magnitude as the cross sections for scattering in the same state as the initial.

The LE parameters of the Σ^+n channels are nearby the eigen-LE parameters calculated in the $\Lambda p \leftrightarrow \Sigma^+n$ system. The deviation is less than 5 % for r_s and less than 1 % for a_s . The Σ^0p eigen-LE parameters show a different behavior: The effective range is larger by far than in the $\Lambda p \leftrightarrow \Sigma^0p$ system. This could be caused by numerical errors in the fitting procedure.

Channel	a [fm]	r [fm]
Σ^+n	-8.7103	0.5846
Σ^0p eigen	-2.3954	6.4034

Table 4.12.: (Eigen-) LE parameters for $\Sigma^+n \leftrightarrow \Sigma^0p$.

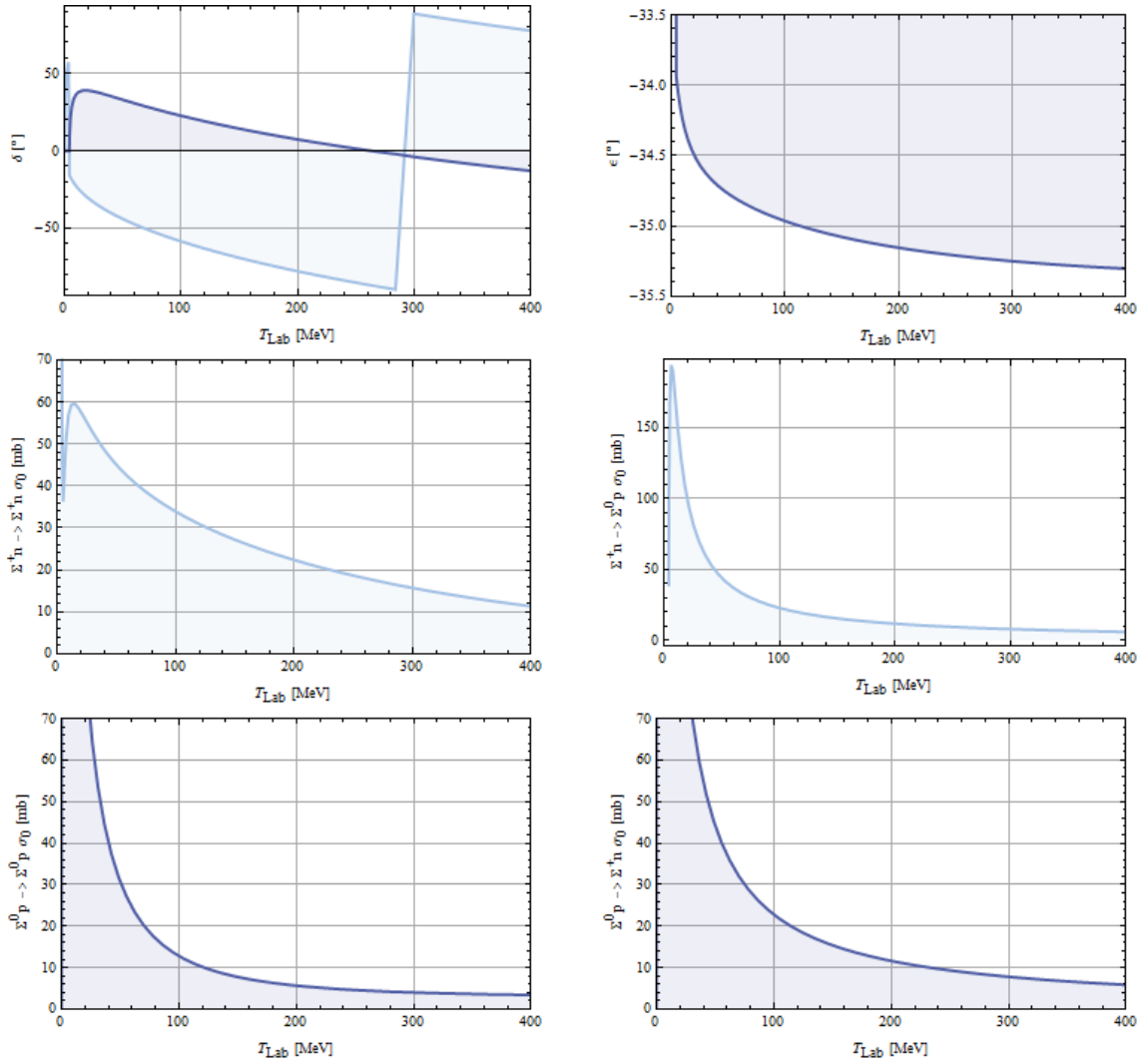


Figure 4.16.: $\Sigma^+n \leftrightarrow \Sigma^0p$ SE-eigenphase shifts, mixing parameter, and cross sections.

4.7.3. $Q = 0$ Channels

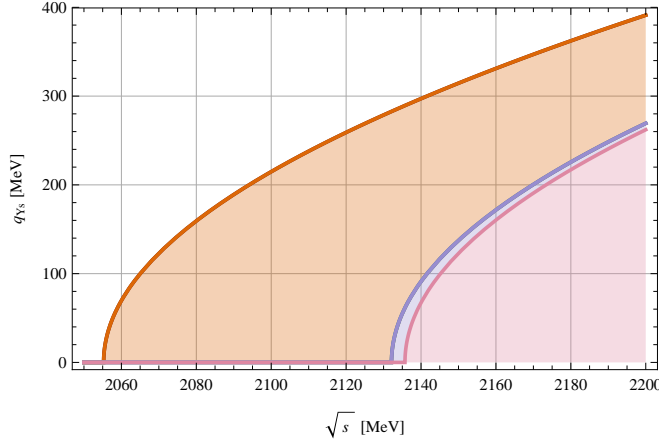


Figure 4.17.: Relation between mandelstam s and on shell momentum q_{Y_s} for $Q = 0$ channels. Legend as in 4.1.

The treatment of the $Q = 0$ channel can be executed analogous to that of the $Q = 1$ channel. The possible particle combinations are

$$\Lambda n, \Sigma^0 n, \text{ and } \Sigma^- p.$$

The corresponding thresholds and kinematics are shown in fig. 4.17.

Again, an isospin rotation is needed in order to achieve the potential in particle basis. According to [24], we use:

$$\begin{pmatrix} V_{\Lambda\Lambda} & V_{\Lambda\Sigma^0} & V_{\Lambda\Sigma^-} \\ V_{\Sigma^0\Lambda} & V_{\Sigma^0\Sigma^0} & V_{\Sigma^0\Sigma^-} \\ V_{\Sigma^-\Lambda} & V_{\Sigma^-\Sigma^0} & V_{\Sigma^-\Sigma^-} \end{pmatrix} = \begin{pmatrix} V_{\Lambda\Lambda} & \sqrt{\frac{1}{3}}V_{\Lambda\Sigma} & -\sqrt{\frac{2}{3}}V_{\Lambda\Sigma} \\ \sqrt{\frac{1}{3}}V_{\Sigma\Lambda} & \frac{1}{3}V_{\Sigma\Sigma}^{\frac{1}{2}} + \frac{2}{3}V_{\Sigma\Sigma}^{\frac{3}{2}} & \frac{\sqrt{2}}{3} \left[-V_{\Sigma\Sigma}^{\frac{1}{2}} + V_{\Sigma\Sigma}^{\frac{3}{2}} \right] \\ -\sqrt{\frac{2}{3}}V_{\Sigma\Lambda} & \frac{\sqrt{2}}{3} \left[-V_{\Sigma\Sigma}^{\frac{1}{2}} + V_{\Sigma\Sigma}^{\frac{3}{2}} \right] & \frac{2}{3}V_{\Sigma\Sigma}^{\frac{1}{2}} + \frac{1}{3}V_{\Sigma\Sigma}^{\frac{3}{2}} \end{pmatrix} \quad (4.28)$$

The successive opening of the channels leads to the structure

$$V_{\Lambda\Lambda} \xrightarrow{s \geq s_{\Sigma^0 n}} \begin{pmatrix} V_{\Lambda\Lambda} & V_{\Lambda\Sigma^0} \\ V_{\Sigma^0\Lambda} & V_{\Sigma^0\Sigma^0} \end{pmatrix} \xrightarrow{s \geq s_{\Sigma^- p}} \begin{pmatrix} V_{\Lambda\Lambda} & V_{\Lambda\Sigma^0} & V_{\Lambda\Sigma^-} \\ V_{\Sigma^0\Lambda} & V_{\Sigma^0\Sigma^0} & V_{\Sigma^0\Sigma^-} \\ V_{\Sigma^-\Lambda} & V_{\Sigma^-\Sigma^0} & V_{\Sigma^-\Sigma^-} \end{pmatrix} \quad (4.29)$$

$$R_{\Lambda\Lambda} \xrightarrow{s \geq s_{\Sigma^0 n}} \begin{pmatrix} R_{\Lambda\Lambda} & R_{\Lambda\Sigma^0} \\ R_{\Sigma^0\Lambda} & R_{\Sigma^0\Sigma^0} \end{pmatrix} \xrightarrow{s \geq s_{\Sigma^- p}} \begin{pmatrix} R_{\Lambda\Lambda} & R_{\Lambda\Sigma^0} & R_{\Lambda\Sigma^-} \\ R_{\Sigma^0\Lambda} & R_{\Sigma^0\Sigma^0} & R_{\Sigma^0\Sigma^-} \\ R_{\Sigma^-\Lambda} & R_{\Sigma^-\Sigma^0} & R_{\Sigma^-\Sigma^-} \end{pmatrix} \quad (4.30)$$

$$G_{\Lambda} \xrightarrow{s \geq s_{\Sigma^0 n}} \begin{pmatrix} G_{\Lambda} & 0 \\ 0 & G_{\Sigma^0} \end{pmatrix} \xrightarrow{s \geq s_{\Sigma^- p}} \begin{pmatrix} G_{\Lambda} & 0 & 0 \\ 0 & G_{\Sigma^0} & 0 \\ 0 & 0 & G_{\Sigma^-} \end{pmatrix}. \quad (4.31)$$

From here, the calculations are done in a completely similar way as for the $Q = 1$ channel. Thus, only the results of the calculations are discussed in this work.

$\Lambda n \leftrightarrow \Sigma^0 n$ Coupling

The overall structure of this subsystem is very similar to the of the $Q = 1$ $\Lambda p \leftrightarrow \Sigma^0 p$ subsystem. Results are shown in fig. 4.18 and tab. 4.13. The Nijmegen models NSC97a-f predict $-2.68 \text{ fm} \leq a_s \leq -0.76 \text{ fm}$ for the Λn channel [24], which coincides with our result.

Channel	a [fm]	r [fm]
Λn	-2.4053	2.4349
$\Sigma^0 n$ (eigen)	-2.0240	2.4762

Table 4.13.: (Eigen-) LE parameters for $\Lambda n \leftrightarrow \Sigma^0 n$.

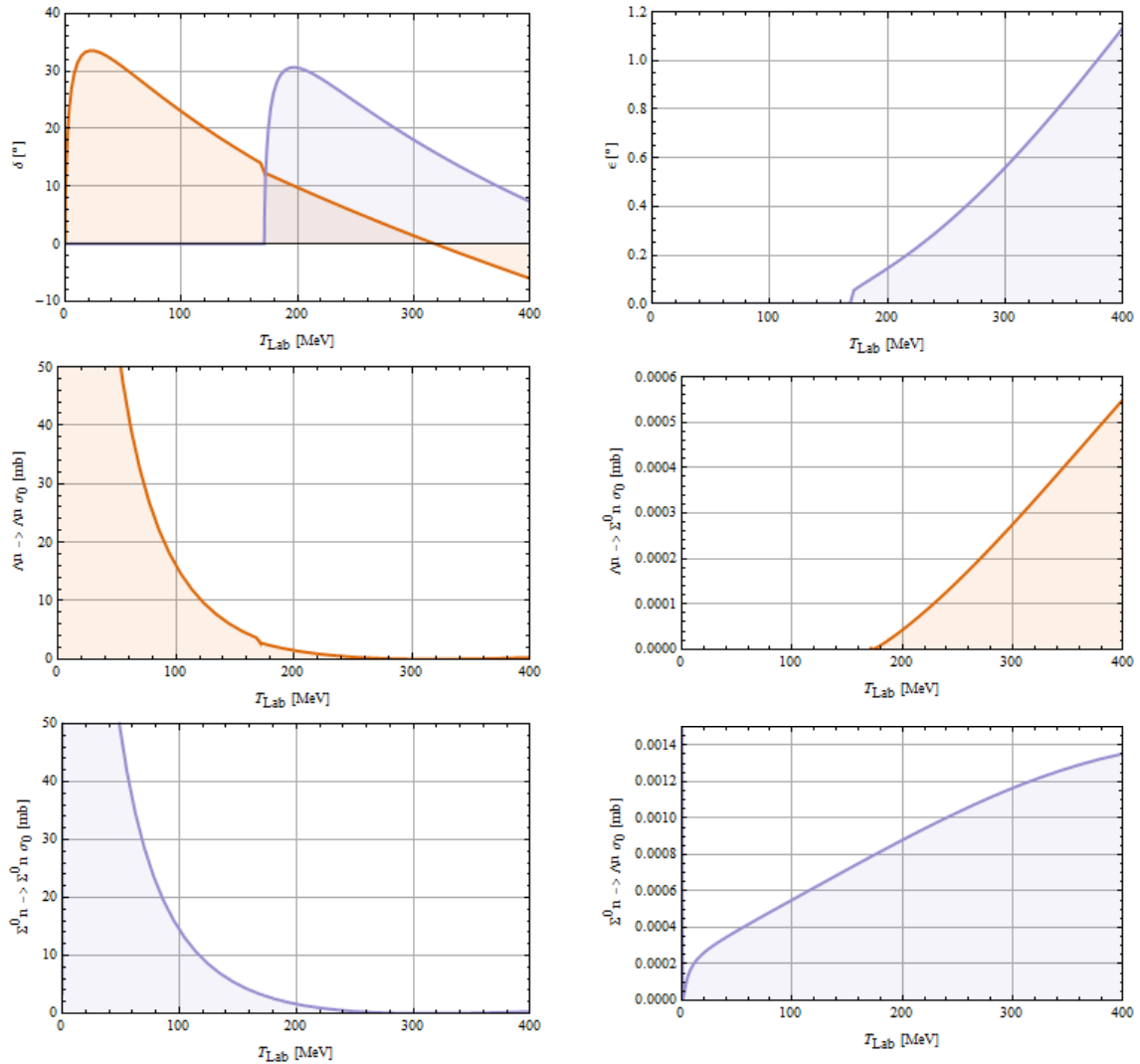


Figure 4.18.: $\Lambda n \leftrightarrow \Sigma^0 n$ SE-eigenphase shifts, mixing parameter, and cross sections.

$\Lambda n \leftrightarrow \Sigma^- p$ Coupling

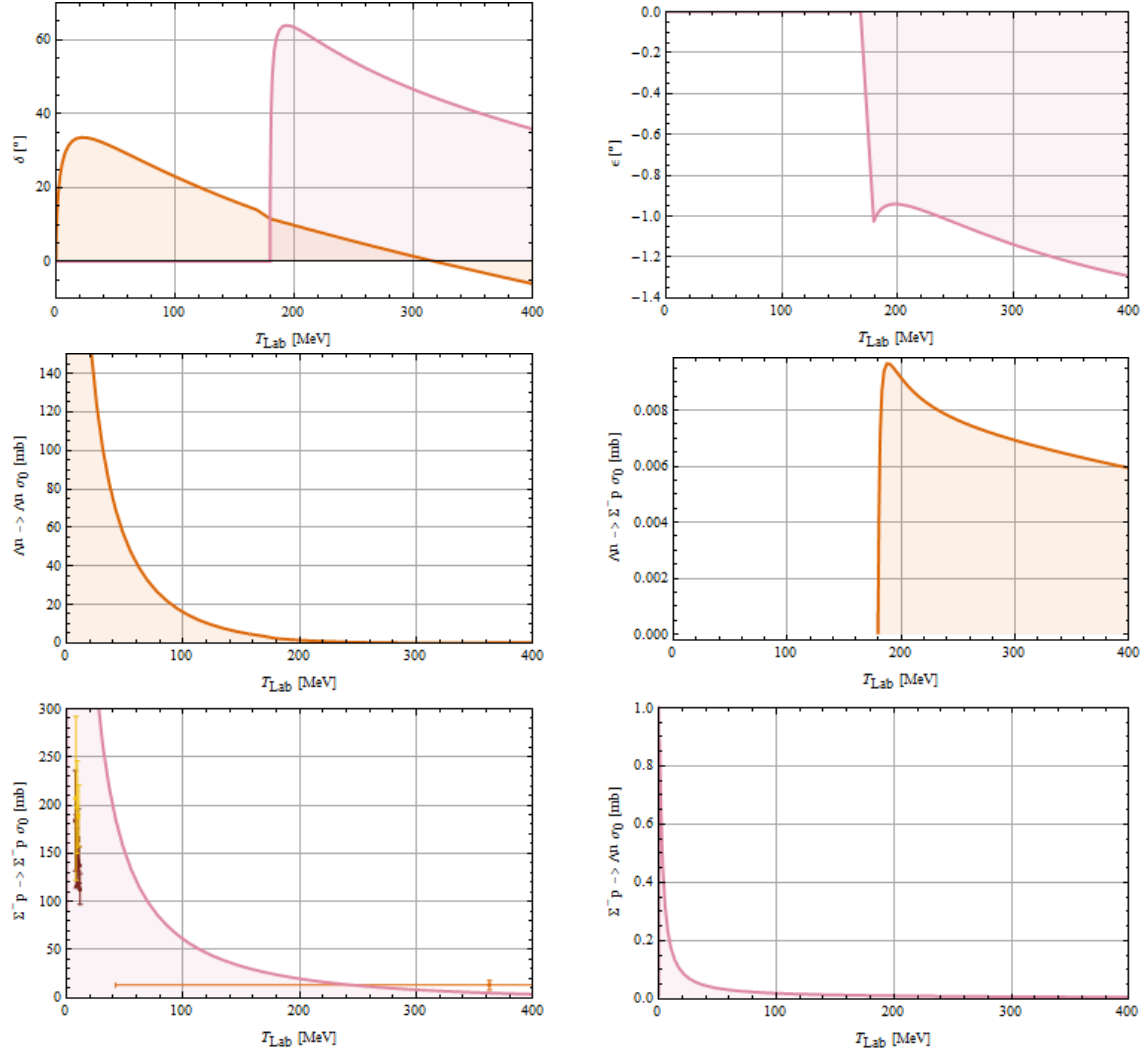


Figure 4.19.: $\Lambda n \leftrightarrow \Sigma^- p$ SE-eigenphase shifts, mixing parameter, and cross sections. Data taken from [1], brown: EI71 [12], orange: CH70 [7], yellow: DO66 [11].

The $\Lambda n \leftrightarrow \Sigma^- p$ results are shown in fig. 4.19. They resemble the $\Lambda p \rightarrow \Sigma^+ n$ results. Experimental values for the $\Sigma^- p \rightarrow \Lambda n$ cross section are much higher than the results of our calculation. Experimental measured cross sections are higher than 100 mb for momenta below 10 MeV [13]. Thus, our results are about a factor of 10^2 too low.

The $\Sigma^- p \rightarrow \Sigma^- p$ fits to the experimental data points as good as the other cross section for scattering in the same state as the initial state do.

The overall structure equates the structure of the $Q = 1$ $\Lambda p \leftrightarrow \Sigma^+ n$ subsystem even in terms of the LE parameters (shown in tab. 4.14).

Channel	a [fm]	r [fm]
Λn	-2.4053	2.4349
$\Sigma^- p$ (eigen)	-8.6470	0.6011

Table 4.14.: (Eigen-) LE parameters for $\Lambda n \leftrightarrow \Sigma^- p$.

$\Sigma^0 n \leftrightarrow \Sigma^- p$ Coupling

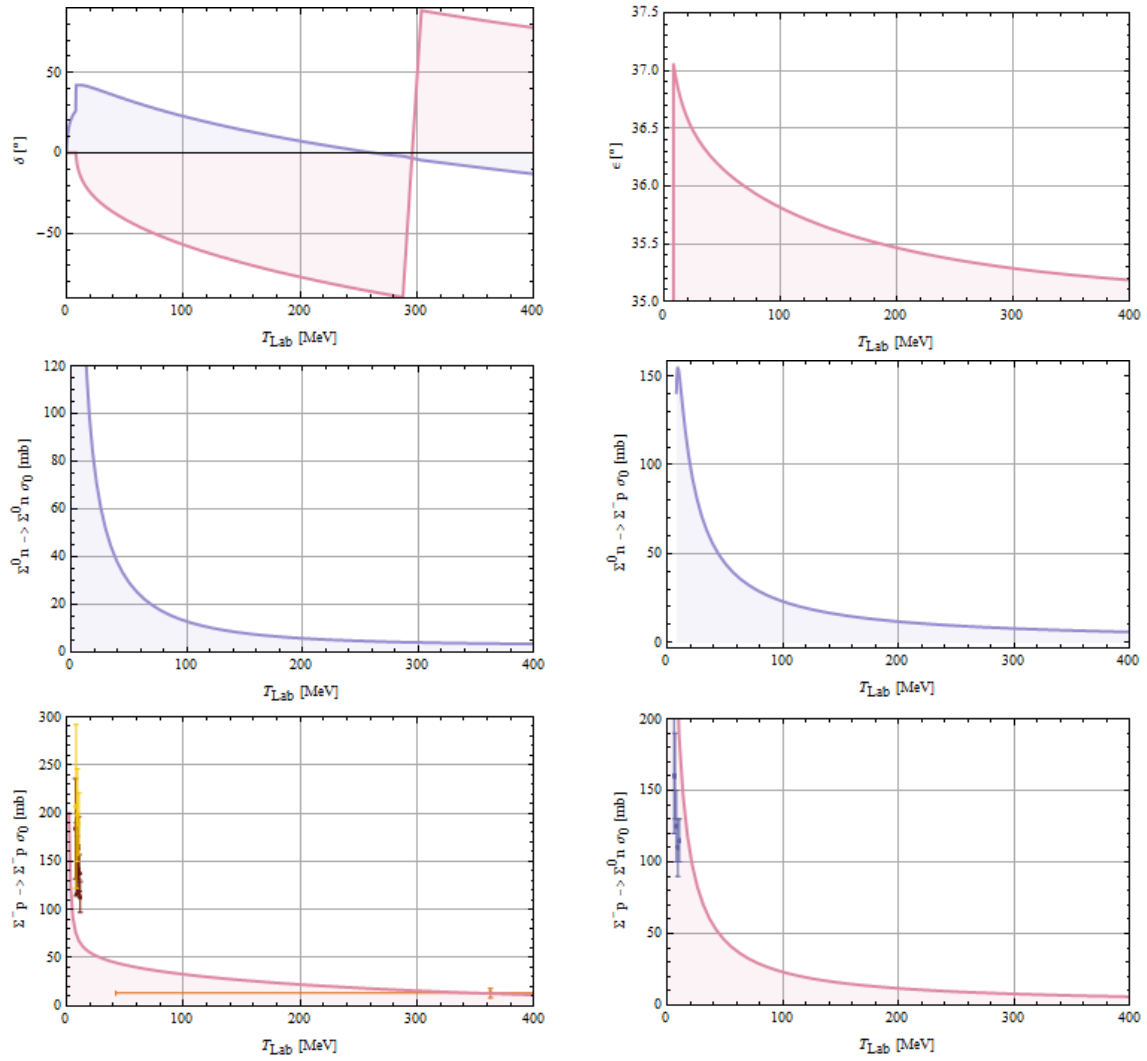


Figure 4.20.: $\Sigma^0 n \leftrightarrow \Sigma^- p$ SE-eigenphase shifts, mixing parameter, and cross sections. Data taken from [1], brown: EI71 [12], orange: CH70 [7], yellow: DO66 [11], blue: EN66 [13].

Here, the structure is very similar to the third subsystem of the $Q = 1$ channel. In comparison to the other channels, our results give a good description of the data points. The coupling of the Σ^-p state to the Σ^0n state seems to be slightly too strong, but the error is much smaller than for the coupling between ΣN and ΛN states.

The LE parameters of the Σ^0n channel (tab. 4.15) are changed by less than 3 % in comparison to the $\Lambda n \leftrightarrow \Sigma^0n$ system. The results for the Σ^-p eigen LE parameters seem to be influenced by numerical inaccuracy.

Channel	a [fm]	r [fm]
Σ^0n	-2.0243	2.5022
Σ^-p eigen	-0.2579	121.1809

Table 4.15.: (Eigen-) LE parameters for $\Sigma^0n \leftrightarrow \Sigma^-p$.

4.7.4. Quality of the Potential

Summarized, the YN potential derived from a NN potential seems to give possibility to describe the YN data, but needs further improvements. The inclusion of higher partial waves and scattering in triplet states could help to find a better description of the data. Another possible improvement could be achieved by fitting to cross section instead of fitting to theoretical predictions. Additionally, more fitting parameters could improve the YN potential, e.g. using the ansatz of eq. 4.1.

5. In-Medium Interaction

After constructing a YN potential and discussing its quality, we now want to describe in-medium scattering. In the first part of this chapter, the Pauli exclusion principle is introduced. Afterwards, the Pauli projection operator for two particles of different kinds is derived and results for scattering in symmetric nuclear matter are given.

5.1. Pauli Exclusion Principle in the R -matrix Equation

According to the Pauli exclusion principle, two identical fermions are not allowed to occupy the same quantum state, or in other words, the total wave function of two identical particles has to be antisymmetric under particle exchange.

The Pauli exclusion principle can be used to describe in-medium effects in scattering processes. This is done in terms of the Pauli projection operator, which prevents the scattering in quantum states that are forbidden by the Pauli exclusion principle.

In quantum mechanical systems, e.g. an atom, the quantum states are filled beginning at those with the lowest energy. The energy of the highest occupied quantum state is called Fermi energy [10]:

$$E_{Fi} = \frac{\hbar^2}{2m} k_{Fi}^2 \quad (5.1)$$

The Fermi momentum k_{Fi} is related to the density ρ_i of particle type i through

$$\rho_i(k_{Fi}) = \frac{k_{Fi}^3}{3\pi^2} \Leftrightarrow k_{Fi}(\rho_i) = \sqrt[3]{3\pi^2 \rho_i}. \quad (5.2)$$

Scattering in states with laboratory momenta below the Fermi momentum are prohibited because all those states are already occupied.

We want to describe interaction in nuclear matter and therefore are interested in calculating scattering especially at nuclear density (i.e. $\rho_0 = 0.16 \text{ fm}^{-3}$) and half nuclear density. If we assume symmetric nuclear matter, the numbers of protons and neutrons per volume are identical and $\rho_{p0} = \rho_{n0} = \frac{\rho_0}{2} = 0.08$.

ρ_i [fm^{-3}]	k_{Fi} [MeV]
0.04	208.778
0.08	263.043
0.16	331.414
0.32	417.555
0.64	526.086

Table 5.1.: Fermi-momenta for some density values.

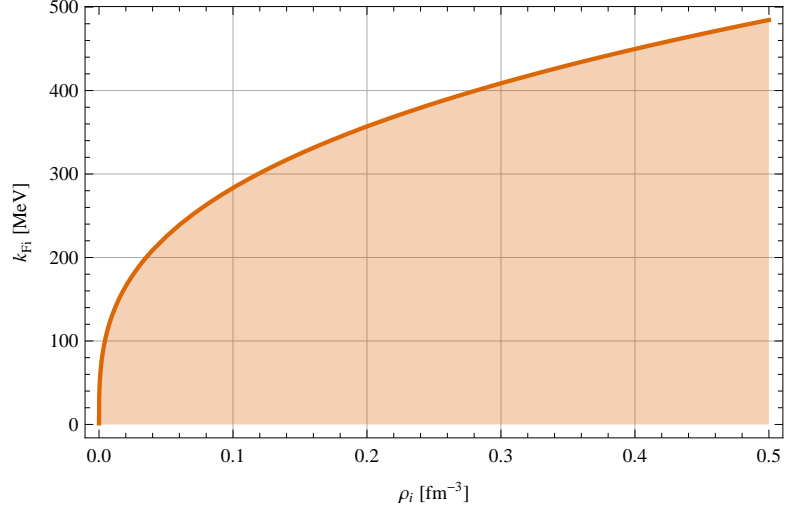


Figure 5.1.: Fermi-momentum k_{Fi} as function of density ρ_i .

The in-medium effects can be included in the R -matrix equation by multiplying the Pauli projection operator $Q(k, P)$ with every Green's function [15]. The resulting equation is called Bethe-Goldstone (BS) equation and reads for uncoupled channels:

$$R^J(q', q) = {}^0V^J(q', q) + \mathbf{P} \int dk V^J(q', k) G(k, P) Q(k, P) R^J(k, q) \quad (5.3)$$

Since the major part of the in-medium effects are produced by the Pauli projection operator, we solve this equation without taking into account the baryonic self-energies evolving in the medium. As a highly appreciated side effect this approximation also leads to considerable numerical simplifications.

5.2. Pauli Projection Operator

The Pauli projection operator for one particle is defined as $Q = \Theta(k^2 - k_F^2)$. For a system of two particles with momenta $k_{1,2}$ in laboratory frame and Fermi-momenta $k_{F1,2}$ it can be written as [17]:

$$Q_F = \Theta(k_1^2 - k_{F1}^2) \Theta(k_2^2 - k_{F2}^2) \quad (5.4)$$

5.2.1. Transformation to c.m. Frame

The R -matrix equation is solved in c.m. frame, henceforth we have to write the Pauli projection operator in c.m. frame. The relation between laboratory and c.m. frame

parameters are

$$\vec{k}_1 = \vec{q} + x_2 \vec{P} \quad (5.5)$$

$$\vec{k}_2 = -\vec{q} + x_1 \vec{P}. \quad (5.6)$$

Where \vec{P} is the conserved c.m. momentum and \vec{q} the relative momentum:

$$\vec{P} = \vec{k}_1 + \vec{k}_2 = \vec{k}_1' + \vec{k}_2' \quad (5.7)$$

$$\vec{q} = x_1 \vec{k}_1 - x_2 \vec{k}_2 \quad (5.8)$$

The c.m. momentum is given by the momentum of the projectile in laboratory system p_{Lab} (eq. 2.4). Inserting eq. 5.5 and eq. 5.6 in eq. 5.8 one finds $x_1 + x_2 = 1$. the Lorentz-invariant choice for the weights is [17]:

$$x_1 = \frac{1}{2} \left(\frac{m_2^2 - m_1^2}{s} + 1 \right) \quad \text{and} \quad x_2 = \frac{1}{2} \left(\frac{m_1^2 - m_2^2}{s} + 1 \right) \quad (5.9)$$

Here s denotes the total energy squared and E_i the particle energy, which in the c.m. frame are given by:

$$s = (E_1(\vec{q}) + E_2(\vec{q}))^2 \quad (5.10)$$

$$E_i(\vec{q}) = \sqrt{m_i^2 + q^2} \quad (5.11)$$

For identical particles the weights are $\frac{1}{2}$. If the particles have different masses, the weights will have the largest difference for $q = 0$ and are approaching $\frac{1}{2}$ as q grows bigger. This is shown in fig. 5.2 for the $\Sigma^+ p$ channel. It will be taken as an example in the following description of this section.

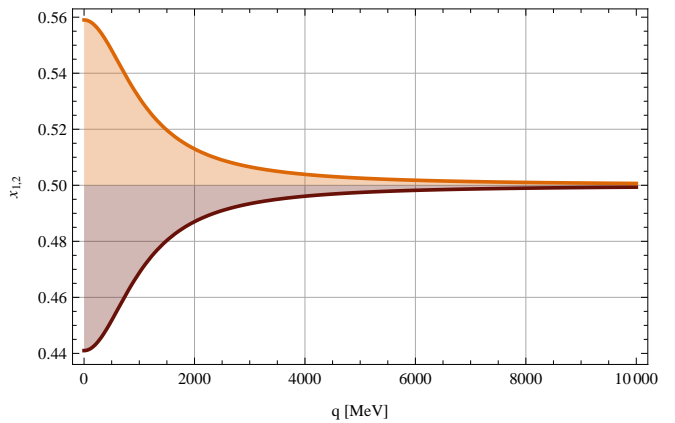


Figure 5.2.: x_1 (brown) and x_2 (orange) for $\Sigma^+ p$ scattering. $m_1 = m_{\Sigma^+}$, $m_2 = m_p$.

Inserting eq. 5.5 and eq. 5.6 into eq. 5.4 gives

$$\begin{aligned} Q_F &= \Theta(q^2 + x_2^2 P^2 - k_{F1}^2 + 2x_2 q P \cos \vartheta) \Theta(q^2 + x_1^2 P^2 - k_{F2}^2 - 2x_1 q P \cos \vartheta) \\ &= \Theta(Z_1 + \cos \vartheta) \Theta(Z_2 - \cos \vartheta) \end{aligned} \quad (5.12)$$

with

$$Z_1 = \frac{q^2 + x_2^2 P^2 - k_{F1}^2}{2x_2 P q} \quad \text{and} \quad Z_2 = \frac{q^2 + x_1^2 P^2 - k_{F2}^2}{2x_1 P q}. \quad (5.13)$$

These quantities can only be negative if the Fermi momenta are both positive and big enough (as shown in fig. 5.3).

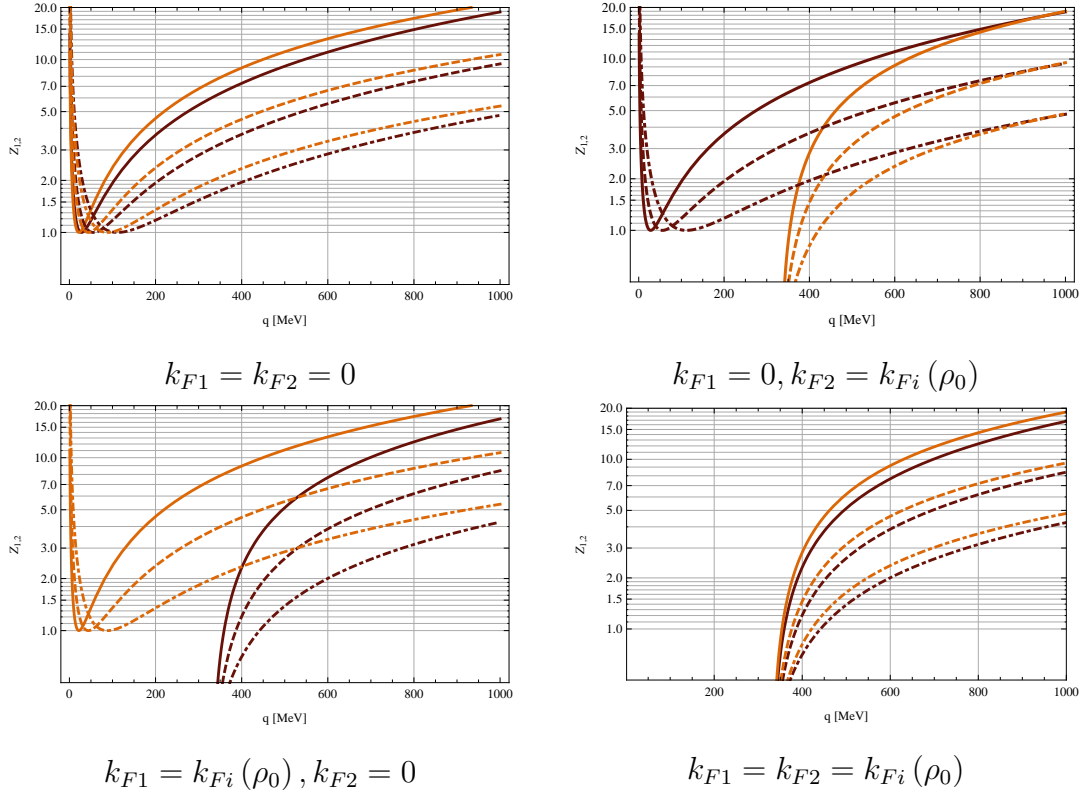


Figure 5.3.: Z_1 (brown) and Z_2 (orange) as function of q for $\Sigma^+ p$ scattering ($m_1 = m_{\Sigma^+}$, $m_2 = m_p$). Solid lines $P = 50$ MeV, dashed $P = 100$ MeV, dashed-dotted $P = 200$ MeV.

We follow the common practice [23] and use the angle-averaged Pauli projection operator. For this purpose we integrate the Pauli projection operator over the unit sphere and find

the angle averaged Pauli projection operator \overline{Q}_F :

$$\begin{aligned}
 \overline{Q}_F &= \frac{1}{4\pi} \int Q_F d\Omega \\
 &= \frac{1}{2} \int_{-1}^1 Q_F d \cos \vartheta \\
 &= \frac{1}{2} \Theta(Z_1 + Z_2) \Theta(1 + Z_1) \Theta(1 + Z_2) \\
 &\quad [2\Theta(-1 + Z_1) \Theta(-1 + Z_2) + (1 + Z_2) \Theta(-1 + Z_1) \Theta(1 - Z_2) \\
 &\quad + (Z_1 + Z_2) \Theta(1 - Z_1) + (1 - Z_2) \Theta(1 - Z_1) \Theta(-1 + Z_2)] \quad (5.14) \\
 &= Q(k, P)
 \end{aligned}$$

The shape of \overline{Q}_F plotted as function of Z_1 and Z_2 is simple, as can be seen in fig. 5.4. Basically it consists of four planes.

Plotting $Q(k, P)$ as a function of q for fixed values of m_i , k_{Fi} and P gives a slightly more complicated picture as shown in fig. 5.5. It can be seen that $Q(k, P)$ no longer is linear and has kinks at some points. To better understand this behavior of $Q(k, P)$, the curves from fig. 5.5 are plotted in comparison to \overline{Q}_F in 5.4. The curves are bend and cross several planes of the Pauli projection operator in Z_1 - Z_2 space. Additionally, the Z_i are not linear in q . Altogether this gives the shape shown in 5.5.

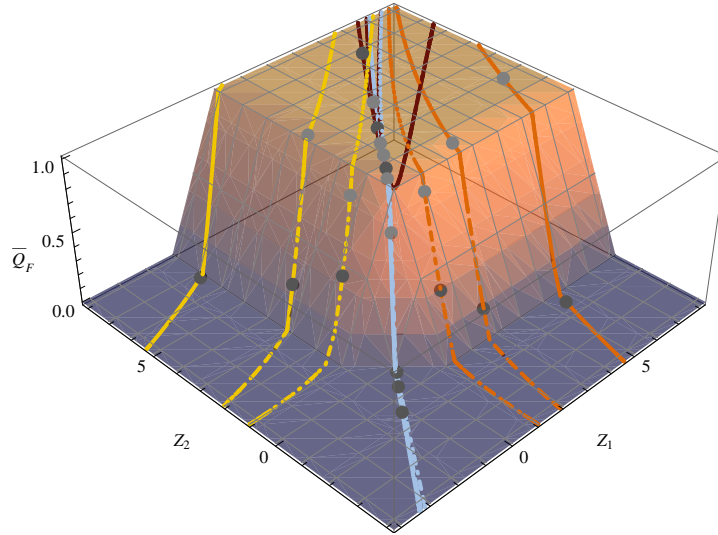


Figure 5.4.: \overline{Q}_F as function of Z_1 and Z_2 for Σ^+p scattering. Legend as in 5.5. Dark gray points mark values for $q = 300$ MeV, light gray points mark values for $q = 400$ MeV.

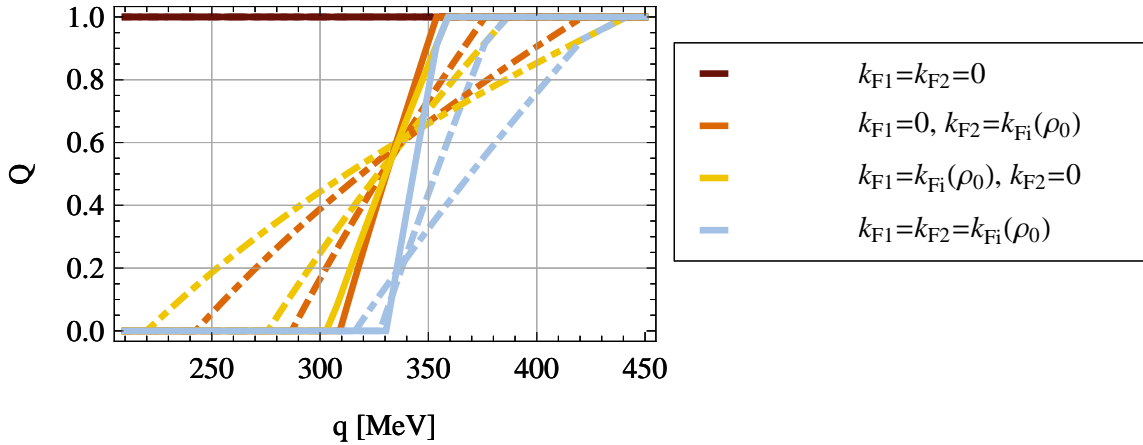


Figure 5.5.: $Q(k, P)$ as function of q for Σ^+p scattering. Solid lines $P = 50$ MeV, dashed $P = 100$ MeV, dashed-dotted $P = 200$ MeV.

5.3. Results

We will concentrate on scattering in symmetric nuclear matter, i.e. $k_{Fp} = k_{Fn}$ and set the Fermi momenta of all other particles equal zero. Even though the derived Pauli projection operator in the used definition is valid for arbitrary Fermi momenta of each particle, only the described case is subject matter of the actual study.

Since the results for the effective range r_s seemed to be influenced by numerical inaccuracies even for vacuum interaction, we will concentrate on discussing the results for the LE parameter a_s .

5.3.1. Uncoupled Channels

The impact of in-medium interaction on the phase shift and cross section of the uncoupled channels is shown in figs. 5.6 and 5.7. The results are nearly identical for both channels. The scattering in half nuclear density is influenced by in-medium effects almost as strongly as at nuclear density. This is due to the fact that not the density, but the Fermi momentum enters the Pauli projection operator and the Fermi momentum is proportional to the third root of the density. The phase shifts as well as the cross section of both channels are reduced by in-medium effects, especially at small momenta.

In fig. 5.8 the scattering length a_s for both channels is shown. Over all, the structures of the two channels are very similar. a_s is negative over the plotted range with decreasing absolute value.

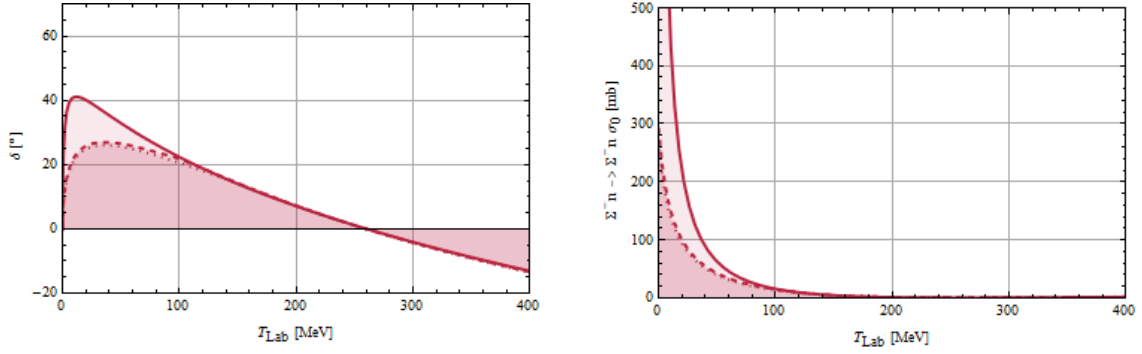


Figure 5.6.: Σ^-n phase shift and cross section. Solid line: vacuum interaction, dashed: $\rho_p = \rho_n = 0.04 \text{ fm}^{-3}$, dotted: $\rho_p = \rho_n = 0.08 \text{ fm}^{-3}$.

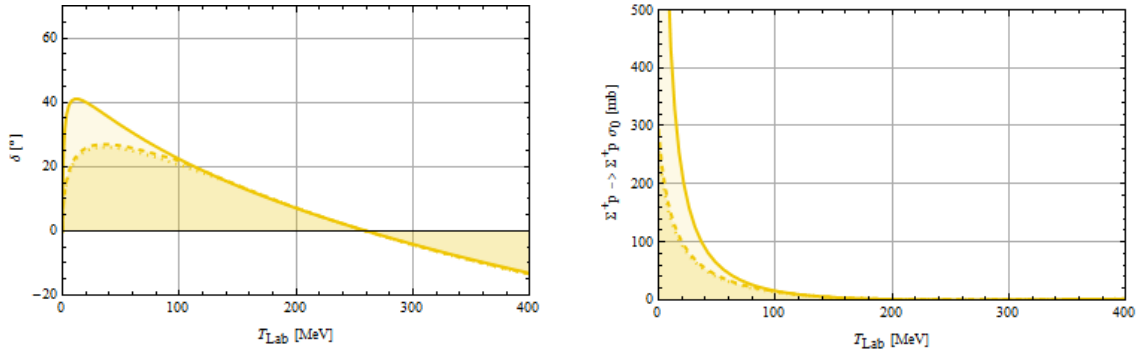


Figure 5.7.: Σ^+p phase shift and cross section. Solid line: vacuum interaction, dashed: $\rho_p = \rho_n = 0.04 \text{ fm}^{-3}$, dotted: $\rho_p = \rho_n = 0.08 \text{ fm}^{-3}$.

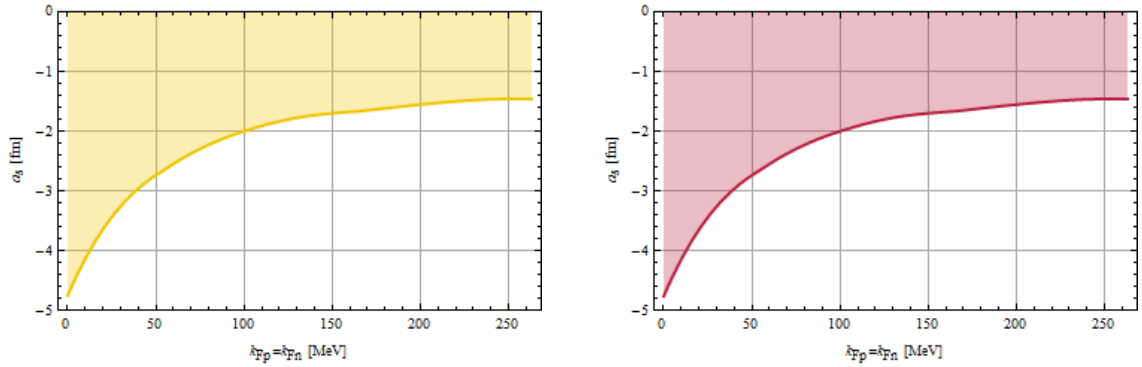


Figure 5.8.: a_s in dependency of Fermi momentum for the uncoupled channels. Yellow: Σ^+p , red: Σ^-n .

5.3.2. $Q = 1$ Channels

 $\Lambda p \leftrightarrow \Sigma^+ n$ Coupling

Like for the uncoupled channels, the in-medium effects lead to a decrease in phase shifts as well as in the cross sections. The kink in the $\Lambda p \rightarrow \Sigma^+ n$ cross section is suppressed in medium and the cross section is increasing slowly instead. This effect is observed in the $\Sigma^+ n \rightarrow \Lambda p$ cross section as well.

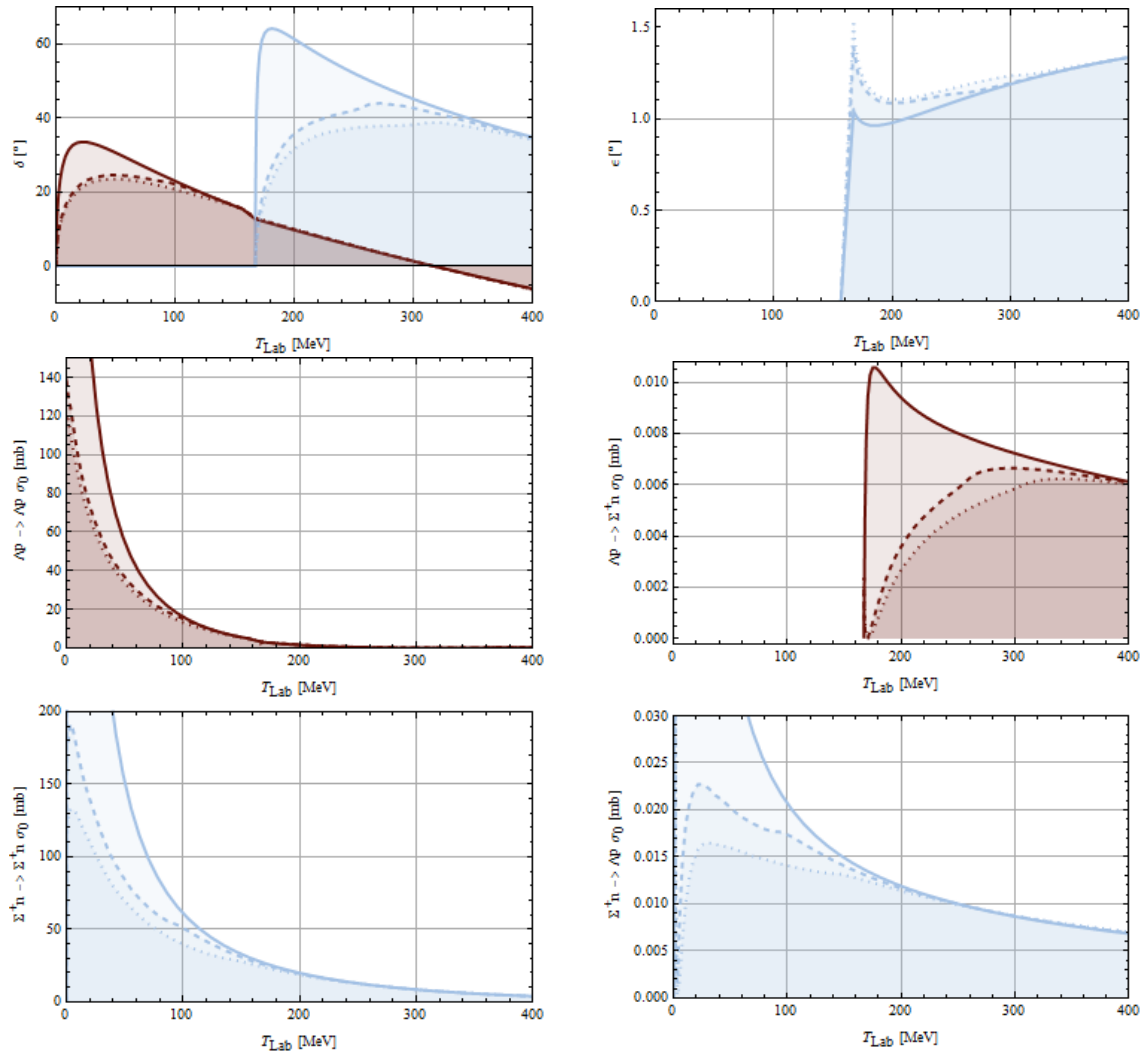


Figure 5.9.: $\Sigma^+ n$ SE-phase shifts, mixing parameter and cross sections. Solid line: vacuum interaction, dashed: $\rho_p = \rho_n = 0.04 \text{ fm}^{-3}$, dotted: $\rho_p = \rho_n = 0.08 \text{ fm}^{-3}$.

$\Lambda p \leftrightarrow \Sigma^0 p$ Coupling

In-medium effects in this subsystem result in an decrease of phase shifts and cross sections, as shown in fig. 5.10. The consequences of the in-medium calculations are very similar to the results found for the uncoupled channels.

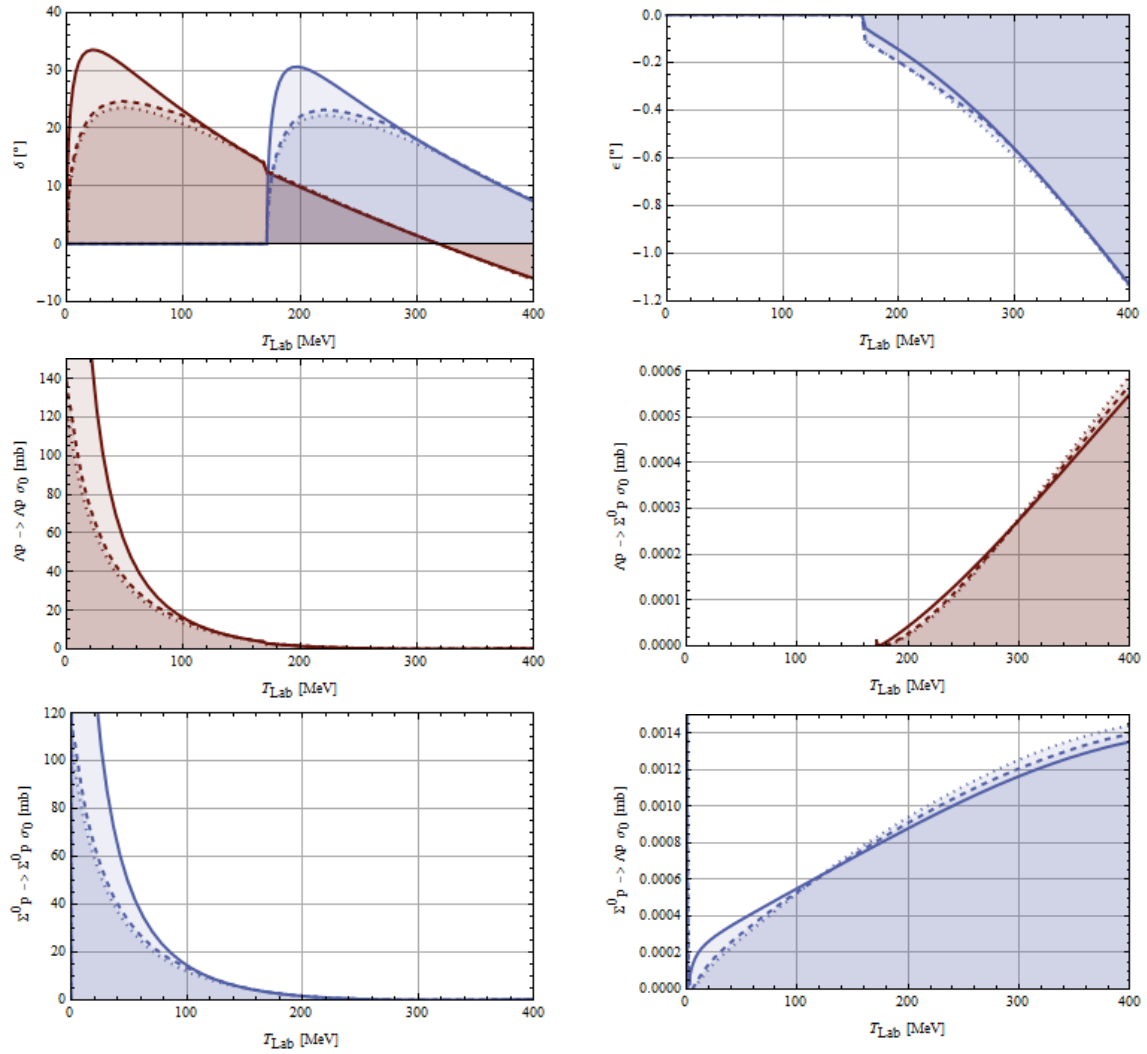


Figure 5.10.: $\Sigma^0 p$ SE-phase shifts, mixing parameter and cross sections. Solid line: vacuum interaction, dashed: $\rho_p = \rho_n = 0.04 \text{ fm}^{-3}$, dotted: $\rho_p = \rho_n = 0.08 \text{ fm}^{-3}$.

$\Sigma^+n \leftrightarrow \Sigma^0p$ Coupling

In the $\Sigma^+n \leftrightarrow \Sigma^0p$ system, the in-medium effects influence the structure in particular for the $\Sigma^+n \leftrightarrow \Sigma^+n$ cross section. Here the kink, which is caused by the opening of the Σ^0p channel in vacuum vanishes and the whole cross section increases for small energies. Another interesting point is that the mixing parameter is oscillating for small energies. This could be caused by numerical inaccuracies.

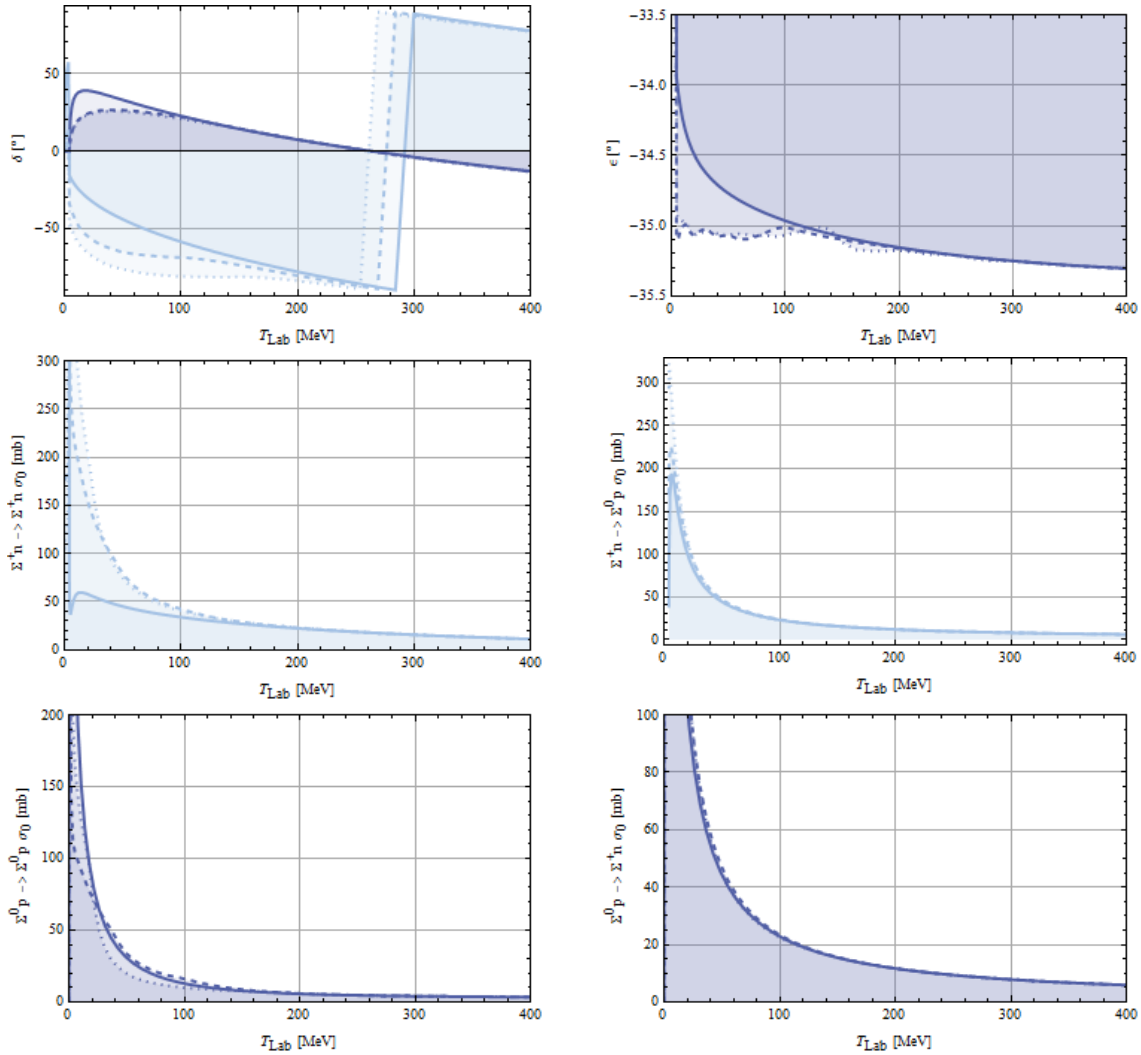


Figure 5.11.: Σ^0p SE-phase shifts, mixing parameter and cross sections. Solid line: vacuum interaction, dashed: $\rho_p = \rho_n = 0.04 \text{ fm}^{-3}$, dotted: $\rho_p = \rho_n = 0.08 \text{ fm}^{-3}$.

LE Parameter

The scattering length a_s is increasing with increasing Fermi momenta for all $Q = 1$ channels (fig. 5.12). The scattering length for Λp and Σ^+n are not as influenced by the chosen subsystem as the eigen-scattering length of the $\Sigma^0 p$. Additionally, in the $\Sigma^0 p$ scattering length calculated in the $\Sigma^+n \leftrightarrow \Sigma^0 p$ subsystem a change in the sign appears.

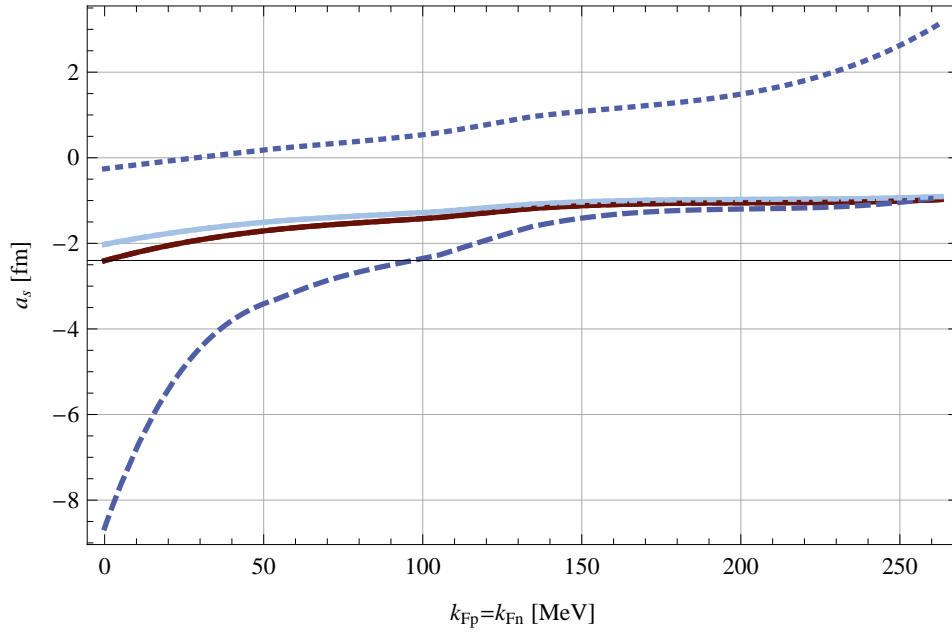


Figure 5.12.: a_s as function of Fermi momenta. Brown: Λp , light blue: Σ^+n , dark blue: $\Sigma^0 p$. Calculated in the subsystems as follows: Solid line: $\Lambda p \leftrightarrow \Sigma^+n$, dashed: $\Lambda p \leftrightarrow \Sigma^0 p$, dotted: $\Sigma^+n \leftrightarrow \Sigma^0 p$.

5.3.3. $Q = 0$ Channels

$\Lambda n \leftrightarrow \Sigma^0 n$ Coupling

The in-medium effect in the $\Lambda n \leftrightarrow \Sigma^0 n$ subsystem are similar to that of the $\Lambda p \leftrightarrow \Sigma^0 p$ subsystem. Hence, we do not need to discuss the results in more detail.

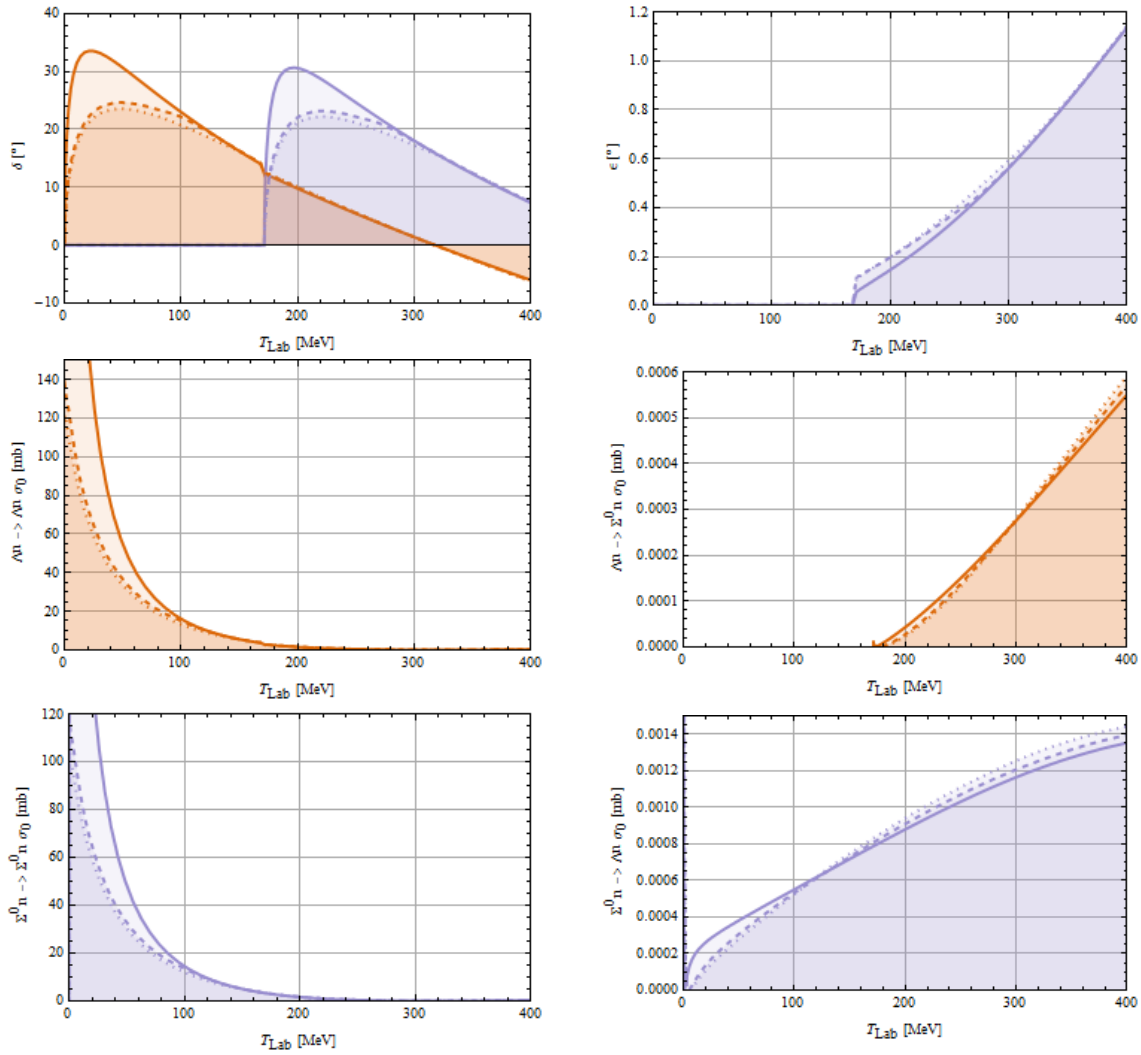


Figure 5.13.: $\Sigma^0 n$ SE-phase shifts, mixing parameter and cross sections. Solid line: vacuum interaction, dashed: $\rho_p = \rho_n = 0.04 \text{ fm}^{-3}$, dotted: $\rho_p = \rho_n = 0.08 \text{ fm}^{-3}$.

$\Lambda n \leftrightarrow \Sigma^- p$ Coupling

This subsystem is influenced more by in medium effects than the previous subsystem is. As discussed for the $\Lambda p \leftrightarrow \Sigma^+ n$ coupling, the kinks of the transition cross sections are suppressed.

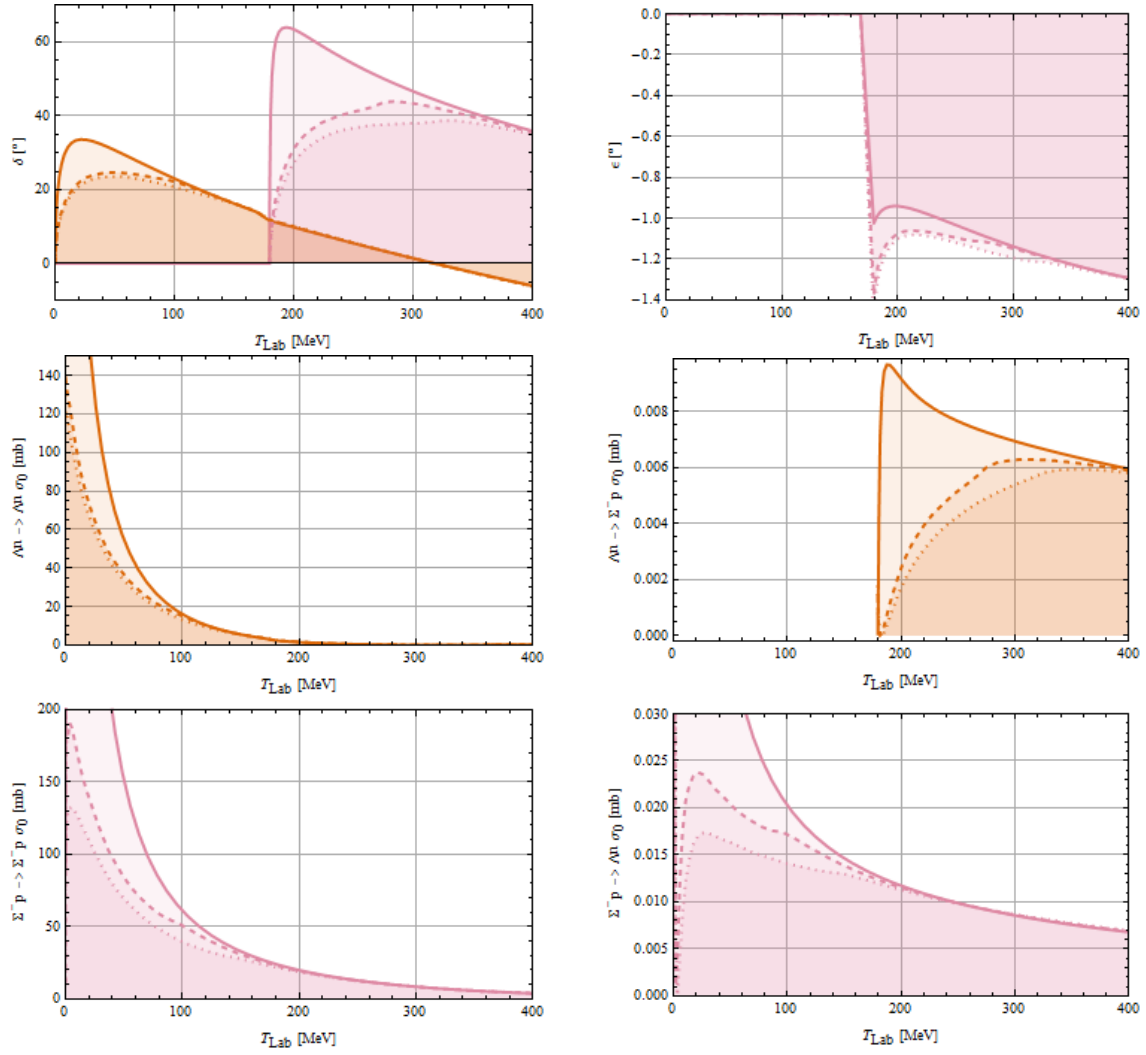


Figure 5.14.: $\Sigma^- p$ SE-phase shifts, mixing parameter and cross sections. Solid line: vacuum interaction, dashed: $\rho_p = \rho_n = 0.04 \text{ fm}^{-3}$, dotted: $\rho_p = \rho_n = 0.08 \text{ fm}^{-3}$.

$\Sigma^0 n \leftrightarrow \Sigma^- p$ Coupling

In this subsystem, an additional structure in the $\Sigma^0 n \leftrightarrow \Sigma^0 n$ cross section is found. The kink caused by the opening of the $\Sigma^- p$ channel becomes more visible with increasing density. As we found for the $\Sigma^+ n \leftrightarrow \Sigma^0 p$ channel, the mixing parameter oscillates for small energies.

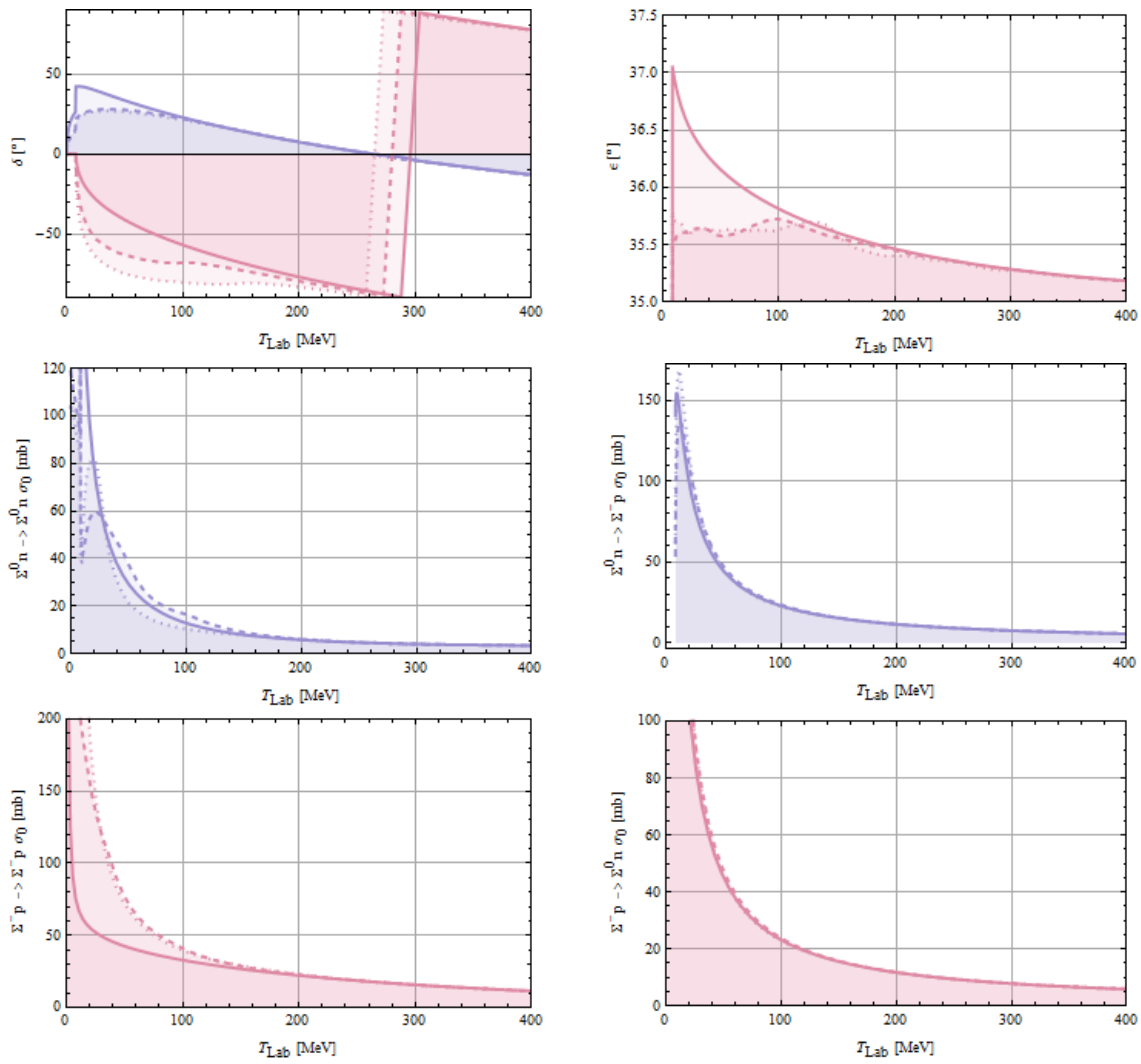


Figure 5.15.: $\Sigma^- p$ SE-phase shifts, mixing parameter and cross sections. Solid line: vacuum interaction, dashed: $\rho_p = \rho_n = 0.04 \text{ fm}^{-3}$, dotted: $\rho_p = \rho_n = 0.08 \text{ fm}^{-3}$.

LE Parameter

From the scattering length shown in fig. 5.16, only the Σ^-p eigen-scattering length shows a change in the sign. Besides, the subsystem in which the calculation has been carried out has the strongest input in this channel. All a_s are increasing with increasing Fermi momenta, as we found for the $Q = 1$ channels.

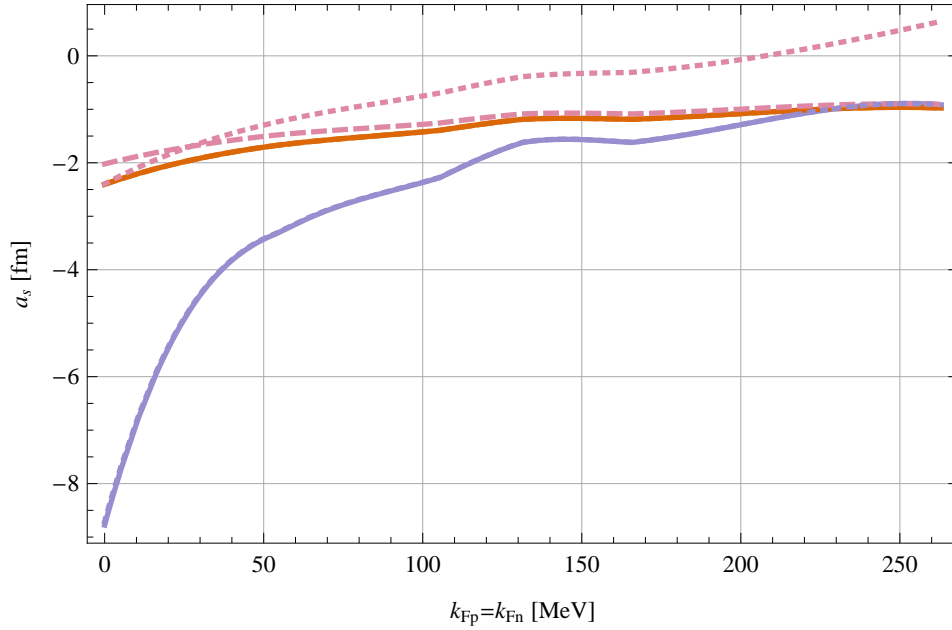


Figure 5.16.: a_s as function of fermi momenta. Orange: Λn , purple: $\Sigma^0 n$, pink: $\Sigma^- p$. Calculated in the subsystems as follows: Solid line: $\Lambda n \leftrightarrow \Sigma^0 n$, dashed: $\Lambda n \leftrightarrow \Sigma^- p$, dotted: $\Sigma^0 n \leftrightarrow \Sigma^- p$.

5.3.4. Summary

The uncoupled channels are influenced in terms of lower phase shifts, cross section and increasing scattering length. The results of the $\Lambda N \leftrightarrow \Sigma N$ channels where no charge transfer between hyperon and nucleon occurs, show a similar structure.

Looking at the transition cross sections of the coupled channels, we find the cross sections from a ΛN system into a ΣN system with charge transition between hyperon and nucleon to be influenced by in medium effects strongly. In nuclear matter the kinks in the $\Lambda p \rightarrow \Sigma^+ n$ cross section as well as the $\Lambda p \rightarrow \Sigma^+ n$ cross section are suppressed.

5. *In-Medium Interaction*

The subsystems treating $\Sigma N \leftrightarrow \Sigma N$ coupling, are influenced in a different way. In $\Sigma^+ n \rightarrow \Sigma^+ n$ the kink is suppressed with increasing density, in $\Sigma^0 n \leftrightarrow \Sigma^0 n$ the kink becomes stronger with increasing density.

6. Summary and Outlook

The goal of this work was to describe hyperon-nucleon (YN) interaction in medium. In order to achieve this, first the principles of scattering theory were introduced and a scattering equation for singlet-even (SE) scattering has been derived. The next step was finding an adequate potential model, from which a YN potential could be constructed. Therefore, the Bonn potential [19] was used, a one-boson-exchange (OBE) model. The non-relativistic reduction of the Bonn potential for SE scattering was derived. Results from solving the scattering equation for this potential were compared to free-space NN data and theoretical predictions.

The YN potential then was obtained by fitting the NN potential to isospin basis YN data of the Jülich group [16] using overall factors. These factors turned out to be 0.86 for ΛN scattering, 0.79 for ΣN scattering and 0.02 for the transition between ΛN and ΣN states.

Afterwards the YN potential was used to solve the scattering equation in the particle basis, including coupling of two channels. Where the coupling of three channels is possible, this was approximated by calculation of two channel coupling in three subsystems. The agreement with the data was found to be improvable. The cross sections for small energies turned out to be too high, while they were too low for higher energies. This problem could be solved by fitting the potential to experimental data, while using different scaling factors for each component of the model, instead of the overall factors. Additionally higher partial waves should be included in further studies. However, the results for the scattering length were found to be in accordance with other theoretical predictions.

In order to include the in-medium interaction a two particle Pauli projection operator was derived. This allows for calculating scattering in medium with arbitrary density of each involved baryon. Then the results for scattering in symmetric nuclear matter were discussed. In further studies, the YN interaction in asymmetric matter and matter including hyperons could be studied. This possibility is already included in the code.

7. Bibliography

- [1] *NN-online.org*, September 2011.
- [2] Milton Abramowitz and Irene A. Stegun, *Handbook of Mathematical Functions with Formulas, Graphs, and Mathematical Tables*, tenth printing ed., New York, 1964.
- [3] G. Alexander, U. Karshon, A. Shapira, G. Yekutieli, R. Engelmann, H. Filthuth, and W. Lughofer, *Study of the Λ - N System in Low-Energy Λ - p Elastic Scattering*, Phys. Rev. **173** (1968), 1452–1460.
- [4] R. Blankenbecler and R. Sugar, *Linear Integral Equations for Relativistic Multichannel Scattering*, Phys. Rev. **142** (1966), 1051–1059.
- [5] John M. Blatt and L. C. Biedenharn, *Neutron-Proton Scattering with Spin-Orbit Coupling. I. General Expressions*, Phys. Rev. **86** (1952), 399–404.
- [6] I.N. Bronstein, K.A. Semendjajew, Musiol, and Mühlig, *Taschenbuch der Mathematik*, Deutsch, 2005.
- [7] G.R. Charlton, J. Badier, E. Barrelet, I. Makarovich, J. Pernegr, J.R. Hubbard, A. Leveque, C. Louedec, L. Moscoso, and D. Revel, *Hyperon-proton interactions between 0.5 and 4.0 GeV/c*, Physics Letters B **32** (1970), no. 8, 720 – 722.
- [8] D. Cline, R. March, and M. Sheaff, *Elastic Λ -proton scattering from 400 – 1300 MeV/c*, Physics Letters B **25** (1967), no. 6, 446 – 448.
- [9] Frank S. Crawford, Marcello Cresti, Myron L. Good, Frank T. Solmitz, M. Lynn Stevenson, and Harold K. Ticho, *Λ Interactions in Hydrogen*, Phys. Rev. Lett. **2** (1959), 174–177.
- [10] W. Demtröder, *Experimentalphysik 4: Kern-, Teilchen- Und Astrophysik*, Springer-lehrbuch, Springer, 2005.
- [11] H.G. Dosch, R. Engelmann, H. Filthuth, V. Hepp, and E. Kluge, *Elastic σp -scattering at low momenta*, Physics Letters **21** (1966), no. 2, 236 – 238.
- [12] F. Eisele, H. Filthuth, W. Föhlich, V. Hepp, and G. Zech, *Elastic $\Sigma^{+/-} p$ scattering at low energies*, Physics Letters B **37** (1971), 204–206.

-
- [13] R. Engelmann, H. Filthuth, V. Hepp, and E. Kluge, *Inelastic $\Sigma^- p$ -interactions at low momenta*, Physics Letters **21** (1966), no. 5, 587 – 589.
- [14] E. Epelbaum, H.-W. Hammer, and Ulf-G. Meißner, *Modern theory of nuclear forces*, Rev. Mod. Phys. **81** (2009), 1773–1825.
- [15] K. Erkelenz, R. Alzetta, and K. Holinde, *Momentum space calculations and helicity formalism in nuclear physics*, Nuclear Physics A **176** (1971), no. 2, 413 – 432.
- [16] Johann Haidenbauer, private communication, July 2011.
- [17] Christoph Marcus Keil, *Microscopic baryon-baryon interactions at finite density and hypernuclear structure*, Ph.D. thesis, Justus-Liebig-Universität Gießen, 2004.
- [18] R. Machleidt, *Computational Nuclear Physics 2—Nuclear Reactions*, ch. 1, pp. 1–29, Springer, New York, 1993.
- [19] R. Machleidt, K. Holinde, and Ch. Elster, *The Bonn meson-exchange model for the nucleon–nucleon interaction*, Physics Reports **149** (1987), no. 1, 1 – 89.
- [20] P. M. M. Maessen, Th. A. Rijken, and J. J. de Swart, *Soft-core baryon-baryon one-boson-exchange models. II. Hyperon-nucleon potential*, Phys. Rev. C **40** (1989), 2226–2245.
- [21] P. J. Mulders, *Comment on S-Matrix parameterizations in NN-scattering*, Tech. report, August 1981.
- [22] Anika Obermann, *Lösung der Bethe-Salpeter-Gleichung für ein Yukawa-Potential*, Vertiefungsmodulbericht, July 2010.
- [23] M.A. Preston and R.K. Bhaduri, *Structure of the Nucleus*, Westview Press, 1993.
- [24] Th. A. Rijken, V. G. J. Stoks, and Y. Yamamoto, *Soft-core hyperon-nucleon potentials*, Phys. Rev. C **59** (1999), no. 1, 21–40.
- [25] Franz Schwabl, *Quantenmechanik (QM I) : eine Einführung*, 2007, Online-Ausg.:, pp. XV, 430 S.
- [26] H. P. Stapp, T. J. Ypsilantis, and N. Metropolis, *Phase-Shift Analysis of 310-Mev Proton-Proton Scattering Experiments*, Phys. Rev. **105** (1957), 302–310.
- [27] V. G. J. Stoks, R. A. M. Klomp, C. P. F. Terheggen, and J. J. de Swart, *Construction of high-quality NN potential models*, Phys. Rev. C **49** (1994), 2950–2962.
- [28] V. G. J. Stoks and Th. A. Rijken, *Soft-core baryon-baryon potentials for the complete baryon octet*, Phys. Rev. C **59** (1999), no. 6, 3009–3020.
- [29] Hideki Yukawa, *On the Interaction of Elementary Particles. I **, Progress of Theoretical Physics Supplement **1** (1955), 1–10.

A. Solving the R -Matrix Equation

In this chapter the approach for solving the R -matrix equation is displayed. We follow the explanations in [18] closely.

Integral equations of the shape

$$\phi(x) = f(x) + \lambda \int_a^b K(x, y)\phi(y)dy \quad (\text{A.1})$$

are called Fredholm integral equations of the second kind. They can be displayed as a system of linear equations and solved numerically under the prerequisite that $K(x, y)$ and $f(x)$ are steady for $a \leq x \leq b$, $a \leq y \leq b$ and solved by Fredholm's Method [6].

Comparing eq. A.1 to the R -matrix equation (eq. 2.58), we find

$$\phi(x) = {}^0R^J(q', q) \quad (\text{A.2})$$

$$f(x) = {}^0V^J(q', q) \quad (\text{A.3})$$

$$K(x, y) = {}^0V^J(q', k)G(k, q) \quad (\text{A.4})$$

$$\lambda = \frac{1}{2\pi^2}. \quad (\text{A.5})$$

Though, y corresponds to the intermediate momentum k , over which the integration has to be performed and x corresponds to q' .

Because the integrand should be steady, we have to eliminate the principle value. This can be achieved by adding a zero term:

$${}^0R^J(q', q) = {}^0V^J(q', q) + \int \frac{dk}{2\pi^2} \frac{\mu}{q^2 - k^2} \left[k^2 {}^0V^J(q', k) {}^0R^J(k, q) - q^2 {}^0V^J(q', q) {}^0R^J(q, q) \right]. \quad (\text{A.6})$$

In the next step the integral is approximated by a quadrature formula according to

$$\int_0^\infty f(k) = \sum_{i=1}^N f(k_i) s_i. \quad (\text{A.7})$$

with the integration points k_i and weights s_i . These are calculated from the familiar Gaussian integration points x_i and weights w_i using the relations

$$k_i = C \tan\left(\frac{\pi}{4}(x_i + 1)\right) \quad (\text{A.8})$$

$$s_i = C \frac{\pi}{4} \frac{w_i}{\cos^2\left(\frac{\pi}{4}(x_i + 1)\right)} \quad (\text{A.9})$$

with $C = 400$ MeV.

We rearrange the integral equation as follows:

$${}^0R^J(q', q) - \int \frac{dk}{2\pi^2} \frac{\mu}{q^2 - k^2} \left[k^2 {}^0V^J(q', k) {}^0R^J(k, q) - q^2 {}^0V^J(q', q) {}^0R^J(q, q) \right] = {}^0V^J(q', q) \quad (\text{A.10})$$

Now the R -matrix equation can be solved in terms of $N + 1$ linear equations. These can be solved using standard methods [18].

We write the system of equations in matrix notation

$${}^0A^J {}^0R^J = {}^0V^J \quad (\text{A.11})$$

with the $N + 1$ dimensional vectors ${}^0R^J$ and ${}^0V^J$ and the $(N + 1)(N + 1)$ matrix ${}^0A^J$, which is constructed by

$${}^0A_{ij}^J = \delta_{ij} + u_j {}^0V^J(k_i, k_j). \quad (\text{A.12})$$

Its elements are calculated as

$$u_j = \mu k_j^2 \frac{s_j}{k_j^2 - q^2}, \quad \text{for } 1 \leq j \leq N \quad (\text{A.13})$$

$$u_{N+1} = -\mu q^2 \sum_{i=1}^N \frac{s_j}{k_j^2 - q^2}. \quad (\text{A.14})$$

For calculating the phase shifts, we need the on-shell R -matrix ${}^0R_{N+1, N+1}^J$ only.

B. Approximation of the Legendre Functions

We have to approximate $Q_0(x)$ and $Q_1(x)$ in the regions where x becomes very small or very large, because we have to calculate differences and sums of these functions (during the calculation of the potentials) which can cause huge numerical errors. First, we reformulate

$$Q_0(x) = \frac{1}{2} \ln(1+2u) = \frac{1}{2} \ln\left(1 + \frac{2}{v}\right) \quad (\text{B.1})$$

$$Q_1(x) = \frac{1 + \frac{1}{u}}{2} \ln(1+2u) - 1 = \frac{1+v}{2} \ln\left(1 + \frac{2}{v}\right) - 1 \quad (\text{B.2})$$

with $u = \frac{1}{x-1}$ and $v = \frac{1}{u}$ and expand these expressions for $v \leq 10^{-2}$ ($u \leq 10^{-2}$). This corresponds to small (large) x . We find for the power series around $u, v = 0$ [6]:

$$Q_0(x) = u - u^2 + \frac{4u^3}{3} - 2u^4 + \dots \quad (\text{B.3})$$

$$Q_0(x) = \frac{1}{2} \log \frac{2}{v} + \frac{v}{4} - \frac{v^2}{16} + \frac{v^3}{48} - \dots \quad (\text{B.4})$$

$$Q_1(x) = \frac{u^2}{3} - \frac{2u^3}{3} + \frac{6u^4}{5} - \frac{32u^5}{15} + \dots \quad (\text{B.5})$$

$$Q_1(x) = \frac{1}{2} \left(-2 + \log \frac{2}{v}\right) + \frac{1}{4} \left(1 + 2 \log \frac{2}{v}\right) v + \frac{3v^2}{16} - \frac{v^3}{24} + \frac{5v^4}{384} - \dots \quad (\text{B.6})$$

The expansion of $Q'_0(x)$ for large x is done by substituting $x = \frac{1}{z}$ and expanding around $z = 0$:

$$Q'_0(x) = \frac{z^2}{z^2 - 1} = -z^2 - z^4 - z^6 - z^8 - \dots \quad (\text{B.7})$$

C. Properties of the Legendre Polynomials

In this section the properties of the Legendre polynomials used in our calculations are given in short. A detailed discussion can be found in [6].

The Legendre polynomials are defined by the recursion formula

$$P_{n+1}(x) = \frac{(2n+1)xP_n(x) - nP_{n-1}(x)}{n+1}, \quad n \geq 1 \quad (\text{C.1})$$

with the first two polynomials

$$P_0(x) = 1 \quad (\text{C.2})$$

$$P_1(x) = x. \quad (\text{C.3})$$

The Legendre polynomials are orthogonal, i.e.

$$\int_{-1}^1 P_l(\cos \vartheta) P_{l'}(\cos \vartheta) d \cos \vartheta = \frac{2}{2l+1} \delta_{ll'}. \quad (\text{C.4})$$

D. Partial-Wave Decomposition

A partial-wave decomposition of a potential can be performed as

$$V(\vec{k}) = \sum_{l=0}^{\infty} (2l+1) P_l(\cos \vartheta) V_l \quad (\text{D.1})$$

with the l th Legendre polynomial $P_l(\cos \theta)$ and where V_l is the desired potential in the l th partial wave. In order to obtain a formula for V_l , we multiply eq. D.1 with $P_{l'}(\cos \theta)$ and integrate over $\cos \theta$ from -1 to 1 :

$$\int_{-1}^1 V(\vec{k}) P_{l'}(\cos \vartheta) d \cos \vartheta = \sum_l^{\infty} (2l+1) V_l \int_{-1}^1 P_l(\cos \vartheta) P_{l'}(\cos \vartheta) d \cos \vartheta \quad (\text{D.2})$$

Using the orthogonality of the Legendre polynomials (eq. C.4) we find:

$$V_{l'} = \frac{1}{2} \int_{-1}^1 V(\vec{k}) P_{l'}(\cos \vartheta) d \cos \vartheta \quad (\text{D.3})$$

A detailed discussion of this procedure can be found e.g. in [25].

E. Danksagung

Ich möchte mich bei allen bedanken, die mich während dieser Arbeit unterstützt haben. Besonderer Dank geht an...

Prof. Dr. Horst Lenske für die interessante Themenstellung und engagierte Betreuung. Ich konnte mich mit allen fachlichen Fragen (die stets sehr ausführlich beantwortet wurden) jederzeit an ihn wenden.

Univ. Doz. Dr. Johann Haidenbauer und Prof. Dr. Evgeny Epelbaum für die Zurverfügungstellung von Ergebnissen des Jülich Modells.

Die Computer-Admins des Instituts, insbesondere Dipl.-Phys. Janus Weil für Hilfe bei allen Problemen mit Computern, Druckern und Kopierern und deren schnelle und zuverlässige Beseitigung.

Die Sekretärinnen des Instituts, Elke Jung, Ilka Sproates und Monika Weingärtner für Hilfe mit diversen Formularen und Verwaltungs-Formalitäten.

Dipl.-Phys. Stefanie Lourenco für anregende Gespräche, Cola, Muffins & Co.

Dipl.-Phys. Jonas Hellhund für Geduld, Aufmunterung, Korrekturlesen und so viel anderes, das ich von ihm bekommen habe.

Meine Familie, besonders meine Eltern für ihre moralische und finanzielle Unterstützung während meines gesamten Studiums.

Versicherung an Eides statt (Affirmation)

Hiermit versichere ich, die vorliegende Arbeit selbst und allein verfasst zu haben sowie außer den Genannten keine weiteren Quellen oder Hilfsmittel verwendet zu haben. Alle Ausführungen, die anderen Schriften wörtlich oder sinngemäß entnommen wurden, sind als solche kenntlich gemacht. Des Weiteren versichere ich, dass die Arbeit in gleicher oder ähnlicher Fassung noch nicht Bestandteil einer Studien- oder Prüfungsleistung war.

Buseck, den 24. September 2011

(ANIKA OBERMANN)
